12-2013

Microfluidics Guided by Redox-Magnetohydrodynamics (MHD) for Lab-on-a-Chip Applications

Vishal Sahore
University of Arkansas, Fayetteville

Microfluidics Guided by Redox-Magnetohydrodynamics (MHD) for Lab-on-a-Chip Applications

Microfluidics Guided by Redox-Magnetohydrodynamics (MHD) for Lab-on-a-Chip Applications

A dissertation submitted in partial fulfillment
of the requirements for the degree of
Doctor of Philosophy in Microelectronics-Photonics

by

Vishal Sahore
University of Wisconsin
Master of Science in Physics, 2009

December 2013
University of Arkansas

This dissertation is approved for recommendation to the Graduate Council.

_____

Dr. Ingrid Fritsch
Dissertation Director

_____

Dr. Chao-Hung Steve Tung
Committee Member

_____

Dr. Christa Hestekin
Committee Member

_____

Dr. David Paul
Committee Member

_____

Prof. Kenneth G. Vickers
Ex-Officio Member

The following signatories attest that all software used in this dissertation was legally licensed for use by Vishal Sahore for research purposes and publication.

Mr. Vishal Sahore, Student	Dr. Ingrid Fritsch, Dissertation Director

This dissertation was submitted to http://www.turnitin.com for plagiarism review by the TurnItIn company software. The signatories have examined the report on this dissertation that was returned by TurnItIn and attest that, in their opinion. The items highlighted by the software are incidental to common usage and are not plagiarized material.

Prof. Kenneth G. Vickers, MicroEP Director	Dr. Ingrid Fritsch, Dissertation Director

Abstract

Unique microfluidic control actuated by simply turning off and on microfabricated electrodes in a small-volume system was investigated for lab-on-a-chip applications. This was accomplished using a relatively new pumping technique of redox-magnetohydrodynamics (MHD), which as shown in this dissertation generated the important microfluidic features of flat flow profile and fluid circulation. MHD is driven by the body force, $\mathbf{F_B} = \mathbf{j} \times \mathbf{B}$, which is the magnetic part of the Lorentz force equation, and its direction is given by the right hand rule. The ionic current density, **j**, was generated in an equimolar solution of potassium ferri/ferro cyanide by applying a constant current/potential across the gap between an anode-cathode pair of the electrodes. The magnetic field, **B**, was produced with an NdFeB permanent magnet beneath the chip.

Two types of microelectrode geometries were used in this dissertation: microbands and concentric disks and rings. Horizontal flow profiles having uniform velocities (≤124.0 μm/s) at fixed heights across different gaps were sustained along a ~25.0 mm path using microband electrodes, in a small volume contained over an insulated silicon chip. Microfluidic rotational flow with velocity ≤ 14 μm/s was also achieved over an annular region between concentric disk (radius: 80 μm) and ring (inner radius: 800 μm) microelectrodes. In a different but related series of studies, natural convection generated by electrochemical processes was studied in a steady state microfluidic system, but without using redox-MHD convection. Natural convection was found to generate a maximum fluid velocity of < 10 μm/s radially across the gap between concentric disk-ring microelectrodes.

A proof-of-concept magnetic microbead enzyme assay was also integrated with the redox-MHD flat flow profile generated by $[Ru(NH_3)_6]^{3+/2+}$ in Tris buffer. Selective placement of

the assay complex at different locations combined with the uniform transport of the electroactive species by-product generated a strong current signal at the locations that were on the same flow path as the detector. When the assay complex was placed at other locations that were on parallel flow paths the current signal at the detector was insignificant (20%), thus confirming the potential of redox-MHD microfluidics to perform multiple, parallel assay detections.

Acknowledgements

I would like to express my greatest regards and special thanks to Dr. Ingrid Fritsch for shaping my career through her visionary leadership. Dr. Fritch has carefully crafted my scientific skills by investing her time, energy, and resources. I am indebted to Dr. Fritsch for investing her intellectual talent to succeed me in spite of her hectic professional and personal life. I would like to thank Prof. Ken Vickers for his thought provoking conversations, unlimited and unconditional support, and encouragement to plan ahead to beat the deadlines so that I can succeed professionally. I am also thankful to Dr. David Paul, Dr. Steve Tung, and Dr. Christa Hestekin for their valuable insights and suggestions that they have given me during our research conversations. I would like to thank Dr. Anupama Aggarwal, Dr. Melissa Weston, and Mr. Mathew Gerner for their unconditional support and mentorship that has helped me to climb the experimental learning curve. I would also like to thank the whole Fritsch group for their sincere participation, conversation, and support regarding my research efforts. I would like to thank Jerry Homesley and K.Z. Shein for their help in fixing the Evaporator and helping with the NMR analysis. I would like to express my regards to Mr. Errol Porter for his help during electrode chip fabrication.

Foremost, I would like to express my regards to my parents, brother, sister-in-law, and friends who have encouraged me in each and every aspect of my life, thank you very much for providing the encouragement and unconditional support I needed to complete this journey. I would like to thank my cousin Mr. Rajiv Kumar Sharma who has enthusiastically supported my idea of higher studies in United States. I would like to express my affection toward my nephew Mr. Pratham Sahore for being the next generation lightning rod in our family.

This program is financially supported by the National Science Foundation under Grant No. CHE-0719097 and CBET-1336853; and Arkansas Biosciences Institute, the major research component of the Arkansas Tobacco Settlement Proceeds Act of 2000. Any opinions, findings, and conclusions or recommendations expressed in this material are those of the author and do not necessarily reflect the views of the National Science Foundation and the Arkansas Biosciences Institute. Research possible through the use of the High Density Electronics Center at the University of Arkansas, Fayetteville campus.

Table of Contents

x-intercept = -1557 ± 44 μm for the three-electrode configuration; and y = (0.0674 ± 0.0026) x + (113.8 ± 3.1), R^2= 0.9926, x-intercept = -1689 ± 80 μm for the four-electrode configuration. Equations for the lines over the anodes in (b) are y = (-0.0949 ± 0.0083) x + (129.6 ± 8.3), R^2= 0.9925, x-intercept = 1366 ± 148 μm, for the two-electrode configuration; y = (-0.0857 ± 0.0017) x + (129.1 ± 1.9), R^2= 0.9988, x-intercept = 1506 ± 38 μm for the three-electrode configuration; and y = (-0.0716 ± 0.0011) x + (116.5 ± 1.3), R^2= 0.9988, x-intercept = 1627 ± 31 μm for the four-electrode configuration. The units of the slopes are in μm/s / μm or s^{-1}; the units of the y-intercepts are μm/s. 64

Figure 2.S10 Dependence of velocity over (a) the cathodes and (b) the anodes for the 5.6 mm gap and for which the current is constant at 120 μA and the number of active electrodes is increased from one to four. The plots of raw data are expanded views of the electrode regions from Figure 3b in the main document. The lines correspond to the least squares best fit to the raw data for each electrode configuration. Equations for the lines over the cathodes in (a) are: y = (0.1108 ± 0.0121) x + (325.9 ± 32), R^2 =0.9883, x-intercept = -2942 ± 432 μm, for the one-electrode configuration; y = (0.0917 ± 0.0080) x + (284.5 ± 21.9), R^2 = 0.9706, x-intercept = -3101 ± 361 μm, for the two-electrode configuration; y = (0.0758 ± 0.0050) x + (245.3 ± 14.1), R^2=0.9788, x-intercept = -3238 ± 283 μm, for the three-electrode configuration; and y = (0.0700 ± 0.0044) x + (230.8 ± 12.8), R^2=0.9764, x-intercept = -3298 ± 278 μm, for the four-electrode configuration. Equations for the lines over the anodes in (b) are: y = (-0.1228 ± 0.0125) x + (350.6 ± 33.4), R^2=0.9897, x-intercept = 2855 ± 399 μm, for the one-electrode configuration; y = (-0.0871 ± 0.0043) x + (264.8 ± 12), R^2= 0.9903, x-intercept = 3039 ± 203 μm, for the two-electrode configuration; y = (-0.0746 ± 0.0034) x + (234.6 ± 9.6), R^2=0.9898, x-intercept = 3144 ± 192 μm, for the three-electrode configuration; and y = (-0.0868 ± 0.0090) x + (267.8 ± 25),

1. Introduction to Redox-Magnetohydrodynamics (MHD) Microfluidics

1.1 Introduction

Unique microfluidic control actuated by simply turning off and on microfabricated electrodes in a small-volume system was investigated for the lab-on-a-chip applications. This has been accomplished using a relatively new and promising fluid pumping technique of redox-magnetohydrodynamics (MHD), which herein this dissertation has generated the important microfluidic features of flat flow profile and fluid circulation. To enhance the scope of this method, the redox-MHD flat flow profile feature was further used to demonstrate its capability to perform multiple, parallel assays with electrochemical detection with a single chip platform. In a different but related study, the significance of electrochemically generated density gradients that induce natural convection for on-chip microfluidic systems that are kept under steady state conditions was also established.

Lab-on-a-chip technology integrates multiple laboratory functions at a single hand-held device platform. This technology can miniaturize apparatuses for chemical analysis, and is capable of performing a variety of applications including disease diagnostics, drug discovery, proteomics, genomics, and environmental monitoring.[1,2,3,4,5] Important advantages of downsizing chemical analysis in a lab-on-a-chip device include portability due to small size which could also help to extend its application toward point of care diagnostics; possibility to integrate multiple, parallel analysis on a single chip to reduce analysis time and increase device efficiency; require low sample volume, generate less waste, and need low power to operate, and therefore could also reduce the overall operational cost.[1,3,5-7,8, 9, 4] Microfluidics plays an important role toward this miniaturization by controlling and automating small fluid volumes over the chip..[1,8,9,4,10] Several fluid pumps have been used so far, with pressure driven, electrokinetic, and centrifugal methods being the most common approaches.[11,12,13,] Pressure driven and centrifugal pumps are useful but

require mechanical parts and need fluid flow channels to operate them, thus complicating the device design and fabrication procedure.[14,15]

Electrochemical microfluidic pumps are also well suited for the fluid actuation, and works due to the mass transfer of electroactive species. Three common modes of mass transfer are diffusion, migration and convection. Although diffusion is always present and migration takes place when there is an electric field, however it is the convection that generates a substantial fluid movement in the microfluidic device. Mass transfer in the electrochemical systems is given by the Nernst – Planck equation, and its one dimensional form is:

$$J_i(x) = -D_i \frac{\partial C_i(x)}{\partial x} - \frac{Z_i F}{RT} D_i C_i \frac{\partial \phi(x)}{\partial x} + C_i v(x) \qquad \text{(Eq. 1.1)}$$

Here $J_i(x)$ is the flux of the ionic species (mol/ s.cm^2); D_i is the diffusion coefficient (cm^2/s); C_i is the ionic concentration (mol/cm^3); $\frac{\partial C_i(x)}{\partial x}$ is the ionic species concentration gradient in the x direction; Z_i is the electric charge; F, R, T are the faraday constant (C/mol) , ideal gas constant (J/mol.K) and the temperature (K) respectively; $\frac{\partial \varphi(x)}{\partial x}$ is the electric potential gradient in the x direction (volt/cm); $v(x)$ is the velocity (cm/s)

Convection can be either forced or natural. Electrokinetic pumping is a popular method that is governed by the forced convection,[11,16,17,18] however its fluid flow depends upon the solution composition and channel wall material, and needs high operational voltages that further create problems associated with heat generation, electrode degradation, and bubble generation.[19] Magnetohydrodynamics (MHD) fluid pumping is another option where convection can be generated by combining the electric and magnetic fields, and which can reduce the flow

dependence on solution composition and at the same time can generate a bidirectional fluid flow compatible with aqueous and non- aqueous solutions.[20,21,22,23,24,25,26] MHD has been used in the past for a variety of analytical applications,[25,27,28,29] however in the absence of easily reduced and oxidized species traditional MHD methods using a supporting electrolyte also require high voltages, which further results in the bubble generation.[30,21,31] An alternative is to introduce redox species into the solution that can sustain the faradaic current at a lower overpotential than for the solvent and the electrode material. This approach is coined as "redox-MHD". Redox-MHD pumping not only avoids bubble generation and electrode degradation, but also generates programmable and bidirectional fluid flow that is compatible with aqueous as well as non-aqueous solutions, and provides channel-less pumping that can allow more flexibility in device design and fabrication.[32,33,34] Redox-MHD has been extensively studied in our laboratory for the past few years,[35,36,37,38,33,29,34,39,40,41] and is the subject of some of the studies in this dissertation. Under steady state conditions the electrochemical reactions at electrode-solution interface and their associated counter ion movement in the electrode vicinity, can also lead to a density mismatch with respect to the bulk solution, thus generating the fluid's natural convection due to the onset of buoyant forces.[42] The natural convection has also been studied in this dissertation.

MHD is driven by the body force, $\mathbf{F_B}$ (N/m^3), which is the magnetic part of the Lorentz force equation, and its magnitude and direction at a given location in solution depend on the ionic current density, $\mathbf{j}$ (A/m^2) and the magnetic flux density $\mathbf{B}$ (Tesla) from an externally applied magnetic field through a relationship described by the right hand rule, $\mathbf{F_B = j \times B}$.[30,36,21,22,23,24] For a given fluid cell having a fixed geometry and for a magnetic field with uniform magnitude and direction, redox-MHD convection is primarily controlled by the ionic current density ($\mathbf{j}$), which is defined by the size and shape of the electrodes where the electrochemical processes take

place, and any nonuniformities in the ionic conductivity of the solution. In addition to the MHD force, two other types of magnetic forces namely the magnetic gradient force (Eq. 1.2)[43] and the paramagnetic concentration gradient force (Eq. 1.3)[43] were also possible, however all the results involving magnetic fields were explained by the MHD force in this dissertation.

$$F_{\nabla B} = 2N_A C_D[(m^*)^2/kT](B.\nabla)B \qquad \text{(Eq. 1.2)}$$

$$F_{\nabla C} = N_A[(m^*)^2/kT]B^2\nabla C \qquad \text{(Eq. 1.3)}$$

Here N_A is the Avogadro number; C_D is the concentration of the species with spin ½; m* is equal to g(1/2) μ_B where g is the Lande's g factor and μ_B is the Bohr magneton; k and T are the Boltzmann constant and temperature, respectively; and B is the magnetic field.

Four different types of electrochemical techniques cyclic voltammetry (CV), chronoamperometry (CA), chronopotentiometry (CP), and square wave voltammetry (SWV) were used in this dissertation. In Cyclic and square wave voltammetry current is monitored as a function of the potential sweep. Chronoamperometry works by recording the variation in current as a function of time, by applying a constant step potential. Chronopotentiometry monitors the change in potential with current due an applied step current at the working electrode. Fluid movement was recorded

Two types of electrode geometries were used in this dissertation, microband and concentric disk-ring, with examples of their resulting MHD fluid flow directions given in Figure 1.1. Electrode chips of a single design and containing both types of these geometries was used throughout this dissertation (see Figure 1.2), different electrodes were activated to perform the different experiments reported in the chapters of this dissertation and are further defined there. Briefly, a 2.0 in. (length) × 1.0 in. (width) chip has three parallel sets of microband electrodes

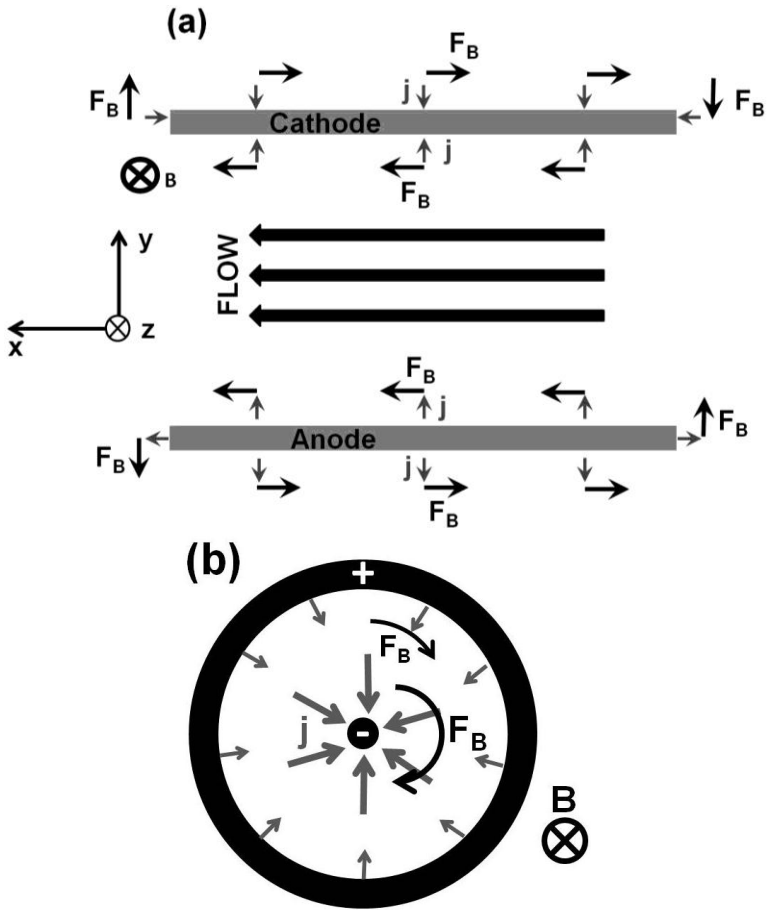

Figure 1.1 Redox-magnetohydrodynamics (MHD)-guided fluid movement. (a) Two long and narrow rectangular electrodes (band electrodes) of same size and material are placed parallel to each other. Electrochemical reaction generates an ionic current density with its direction inward for cathode but outward for anode. In the central region between oppositely biased electrodes, however, ionic current density is in the same direction (toward the cathode) and is uniform within the horizontal plane (except there should be a little curvature upward or downward, especially nearer the electrodes). In presence of a magnetic field that is perpendicular to the plane of the electrodes and directed toward that plane, and using right hand rule, fluid will move in a direction as shown in the figure. (b) In the region between concentric disk-ring microelectrodes, the direction of the ionic current is directed radially inward, therefore with a perpendicular magnetic field, fluid will flow in a circular direction.

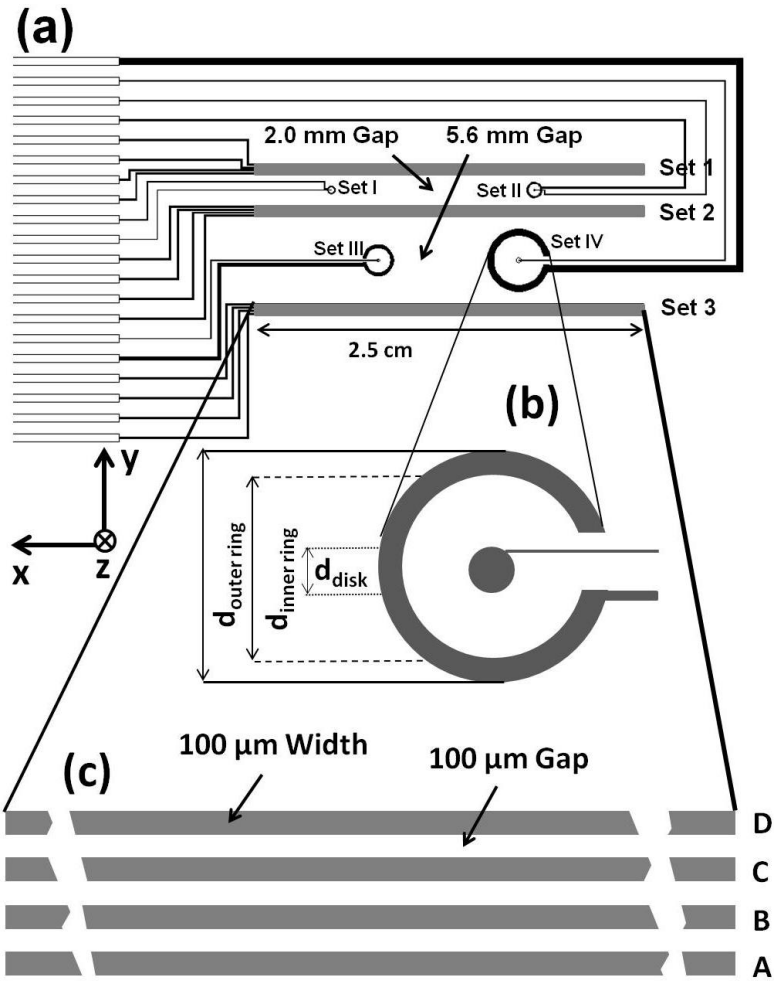

Figure 1.2 (a) Top down view schematic of the electrode chip design. An individual chip has three microband electrode sets ("set 1", "set 2", and "set 3") with each having four individually-addressable rectangular microelectrodes (A, B, C, D) of equal size (25.0 mm long × 98 ± 0.1 µm wide × ~100 nm thick), and four different sets ("set I", "set II", "set III", and "set IV") of concentric disk-ring microelectrodes. Intraset electrode gap within each microband electrode set is 100 µm, whereas the interset gaps are 2.0 (between sets 1 and 2) and 5.6 mm (between sets 2 and 3). Expanded views of the two kinds of electrode geometries are shown in **(b)** for the concentric disk-ring electrode set IV, and in **(c)** for the microband electrode set 3, with the corresponding electrode dimensions.

Table 1.1 Dimensions of the individual electrodes in the two kinds of geometries available on the electrode chip.

Single Microband Electrode		**Concentric Disk-Ring**				
Length (mm)	25		**Set I**	**Set II**	**Set III**	**Set IV**
		Disk Radius (μm)	20	40	80	160
Width (mm)	0.1	**Inner Ring Radius (μm)**	200	400	800	1600
		Outer Ring Radius (μm)	250	500	1000	2000

with each set containing four equally-sized individually-addressable electrodes placed equidistant from each other (See Figure 1.2c), and four differently-sized sets of concentric disk-ring gold microelectrodes (See a representative expanded view of set IV in Figure 1.2b). The overall electrode dimensions are given in Table 1.1.

Two different types of redox species were used in this dissertation to sustain the electrochemical reactions at the electrode/solution interface. In fundamental microfluidic studies, the solution contained potassium ferricyanide and potassium ferrocyanide in a supporting electrolyte of potassium chloride. For assay detection studies, a solution of ruthenium(II) hexamine chloride and ruthenium(III) hexamine chloride in tris buffer was used due to its compatibility with the assay detection method and with the enzyme. Flow velocity measurements were performed by tracking the path of polystyrene latex beads mixed with redox species solution, and the two dimensional data analysis was performed by visualizing the particle path in the flow direction by particle image velocimetry (PIV) software.[44,45] More details on the relevant background, experimental descriptions, and results and discussion are provided within each chapter that focuses on a different set of studies.

Chapter 2 of this dissertation establishes redox-MHD guided flat flow profiles in a small fluid volume over large distances that are compatible with lab-on-a-chip applications. This is accomplished over a chip under laminar flow conditions (Reynolds number < 1) when a constant current is applied at the on-chip microband electrodes in the presence of an externally applied magnetic field. Vertical and horizontal flow profiles were measured by changing the interset electrode gaps, number of active electrodes, applied currents, and velocity measurement heights. This chapter is based upon an article submitted to the journal *Analytical Chemistry*.

Chapter 3 of this dissertation investigates redox-MHD microfluidic rotational flow in a small volume contained over the chip, under laminar flow conditions. Fluid circulation was studied at a region between concentric disk and ring microelectrodes when a potential difference was applied between them in the presence of a magnetic field. Fluid flow was visualized by tracking the path of polystyrene latex beads and a red dye added externally to the redox species solution. This chapter is based upon a manuscript to be submitted to the journal *Microfluidics and Nanofluidics*.

In Chapter 4 of this dissertation a proof-of-concept magnetic microbead assay was integrated with redox-magnetohydrodynamics (MHD) microfluidics to take advantage of the magnet beneath the chip and the uniform flat flow profiles, as a first step toward developing multiple, parallel chemical analysis on a chip. In this work, a flat flow profile was generated using $[Ru(NH_3)_6]^{3+/2+}$ in Tris buffer, and the bead assay complex was formed by reacting streptavidin coated superparamagnetic beads with biotinylated alkaline phosphatase (AP). Selective placement of bead assay complex at different locations, and the uniform transport of electroactive *p*-aminophenol (PAP_R) created by reaction between AP and its electroinactive substrate *p*-aminophenyl phosphate (PAPP), has generated a strong current signal at the locations that were on horizontal path of the detector. At other locations that were off the detector path, current signal is insignificant, thus confirming the potential of redox-MHD flat flow profile to perform multiple, parallel assay detection.

Chapter 5 of this dissertation demonstrates the activation and behavior of density gradient induced-natural convection at electrodes within small volumes suitable for microfluidic devices. Electrochemical reactions at electrode-solution interfaces and their associated counter ion movement in the vicinity of electrodes generates a density mismatch with respect to the bulk

solution, and hence induces a fluid's natural convection due to the onset of buoyant forces. Here, natural convection was measured at an annular region between concentric disk-ring microelectrodes. Observed parameters were the sudden changes in electrode current, potential, and localized fluid velocity, and were found to be significant enough to affect the analytical systems that are used in microfluidics and electrodeposition technology. Overall, natural convection, as measured by tracking microbeads in a horizontal plane and vertically, was investigated as a function of electrode size, electrode polarity, solution concentration, and magnitude of the applied current.

Chapter 6 of this dissertation discusses the conclusions of redox-MHD and natural convection studies, and possible future applications to expand the horizon of this unique pumping method.

This dissertation is written in a format that is compatible to be published in peer reviewed journals. An individual chapter has the main text as well as the supporting information at the end of each chapter. Supporting information chapter, sections, and figures are labeled as Chapter Number.S. A detailed procedure for the electrode chip fabrication is described in the Appendix A.

1.2 References

(1) Chin, C. D.; Linder, V.; Sia, S. K. *Lab on a Chip* **2007**, *7*. 41-57.

(2) Dittrich, P. S.; Manz, A. *Nature Reviews Drug Discovery* **2006**, *5*. 210-218.

(3) Foudeh, A. M.; Didar, T. F.; Veres, T.; Tabrizian, M. *Lab on a Chip* **2012**, *12*. 3249-3266.

(4) Gardeniers, J. G. E.; van den Berg, A. *Analytical and Bioanalytical Chemistry* **2004**, *378*. 1700-1703.

(5) Stone, H. A.; Stroock, A. D.; Ajdari, A. *Annual Review of Fluid Mechanics* **2004**, *36*. 381-411.

(6) Ohno, K.; Tachikawa, K.; Manz, A. *Electrophoresis* **2008**, *29*. 4443-4453; Erickson, D.; Li, D. Q. *Analytica Chimica Acta* **2004**, *507*. 11-26.

(7) Roman, G. T.; Kennedy, R. T. *Journal of Chromatography A* **2007**, *1168*. 170-188.

(8) Khandurina, J.; Guttman, A. *Journal of Chromatography A* **2002**, *943*. 159-183.

(9) Squires, T. M.; Quake, S. R. *Reviews of Modern Physics* **2005**, *77*. 977-1026.

(10) Iverson, B. D.; Garimella, S. V. *Microfluidics and Nanofluidics* **2008**, *5*. 145-174.

(11) Jacobson, S. C.; Hergenroder, R.; Koutny, L. B.; Ramsey, J. M. *Analytical Chemistry* **1994**, *66*. 2369-2373.

(12) Rathore, A. S. *Electrophoresis* **2002**, *23*. 3827-3846.

(13) Nguyen, N. T.; Huang, X. Y.; Chuan, T. K. *Journal of Fluids Engineering-Transactions of the Asme* **2002**, *124*. 384-392.

(14) Duffy, D. C.; Gillis, H. L.; Lin, J.; Sheppard, N. F.; Kellogg, G. J. *Analytical Chemistry* **1999**, *71*. 4669-4678.

(15) Dutta, D.; Leighton, D. T. *Analytical Chemistry* **2003**, *75*. 57-70.

(16) Chen, L. X.; Choot, J.; Yan, B. *Expert Opinion on Drug Delivery* **2007**, *4*. 119-129.

(17) Paul, P. H.; Arnold, D. W.; Neyer, D. W.; Smith, K. B. *Micro Total Analysis Systems 2000, Proceedings* **2000**. 583-590.

(18) Bazant, M. Z.; Ben, Y. X. *Lab on a Chip* **2006**, *6*. 1455-1461.

(19) Pamme, N. *Lab on a Chip* **2006**, *6*. 24-38.

(20) Weston, M. C.; Gerner, M. D.; Fritsch, I. *Anal Chem* **2010**, *82*. 3411-8.

(21) Leventis, N.; Gao, X. R. *Analytical Chemistry* **2001**, *73*. 3981-3992.

(22) Qian, S.; Bau, H. H. *Mechanics Research Communications* **2009**, *36*. 10-21.

(23) Grant, K. M.; Hemmert, J. W.; White, H. S. *Journal of the American Chemical Society* **2002**, *124*. 462-467.

(24) West, J.; Karamata, B.; Lillis, B.; Gleeson, J. P.; Alderman, J.; Collins, J. K.; Lane, W.; Mathewson, A.; Berney, H. *Lab on a Chip* **2002**, *2*. 224-230.

(25) Kabbani, H.; Wang, A. H.; Luo, X. B.; Qian, S. Z. *Physics of Fluids* **2007**, *19*.

(26) Eijkel, J. C. T.; Dalton, C.; Hayden, C. J.; Burt, J. P.; Manz, A. *Sensors and Actuators B-Chemical* **2003**, *92*. 215-221.

(27) Homsy, A.; Linder, V.; Lucklum, F.; de Rooij, N. F. *Sensors and Actuators B-Chemical* **2007**, *123*. 636-646.

(28) Weston, M. C.; Anderson, E. C.; Arumugam, P. U.; Narasimhan, P. Y.; Fritsch, I. *Analyst* **2006**, *131*. 1322-1331.

(29) Pamme, N. *Lab Chip* **2006**, *6*. 24-38.

(30) Kang, H. J.; Choi, B. *Sensors and Actuators a-Physical* **2011**, *165*. 439-445.

(31) Anderson, E. C.; Weston, M. C.; Fritsch, I. *Anal Chem* **2010**, *82*. 2643-51.

(32) Weston, M. C.; Nash, C. K.; Homesley, J. J.; Fritsch, I. *Analytical Chemistry* **2012**, *84*. 9402-9409.

(33) Arumugam, P. U.; Fakunle, E. S.; Anderson, E. C.; Evans, S. R.; King, K. G.; Aguilar, Z. P.; Carter, C. S.; Fritsch, I. *Journal of the Electrochemical Society* **2006**, *153*. E185-E194.

(34) Weston, M. C.; Gerner, M. D.; Fritsch, I. *Analytical Chemistry* **2010**, *82*. 3411-3418.

(35) Anderson, E. C.; Weston, M. C.; Fritsch, I. *Analytical Chemistry* **2010**, *82*. 2643-2651.

(36) Weston, M. C.; Nash, C. K.; Fritsch, I. *Analytical Chemistry* **2010**, *82*. 7068-7072.

(37) Weston, M. C.; Fritsch, I. *Sensors and Actuators B-Chemical* **2012**, *173*. 935-944.

(38) Weston, M. C. *Redox-magnetohydrodynamic (MHD) microfluidics : fundamentals, optimization, and applications to analytical chemistry,* **2010**.

(39) Anderson, E. C. *Redox magnetohydrodynamic (MHD)-induced fluid convection and its applications in analytical chemistry*, **2006**.

(40) Scrape, P. G.; Gerner, M. D.; Weston, M. C.; Fritsch, I. *Journal of the Electrochemical Society* **2013**, *160*. H338-H343.

(41) Gao, X. P.; Lee, J.; White, H. S. *Analytical Chemistry* **1995**, *67*. 1541-1545.

(42) Gerner, M. D. *Factors Affecting Redox-Magnetohydrodynamics for Flow in Small Volumes*. University of Arkansas, fayetteville, **2009**.

(43) Lee, S. J.; Kim, S. *Microfluidics and Nanofluidics* **2009**, *6*. 577-588.

(44) Lindken, R.; Rossi, M.; Grosse, S.; Westerweel, J. *Lab on a Chip* **2009**, *9*. 2551-2567.

2. Flat Flow Profiles Achieved with Microfluidics Generated by Redox-Magnetohydrodynamics (MHD)

2.1 Abstract

Horizontal flow profiles having uniform velocities (3-13% RSD) at fixed heights across 0.5, 2.0, and 5.6 mm widths, with magnitudes of ≤124.0 μm/s, can be sustained along a ~25.0 mm path using redox-magnetohydrodynamics (MHD) microfluidic pumping in a small volume (14.3 mm wide × 27.0 mm long × 620. μm high) on a chip. Uniform velocity profiles are important in moving volume elements without shape distortion for assays and separations for lab-on-a-chip applications. Fluid movement resulting from the MHD force ($\mathbf{F_B} = \mathbf{j} \times \mathbf{B}$) was monitored with video microscopy by tracking 10-μm, polystyrene latex beads mixed into the solution. The ionic current density, **j**, was generated in 0.095 M $K_3Fe(CN)_6$, 0.095 M $K_4Fe(CN)_6$, and 0.095 M KCl by applying a constant current across a 0.5, 2.0 or 5.6 mm gap between an anode-cathode pair of electrodes, consisting of one to four shorted parallel, coplanar gold microbands (each 25.0 mm × 98 μm × ~100 nm (thickness), and separated by 102.0 μm) fabricated on an insulated silicon substrate. By shorting the increasing numbers of microbands together, increasing currents (118, 180, 246, and 307 μA) could be applied without electrode damage, and the impact of ionic current density gradients on velocity profiles over the anodes and cathodes could also be investigated. The magnetic field, **B**, was produced with a 0.36 T NdFeB permanent magnet beneath the chip. Data analysis was performed using particle image velocimetry software. A vertical flow profile was also obtained in the middle of the 5.6 mm gap.

2.2 Introduction

Redox-magnetohydrodynamics (MHD) is relatively new and promising for use as a pumping technique, which is shown here to generate controlled, flat flow profiles in a small fluid volume over large distances. This is accomplished over a chip under laminar flow conditions (Reynolds number < 1) when a constant current is applied at the on-chip electrodes in the presence of an externally applied magnetic field. A uniform, flat flow profile is important for allowing undistorted sample transport to assist with multiple and parallel analyses on a single chip, and therefore providing a desirable advantage for lab-on-a-chip based systems such as immunoassays, DNA hybridization assays, and separations, whereas, non-uniformities can adversely affect analytical results.[1, 2]

Lab-on-a-chip technologies hold promise for point-of-care diagnostics, bioanalysis and environmental monitoring, in locations remote from laboratories due to their small size, portability, rapid analysis, and possibility of integrating and automating complex laboratory procedures on a single hand held device.[3-10] Microfluidics[3, 8-11] is important for transporting small volume elements onto and within the device. Common approaches are pressure (e.g. mechanical pumping) and electroosmosis.[12, 13] Under laminar flow conditions (Reynolds number < 1), a pressure difference gives rise to a parabolic profile in a channel and hence varied fluid velocities. Electroosmotic pumping provides a flat profile, but requires the fabrication of microchannels which limits design options and a high voltage for its operation, which can lead to problems of heat generation, bubble formation, and electrode degradation.[14] Redox-MHD allows more flexibility in device design, avoids electrode degradation, and offers the intriguing prospect that simply through judicious control of ionic current density and magnetic field, it is possible to fine tune the flow profile, such as making it flat over large dimensions. We have previously

reported relatively-flat horizontal fluid flow profiles using applied-potential[15] and applied-current[16] redox-MHD over a 650 μm spacing between oppositely biased, 2-mm long electrodes and showed that fluid velocity increases proportionally with the magnitude of the current for a fixed cell geometry.[16] Here, we combine this knowledge to engage in methodical studies of tuning flow profiles by redox-MHD on much larger dimensional scales that are suitable for lab-on-a-chip applications.

MHD is governed by the right hand rule, $\mathbf{F_B} = \mathbf{j} \times \mathbf{B}$ (the magnetic part of the Lorentz force equation). Here **j** is the ionic current density of a fluid element (C/m^2), **B** (Tesla) is the magnetic flux density, and $\mathbf{F_B}$ (N/m^3) is the MHD body force acting on the fluid element.[17-19] Introduction of easily oxidizable and reducible chemical (redox) species to the fluid can sustain a faradaic current at low overpotential, and is coined "redox-MHD". It provides the ionic current density needed for the MHD force and avoids electrode corrosion and bubble generation due to water electrolysis at high voltages required for MHD in supporting electrolyte alone.[20-23] Redox-MHD microfluidics offers multidirectional and channel-less fluid flow,[24] with several degrees of freedom in selecting parameters to control velocities, [15, 16, 25] and compatibility with aqueous and non-aqueous solutions.[26]

The extent to which redox-MHD microfluidic pumping produces flat flow profiles over a chip under different experimental conditions was explored by applying a current between long, individually-addressable, parallel microband electrodes on a chip and using an NdFeB permanent magnet beneath it (Figure 2.1). Horizontal and vertical flow profiles were investigated. Reduction of ferricyanide and oxidation of ferrocyanide at the electrodes in the thin layer of potassium chloride solution containing polystyrene latex microbeads in the small cell over the chip (Figure 2.2)

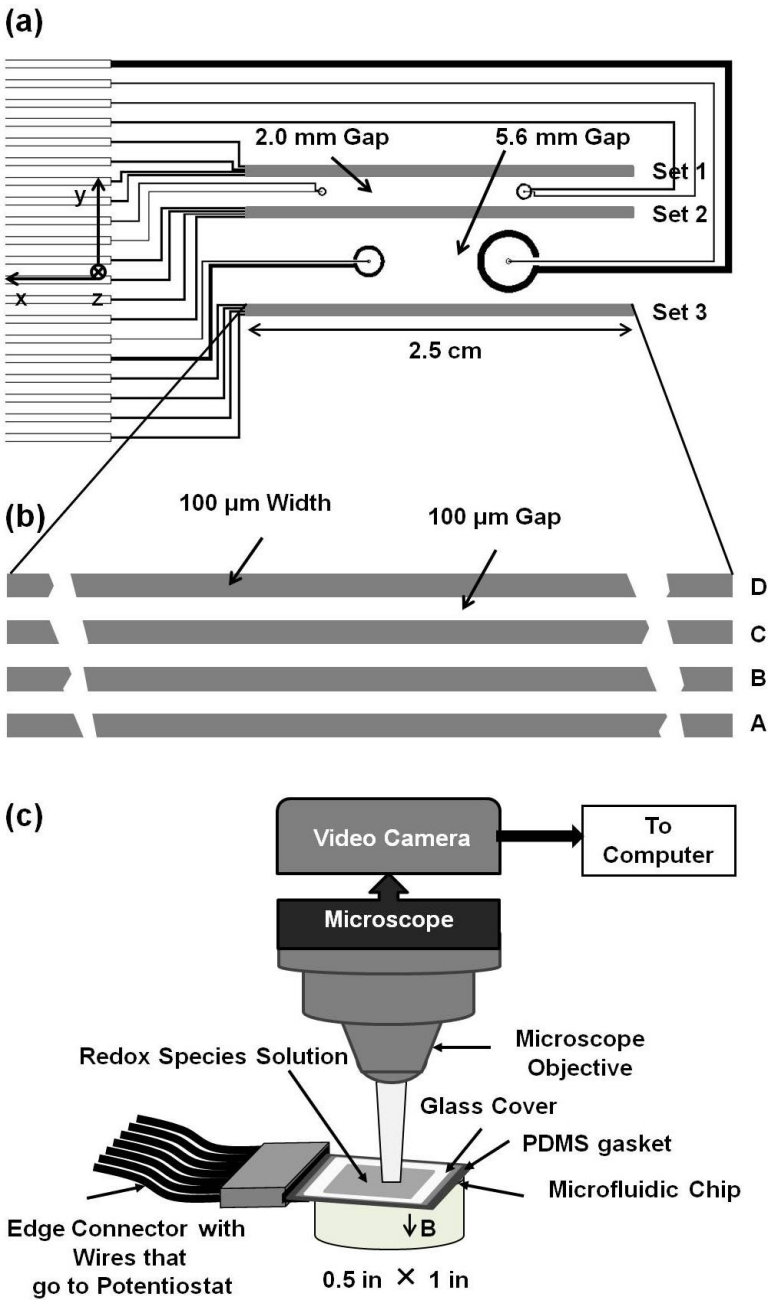

Figure 2.1 Top down schematic of the electrode chip design, which includes 12, individually-addressable microband electrodes, which are 25.0 mm long × 98 ± 0.1 µm wide × ~100 nm thick. They are arranged in three sets of four electrodes each, with the designations "set 1", "set 2", and "set 3", as shown in the figure. (Ring/disk microelectrodes of different sizes are also present on the chip, but they were not used for the studies herein.) The intra electrode gap within each set of microbands is nominally 100 µm, whereas the interset gaps are 2.0 (between sets 1 and 2) and 5.6 mm (between sets 2 and 3). **(b)** Expanded view of four electrodes in one of the sets, showing microband (dark gray) width and gap dimensions. **(c)** Setup used for redox-MHD microfluidics experiments.

allowed current to be sustained while the fluid flow was monitored by tracking the beads using video optical microscopy (Figure 2.1c).

2.3 Experimental Section

2.3.1 Chemicals and Materials

See Supporting Information.

2.3.2 Electrode Chip Design

The 2.0 in. (length) × 1.0 in. (width) chip contains several patterned gold features (see fabrication procedure in Supporting Information) but only the microband electrodes were used for this work (Figure 2.1a). The chip has three parallel sets of microband electrodes with interset gaps of 2.0 and 5.6 mm, and each set contains four individually addressable electrodes having dimensions of 25.0 mm (length) × 98.0 ± 0.1 μm (width) × ~100 nm (thickness, based on an uncalibrated piezoelectric monitor of the thermal evaporator). The interelectrode gap between microband electrodes within each set is 102.0 ± 0.1 μm (Figure 2.1b).

2.3.3 Experimental Setup

The electrical connection between the electrode chip and the CHI 760B bipotentiostat (CHI Instruments, Austin, TX) was made via an edge connector (solder contact, 20/40 position, 0.05 in. pitch) purchased from Sullins Electronics Corporation, San Marcos, CA. All studies involving electrochemistry were performed at room temperature with an equimolar mixture of potassium ferricyanide (0.1 M) and potassium ferrocyanide (0.1 M) in a potassium chloride solution (0.1 M). A 1.0 mL aliquot was mixed with 50.0 μL of polystyrene latex microbeads for fluid flow measurements, changing concentrations to 95% of the original values. The individual

microband electrodes were characterized using cyclic voltammetry (CV). CV responses (Figure 2.S1) and comparison with expected behavior are given in the Supporting Information.

MHD fluid flow can be induced either by directly applying a current or potential at electrodes in the presence of a magnetic field. Because the MHD force, and therefore the fluid flow, depends linearly on current,[16] it is the current that was controlled here (using chronopotentiometry, CP) to achieve the best precision. Applied currents were ≤70% of the mass transfer limit from chronoamperometry (CA) responses. (See Figure 2.S2 and Supporting Information for details).

In redox-MHD studies, a "two-electrode setup" was used where one, two, three, or four microband(s) were shorted as working anode(s), and the same number of microband(s) across the interset gap were shorted as the combined counter/reference cathode(s). Electrodes from set 1 were used as the anode(s) and the corresponding electrode(s) in set 2 served as the cathode(s) for experiments with the 2.0 mm interset gap (Figure 2.S3a in Supporting Information). For experiments with the 5.6 mm interset gap, set 2 electrode(s) served as the anode(s), and set 3 electrode(s) served as the cathode(s) (Figure 2.S3b in Supporting Information). .

A PDMS gasket with a rectangular opening (14.3 mm wide, 27.0 mm long and 620.0 μm thick), placed directly over the chip, formed the sidewalls of the electrochemical cell for redox-MHD studies, leaving the microband electrodes exposed to the solution (Figure 2.S4, in the Supporting Information). A 300. μL aliquot of solution was dispensed onto the chip within the PDMS boundary and covered with a microscope glass slide, thus making a closed electrochemical cell with a height defined by the PDMS thickness. This completed assembly was placed on the magnet on stage of a light microscope (LEICA DM 2500M) and bead movement was recorded using an attached SONY HDR-XR 500V camcorder (Figure 2.1c).

Fluid velocities were quantified by processing the bead movement in the videos using particle image velocimetry, PIV (Dantec Dynamics), software.[25] Horizontal flow profiles parallel to the chip surface, across the gap between the anode(s) and cathode(s), at a fixed height, and equidistant from the ends of the microbands were obtained. Vertical flow profiles (perpendicular to the electrode chip, centered between the edges and ends of the activated microband electrodes) were obtained by raising the microscope focus to change the velocity measurement height within a single experiment. Between experiments, the assembly was rinsed with deionized water, dried with ultrapure argon gas, and a fresh volume of redox-bead solution was introduced for the next experiment. Further details about recording the videos and their timing are given in the PIV section of the Supporting Information.

2.4 Results and Discussion

2.4.1 Horizontal Flow Profiles for Different Electrode Configurations and Gaps at a Fixed Applied Current

Relatively flat flow profiles were observed in the horizontal plane in the y-direction that were produced by redox-MHD in the two large interset gaps (see Figure 2.3), and for the smaller intraset gap (Figure 2.S5) for the same, constant applied current and at a fixed height above the chip surface (just below the half-way point to the lid). Table 2.S1 in the Supporting Information provides averages and pooled standard deviations for the velocities across the *central region* of the gaps, covering the inner 4.61 ± 0.06 mm for the 5.6 mm interset gap, 1.39 ± 0.06 mm for the 2.0 mm interset gap, and the entire 500 μm for the intraset gap. The data for the 5.6 mm and 2.0 mm gaps are between the estimated diffusion lengths extending from the electrodes (~400 μm and ~250 μm, respectively). For the 500 μm gap, the average includes the diffusion layers. In addition, highly linear fluid flow was observed essentially along the entire length of the gaps. A

representative PIV processed image used to quantify velocities and showing the straight fluid path at the center of a gap is given in Figure 2.S7 of the Supporting Information. Figure 2.S8 of the Supporting Information demonstrates that the linear flow continues until it reaches the ends of the active electrodes. In the last ~700 μm the fluid begins to turn around to flow in the reverse direction along the outer sides of the active electrodes to form a flow loop in a manner similar to redox-MHD for much smaller reinforcing flow designs.[15, 16] In the rest of this paper, we focus on flow profiles halfway between the ends of the electrodes, where flow patterns are straight, simplifying the analysis.

Figure 2.2 helps to explain these phenomena. The ionic current is produced across the gap between anodes and cathodes by applying an external electronic current between them. Electrons originating at the anode by converting $Fe(CN)_6^{4-}$ to $Fe(CN)_6^{3-}$ in the solution at a low overpotential are sent through the external circuit using the galvanostat and arrive at the cathode to convert $Fe(CN)_6^{3-}$ to $Fe(CN)_6^{4-}$ (Figure 2.2a). In a static solution, ions move in response to a concentration gradient (such as those produced by electrolysis at the electrodes) and to compensate for the change in charge at the electrodes (i.e. respond to the resulting electric field and dominated by migration[27-29]), thus completing the circuit. Ions that are both negative and positive may move from anywhere in solution, but there must be a net positive ion movement from anode to cathode and a net negative ion movement from cathode to anode, the sum of which produces a net **j**. A large component of the magnetic field from the underlying magnet is perpendicular to **j** (see Figure 2.S6 in Supporting Information) and together they generate $\mathbf{F_B}$ within the gap from one end to the other, along its length, resulting in fluid flow in that direction (Figure 2.2b). Thus, the localized **j** and **B** (and their relative location to the walls of the solution compartment) define the fluid flow pattern and profile. The straight flow suggests that the j_y and

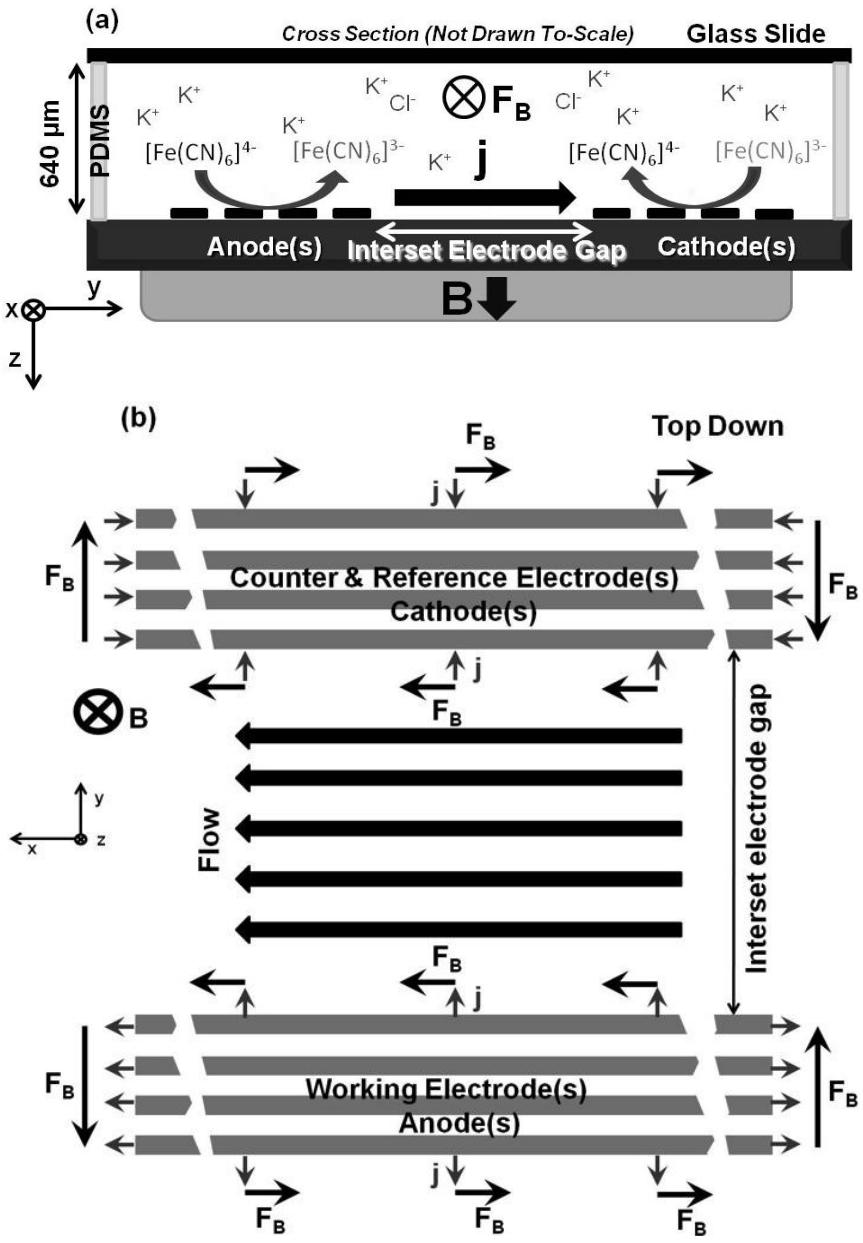

Figure 2.2 Schematics of electrochemical processes, ionic current, and magnetic field that give rise to the MHD force and fluid flow. (a) Cross sectional view for a given interset gap. Electrochemical oxidation at one set of microband electrodes and reduction at the other set of microband electrodes produce the ionic current **j** in the interset gap. Where **j** is perpendicular to **B** from the external magnet, a non-zero $\mathbf{F_B}$ is produced and the fluid moves there parallel to the electrodes. (b) Top down view of these forces.

B_z components in that region must be fairly uniform along the entire length of the gap. By neglecting small changes in local potential in the gap along its length (in the x-direction), the electric potential distribution can be limited to a two dimensional plane (y, z), where for a fixed height, z, there is minimal variation along the y plane of the electric field between active electrodes. If this is the case, then it will generate a fairly flat flow profile (Figure 2.2).

Consider in detail the horizontal flow profile across the 2.0 mm gap between electrodes for the one-electrode configuration in Figure 2.3a. It is statistically flat at the 95% confidence level over 82% of the central 1.39 ± 0.06 mm portion. Interestingly, the shape of the profile across the gap is asymmetric, where it is statistically flat over 100% of a stretch of 1.03 mm skewed toward the anode side (from -400 μm to +670 μm) with a speed of 64.5 ± 2.5 μm/s (3.9% RSD). Also, the speed drops over the electrodes with distance more steeply over the anode than over the cathode.

To better understand these features, and to demonstrate how tuning a flow profile by redox-MHD may be possible, it is of interest to activate increasing numbers of anodes and cathodes, while maintaining the same gap size (2.0 mm) and electronic current (120 μA). The resulting horizontal flow profiles are also shown in Figure 2.3a. One outcome is that the average fluid velocity across the central portion of the gap at a fixed height decreases (See Table 2.S1 in Supporting Information). (The trend is statistically significant when comparing the one- to the four-electrode case.) The largest percentage of measured velocities that are statistically identical at the 95% confidence level over the central portion of the 2.0 mm gap is also less than in the one-electrode case. These are 50%, 58%, and 67% which correspond to 64.1 ± 2.1, 61.9 ± 2.2, and 61.0 ± 1.9 μm/s, for the two-, three-, and four-electrode configurations, respectively. The region where velocities are most statistically identical is also skewed toward the anode, on

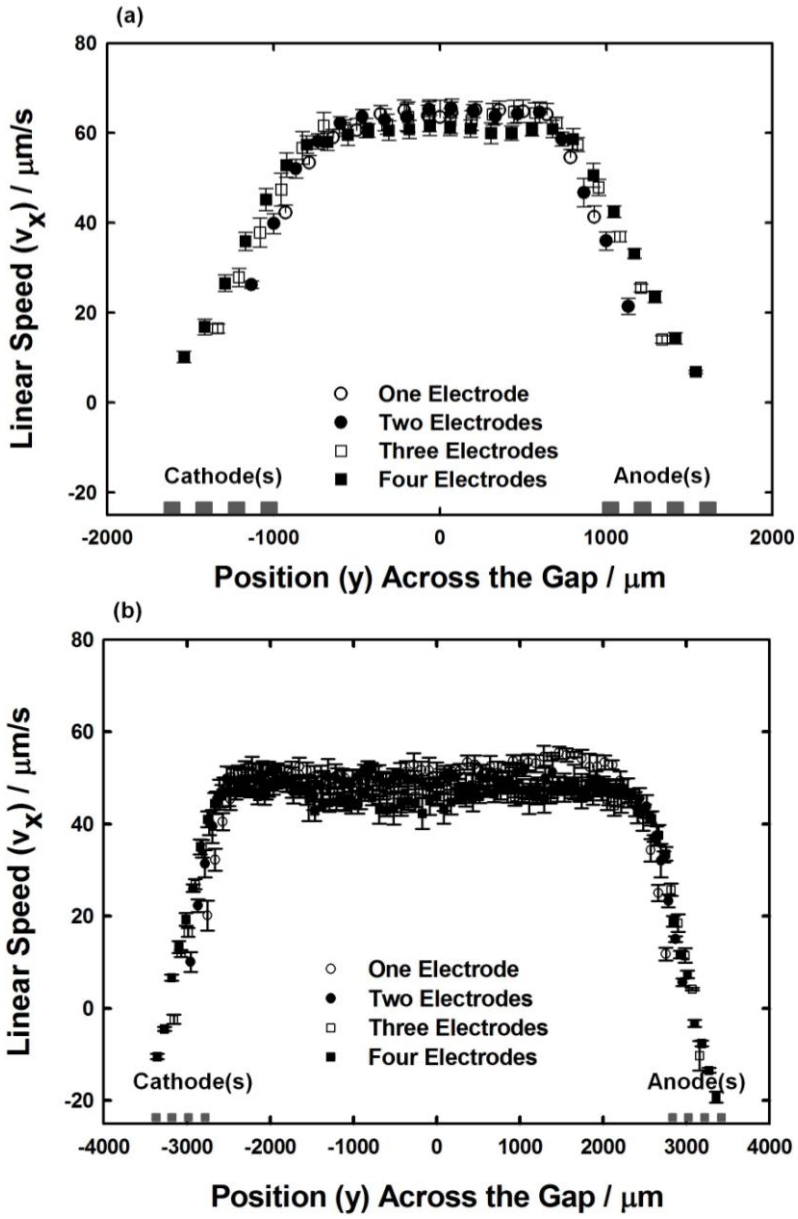

Figure 2.3 Horizontal flow profiles for different electrode configurations for a fixed applied current of 120 μA. The velocity (v_x) was measured as a function of position in y at a constant z plane (270.0 and 245.0 μm above the chip surface) across the **(a)** 2.0 mm and **(b)** 5.6 mm interset gaps, respectively. The profiles in (a) were obtained with electrode assignments shown in Figure S-3a. Each of those profiles was derived from a single experiment, where three regions were video-recorded, starting at the anode side and ending at the cathode side. Bead velocities were analyzed over a 3 to 5 s interval starting at 15, 45, and 65 s after the current was applied, which correspond to regions one, two, and three, respectively. The total run time was 85 s. The profiles in (b) were obtained with the electrode assignments shown in Figure S-3b. Each of those profiles was derived from multiple experiments, in which bead movement was recorded in a different lateral location. There were three experiments for 1- and 2-electrode configurations and four for 3- and 4- electrode configurations. Analysis of bead velocities in each of those regions involved a 3-5 s interval at 120 s after the current was applied, and a total run time of 150 s.

average, just as in the case for the one-electrode configuration, over a stretch of 1.19 ± 0.18 μm from -530 ± 150 to +660 ± 50 μm.

Although the net ionic current remains unchanged, it is the ionic current density that decreases overall, because of the increased electrode area, causing a decrease in $\mathbf{F_B}$ and therefore in velocity. It is important to note that although the electronic current density at the electrodes decreases with increasing numbers of electrodes so that at the four-electrode configuration it is only 25% of that at the one-electrode configuration, the average velocity in the gap has only decreased to 95%. This result emphasizes that redox-MHD fluidic devices must be designed with the ion paths in mind. In this case, the thin cross section of electrolyte between anodes and cathodes has remained the same so that the ionic current density in the gap has only diminished slightly. A design consideration, then, is that an increase in electrode area is possible, which allows higher currents and therefore higher velocities to be attained, without drastically changing the shape of the flow profile.

The effect of changes in ionic current density on fluid velocity is especially noticeable directly over the electrodes, however, in the form of three characteristics. (See the expanded plots of velocities in these regions in Figure 2.S9 of the Supporting Information). One is that there is a linear decrease of velocity with position over the active electrodes, for which the average R^2 values from a least squares fit of the data is 0.997 ± 0.003. (Equations for the lines and x-intercepts are included in the Figure caption for Figure 2.S9.) This occurs because the greatest ionic current density for a thin cross section of electrolyte between co-planar electrodes[30] should be at the inner edge of the innermost set of active electrodes (A of set 1 and D of set 2) and drop off going outward (away from the gap) at the second, third, and fourth electrodes. The second characteristic is that there is a weaker dependence of velocity on distance

as the number of electrodes increases, because ionic current density decreases, yielding shallower slopes. The slopes are also significantly steeper over the anodes than over the cathodes for the three- and four-electrode configurations, confirming the presence of asymmetry. The third characteristic is that the x-intercepts from the best fit lines, where the velocity is expected to be zero (center of the elliptical vortex) and where the fluid flow changes direction, is also further from the gap with increasing numbers of electrodes. Interestingly, these "zero-velocity" positions expand outward, even beyond the position of the active electrodes, in increments of only 120 to 150 μm although the corresponding geometric width of the electroactive regions increase in increments of 200 μm. This could be a consequence of the larger contribution of a vertical component to the ionic current relative to the horizontal component there that cannot contribute to $\mathbf{F_B}$ because the cross product with **B** would be zero. Also, the current density across that increment cannot be uniform because only half its width is occupied by a band electrode.

Now consider in detail the horizontal flow profiles produced with the same current (120 μA) in a cell of the same height but across the much wider 5.6 mm interset gap for the different electrode configurations shown in Figure 2.3b. In general, the trends with increasing numbers of activated electrodes are similar to those for the 2.0 mm gap. The average velocity across the gap decreases (see Table 2.S1 in Supporting Information), the decline of velocity with distance over the electrodes becomes shallower, and the reversal point of the flow occurs farther from the center of the gap. There is also asymmetry in the shapes of these profiles. For example, as shown in Figure 2.S10 of the Supporting Information, the x-intercept of the best line fit for the declining velocity over the electrodes, which represents the estimated flow reversal point, shifts outward and with diminishing increment size with increasing numbers of active electrodes, and appears closer to the center of the gap over the anodes than over the cathodes, as is the case for the 2.0

mm gap. The negative velocities measured on the other side of the flow reversal point, lie near the extension of the line produced from the positive velocities, thus, supporting this approach to estimate the flow reversal location. (Note that although measurements were made 25 μm closer to the electrode chip than in the 2.0 mm case, they are not expected to vary more than 5% for a given interset gap, based on the vertical profile study below. Thus, a direct comparison between results at the 2.0 mm and 5.6 mm interset gaps should be valid).

There are several characteristics of the flow profiles for the 5.6 mm interset gap that differ from those of the 2.0 mm interset gap, however. These can be attributed to an increased contribution of ions from solution beyond the ends of the gap to the ionic current, thereby leading to nonuniformities in **j** and decreasing the magnitude of its y-component across the gap. One consequence of this effect is that the average of the velocities across the 5.6 mm gap for the electrode configurations is 77.6 ± 2.3% of the values across the 2.0 mm gap. Intriguingly, however, the dependence of the average velocity decreases approximately linearly with increasing numbers of activated electrodes (R^2 = 0.989). The direction of the fluid flow between the anodes and cathodes of the 5.6 mm gap is still impressively straight, and fairly flat (≤5.1% RSD). The greatest percent of velocities across the central 4.61 ± 0.06 mm span that are statistically identical at the 95% confidence level are: 33%, 51%, 49%, and 44%, which correspond to 51.0 ± 2.1, 49.8 ± 2.5, 47.6 ± 2.4, and 47.1 ± 1.7 μm/s average speeds for one-, two-, three-, and four-electrode configurations, respectively. Statistical analysis confirms that the fluid speed dips near the center of the gap and is most noticeable for electrode configurations with a larger electroactive area, and covers a region skewed toward the cathode (e.g. from -1700 to +200 μm for the four-electrode configuration). The other electrode configurations also have velocities that are statistically depressed in this region, although the breadth of the dip is not as

obvious. The decline of velocity with distance directly over the electrodes (Figure 2.S10 of Supporting Information) is not as linear ($R^2 = 0.980 \pm 0.011$) as in the case for the 2.0 mm gap and slopes from the least squares fit to the data are not steeper over the anode than the cathode. Also, the x-intercept of those lines have shifted to positions over the activated electrodes that are closer to the gap than for the 2.0 mm case where the flow reversal point can be on the outer sides of the activated electrodes.

Understanding factors responsible for the flow profile asymmetry is important for achieving fine tuning of fluid flow using redox-MHD. Asymmetry in the direction or magnitude of the ionic current density and magnetic flux density, as well as the wall placement relative to the active electrodes are possible reasons. Figure 2.S6 in the Supporting Information shows the distribution of **B** and the B_z component throughout the cell. The variation in B_z along the z- and y-directions for both the 2.0-mm and 5.6-mm interset gaps is insufficient to account for the asymmetry in the velocity profiles. Table 2.S2 in the Supporting Information compares velocities in the gap that are near the anode, in the center, and near the cathode to the B_z component of the magnetic field at the same positions. For example, the 2-mm interset gap is not centered on the magnet, and the magnitude of B_z increases by 0.73% from cathode to anode. However, this change in B_z cannot completely explain the 3.9% increase in velocity between those two regions for the one-electrode configuration. The 5.6 mm interset gap is more centered on the magnet, and thus there is a decrease in B_z of 0.1% from the anode to the middle of the gap and 0.6% for that from the cathode. However, the velocity decreases by much more ~3.0 and 3.6%, respectively, between these locations for the four-electrode configuration. In addition, the lowest point of B_z lies just to the anode side of the center of the gap, not near the cathode where the depression in the velocity profile resides.

Location of the sidewalls is not likely an explanation for the asymmetry. One would expect a faster reverse velocity to accommodate the smaller volume at electrodes that are closer to the side wall, and thereby sharpen the profile's edge there. However, the nearest sidewall is much closer to the anode in studies of the 2.00 mm interset gap but closer to the cathode for studies of the 5.6 mm gap, without a corresponding asymmetry in the velocity profiles.

A variation in ionic current density across the gap is more likely to make a larger contribution to the flow profile asymmetry. A slight variation in cell height (e.g. tilt of the lid relative to the electrode chip) from cathode to anode would lead to both a variation in ionic current density as well as viscous forces across the gap. If the tilt is biased the same way with every experiment, then this could explain the similar asymmetry of the 2.0 and 5.6 mm interset gap studies.

Another factor specific to the anode and cathode is a change in mass density from faradaic conversion of a chemical species of a given charge to one of higher or lower charge, and thus attracting a greater or fewer number of counterions, respectively. This phenomenon can lead to variation in natural convection and ionic resistance across the gap. Natural convection under conditions similar to those described here is significant at long time scales (>20 s) and are under investigation.[31] Essentially, at the anode, which is facing upward, fluid will eventually rise when each $Fe(CN)_6^{4-}$ with four associated K^+ is converted to $Fe(CN)_6^{3-}$ and only three associated K^+. The net departure of K^+ ions produces a less dense fluid element there. The opposite reaction occurs at the cathode, resulting in the denser fluid element spreading outward along the floor of the chip, with a less dramatic impact on convection than at the anode. However, density gradients cause circulation of fluid across the gap and at a lower speed ($\leq 1/10^{th}$), and thus it is not clear at this time how it affects the asymmetry of the net redox-MHD flow. How the

developing diffusion layer and natural convection over time affect the flow profile across the gap is a matter for further study. A horizontal flow profile using a much narrower (intraset) gap of 500.0 μm for a one-electrode configuration for the same current and similar height was also obtained, and is compared to profiles of the wider interset gaps in the Supporting Information (Figure 2.S5).

2.4.2 Horizontal Flow Profiles for a Fixed Electrode Configuration with Different Applied Currents

Increasing current for a fixed electrode configuration is expected to increase ionic current density, without substantially changing the ionic current density distribution. Thus, we would expect that the flow patterns should remain the same, but with speeds proportional to the increase in current. This situation is important for tuning fluid speeds without altering flow patterns and supported by studies on a different electrode geometry where fluid speed was confirmed to be proportional to both the applied current and magnetic field.[16] What is unique here, however, is the much larger scale and the dependence of the speeds over the active electrodes where an ionic current density gradient occurs, which clearly confirms this concept.

Figure 2.4a shows the horizontal flow profiles attained for the 5.6 mm interset gap using the four-electrode configuration, at 280 μm from the chip, but with different applied currents (118, 180, 246 and 307 μA). (The slight difference in measurement height from those of the other horizontal profiles, ≤ 35 μm, should influence the velocities ≤ 5%.) The average velocity across 4.61 ± 0.06 mm of this large gap (see Table 2.S1 in Supporting Information) is fairly uniform (with a RSD of 4.4% for 118 μA, 3.5% for 180 μA, 3.2% for 246 μA, and 3.5% for 307 μA) and has an excellent linear dependence on current ($y = 0.367 \pm 0.007$ (μm s^{-1} μA^{-1}) $x + 1.9 \pm 1.5$ (μm s^{-1}), $R^2 = 0.999$). No particular trend is observed regarding the magnitude of the dip in

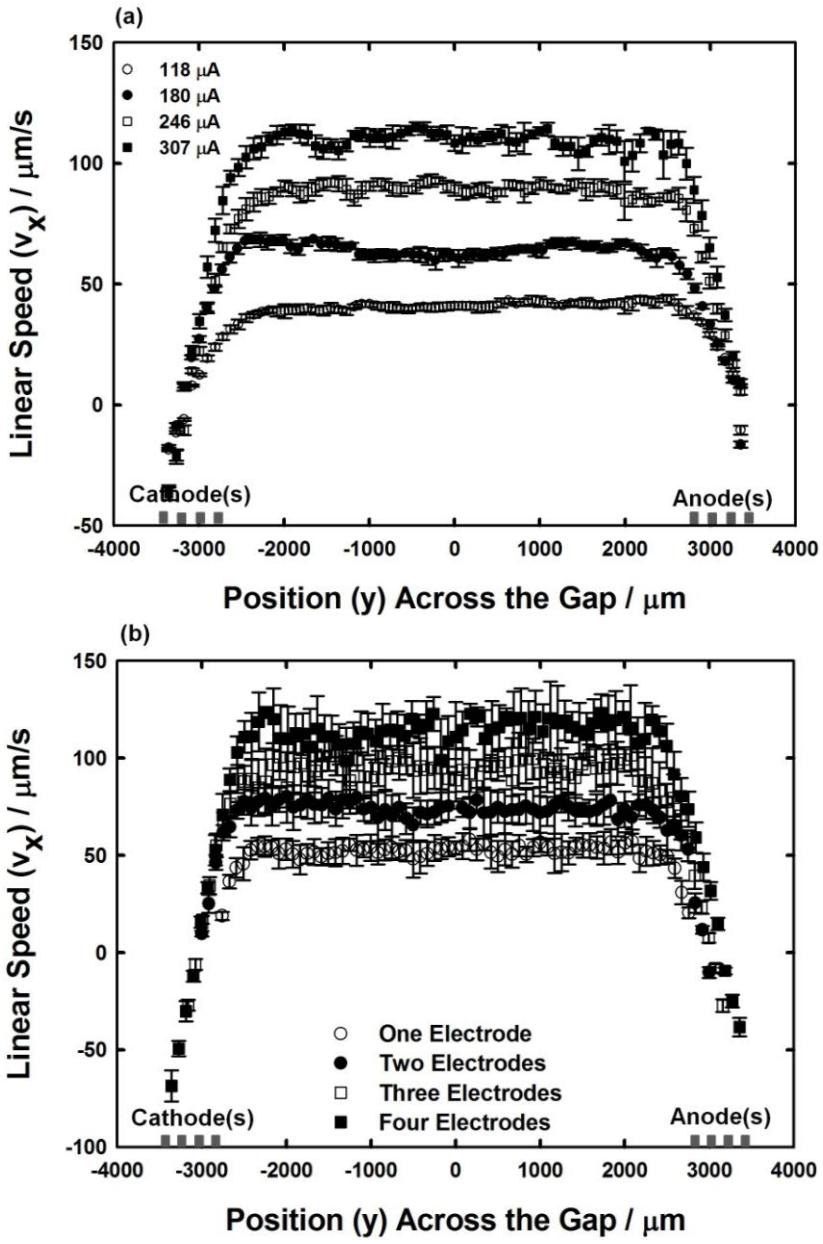

Figure 2.4 Horizontal flow profiles at a constant z plane (280.0 μm above the chip surface) across the 5.6 mm interset gap for (a) different applied currents at the four-electrode configuration and for (b) configurations with different numbers of electrodes with applied currents at 70% of the mass transfer-limited values (the same currents as in (a). The profiles were obtained with the electrode assignments shown in Figure S-3b. For (a), four experiments were performed to determine the profile when the current was 180 μA, and only three when the current was 118, 246, and 307 μA. In addition, analysis of bead velocities in each of the regions was performed at 120 s after the current was applied, and the total run time was 150 s. For (b), the procedure was as described in Figure 3b. In addition, analysis of bead velocities in each of those regions involved a 3-5 s interval at 140 s after the current was applied, and a total run time was 150 s.

speed near the center of the profile with current, but the dip is especially noticeable for the 180 μA case, and skewed toward the cathode side, as above. The decline in speed over the active electrodes (the slope of the best fit line to positive speed vs. location over the electrodes) is proportional to current (R^2 = 0.985 and 0.997 for the cathode and anode sides, respectively) and the flow reversal point at a given set of electrodes is similar for all the currents (3220 ± 36 and 3440 ± 65 μm for cathode and anode sides, respectively).

Thus, the ionic current density distribution does indeed appear to remain the same, only the magnitude changes. The reversal point is farther away at the anode side than at the cathode side, showing that the asymmetry is also preserved across the different currents.

2.4.3 Horizontal Flow Profiles for Different Electrode Configurations, each with Applied Current at 70% of the Mass Transfer Limit

By increasing the number of active electrodes to generate redox-MHD, higher currents can be applied, and thus an increase in the MHD force and fluid velocity can be achieved without damaging the electrodes. The studies above with increasing numbers of active electrodes involved a fixed applied current. Here, we also increase the applied current with increasing numbers of active electrodes. A series of studies was performed using the 5.6 mm interset gap with applied currents of 118, 180, 246 and 307 μA, which were at 70% of the mass transfer limited values obtained from CA data for one, two, three and four electrode configurations, respectively. The resulting horizontal flow profiles are shown in Figure 2.4b that show fluid flow characteristics that exhibit a combination of features that are described above for the case of increasing electroactive area with a fixed current and for the case of increasing current for a fixed electroactive area. The horizontal flow profile is fairly uniform across the gap. The average fluid velocity over the central 4.61 ± 0.06 mm region increases proportionally with current, and the

dependence ($y = 0.324 \pm 0.006$ (μm s^{-1} μA^{-1}) + 15.0 ± 1.3 μm s^{-1}, $R^2 = 0.999$) is linear as for a fixed electrode configuration, despite the diminishing electronic current density that for the four-electrode configuration is 65% of that for the one-electrode configuration. The fluid reversal points over the electrodes are closer together than for the fixed current case because the loss in ionic current density is more apparent there with increasing electroactive area offset by the increase in current.

Finally, the repeatability of these redox-MHD experiments is excellent, as can be seen by comparing results for similar conditions for the different studies described here. For horizontal profiles, compare Figures 2.4a and 2.4b for 307 μA at the four-electrode configuration, Figures 2.3b and 2.4a for 120 and 118 μA for the four-electrode configuration, and Figures 2.3b and 2.4b for 120 and 118 μA for the one-electrode configuration. See Table 2. S1 in the Supporting Information to compare the average velocities under these conditions.

2.4.4 The Vertical Flow Profile for a Single Electrode Configuration and a Fixed Applied Current

For the set of experiments described in this section, fluid flow was determined in the z direction. This study was performed with the 5.6 mm interset gap and four-electrode configuration, using 70% of the mass transfer limited applied current (307 μA). The measurement heights of 100, 200, 300, 400, 500, and 550 μm were fixed by the microscope focus adjustment (Figure 2.5a). The fluid velocity is small closer to the chip, increases with height, and then decreases again as it reaches the lid (Figure 2.5b). A parabola, which would be the expected vertical profile for pressure-driven flow, is not a good fit to the data, producing an R^2 value of only 0.97. The maximum velocity is closer to the electrode chip than the lid. This

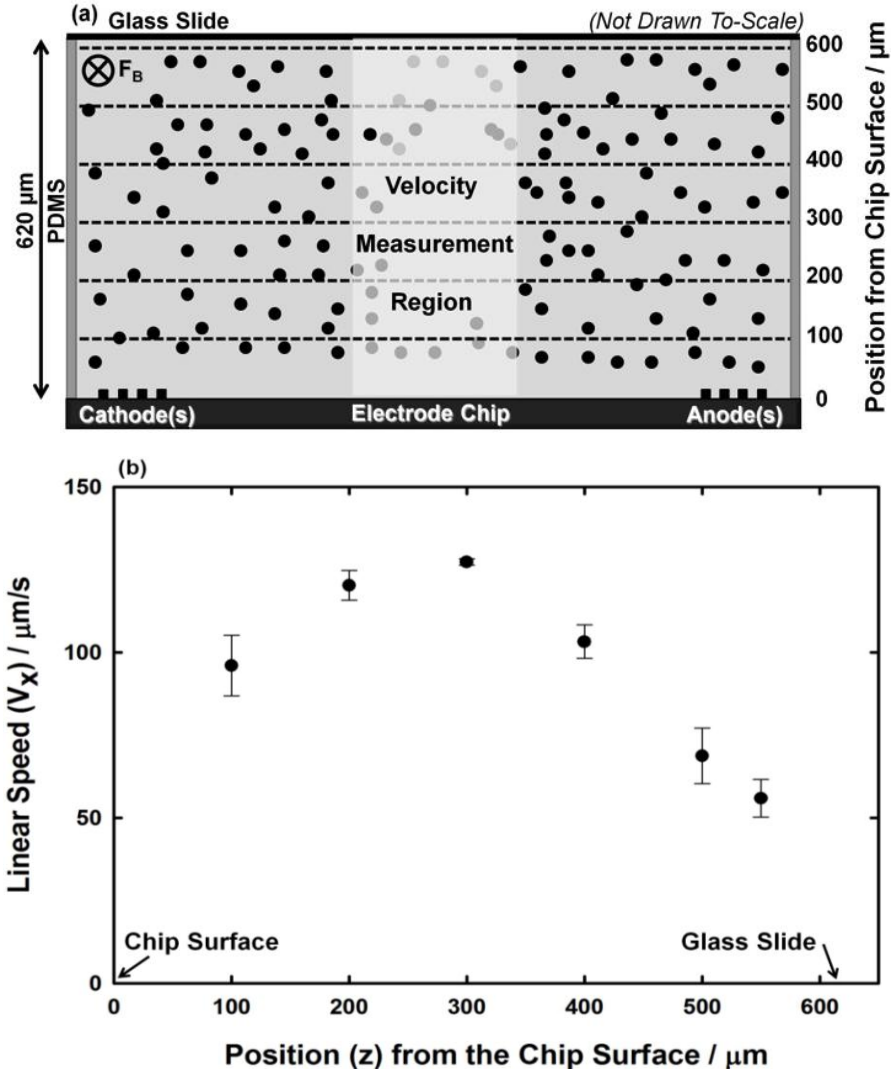

Figure 2.5 Vertical flow profile for the 5.6 mm interset gap using the four-electrode configuration. (a) Cross sectional schematic illustrating the region and positions from the chip where velocities were measured. The region is at the center of the gap and half-way from both ends of the microband electrodes. (b) The vertical flow profile was determined starting near the electrode chip and ending near the lid at 15, 40, 65, 90, 115, and 140 s after the application of the current (307 µA).

shape was observed previously for a vertical profile within a much smaller gap (650 μm) and electrode length (2 mm),[15] and was attributed to a larger MHD force near the electrode side of the cell where the current originates. If this reason is correct, then the ionic current density remains larger near the electrode chip on a much larger scale, as well, even with a gap that is 8.6 times in width and electrodes that are 12.5 times in length. The ramification of this result is that the velocity profiles appear to be scalable.

2.5 Conclusions

Horizontal flat flow profiles using redox-MHD microfluidics between parallel band electrodes have been evaluated for a fixed height and for different applied currents and gaps. A non-parabolic vertical flow profile was also obtained, although it is not flat. Based on the results for the horizontal profiles that clearly depend on the ionic current density distribution, this should also be tunable and will be addressed in future studies. The results herein demonstrate that tunable fluid flow and with flat profiles are achievable by redox-MHD on scales (several centimeters) consistent with lab-on-a-chip devices, and across larger breadths and with larger volumes than shown for electroosmotic flow. Thereby it is possible for redox-MHD to be applied to chip-based chemical analysis with minimal distortion of sample transport, and hence will facilitate multiple, parallel analysis in a single platform.

2.6 Acknowledgments

We are thankful to the National Science Foundation (Grant number: CHE-0719097), and the Arkansas Biosciences Institute, the major research component of the Arkansas Tobacco Settlement Proceeds Act of 2000, for their financial support. We also acknowledge Matthew D Gerner for the electrode chip design.

2.7 Supporting Information Available

The Supporting Information includes chemicals and materials used, procedure for electrode chip fabrication, CV characterization of individual microband electrodes, CA responses and determination of current for use in applied current studies, assignments for electrode configurations in redox-MHD studies, schematics for the PDMS gasket placement with reference to the electrodes, horizontal flow profile and discussion for the 500-μm intraset gap, magnetic flux density distribution over regions where fluid flow was measured, a representative image processed by the PIV software and details of recording the videos and their timing, flow patterns at the end of the gap, dependence of velocity with location over active electrodes of increasing numbers, tables of average velocities across different gap widths and comparing velocities and magnetic fields at different locations in the gaps, and calculation of the Reynolds number. This material is available free of charge via the Internet at http://pubs.acs.org.

2.8 References

(1) Dutta, D.; Leighton, D. T. *Analytical Chemistry* **2003**, *75*, 57-70, DOI: 10.1021/ac020179r.

(2) Ajdari, A.; Bontoux, N.; Stone, H. A. *Analytical Chemistry* **2006**, *78*, 387-392, DOI: 10.1021/ac0508651.

(3) Chin, C. D.; Linder, V.; Sia, S. K. *Lab on a Chip* **2007**, *7*, 41-57, DOI: 10.1039/b611455e.

(4) Stone, H. A.; Stroock, A. D.; Ajdari, A. *Annual Review of Fluid Mechanics* **2004**, *36*, 381-411, DOI: 10.1146/annurev.fluid.36.050802.122124.

(5) Erickson, D.; Li, D. Q. *Analytica Chimica Acta* **2004**, *507*, 11-26, DOI: 10.1016/j.aca.2003.09.019.

(6) Ohno, K.; Tachikawa, K.; Manz, A. *Electrophoresis* **2008**, *29*, 4443-4453, DOI: 10.1002/elps.200800121.

(7) Foudeh, A. M.; Didar, T. F.; Veres, T.; Tabrizian, M. *Lab on a Chip* **2012**, *12*, 3249-3266, DOI: 10.1039/c2lc40630f.

(8) Roman, G. T.; Kennedy, R. T. *Journal of Chromatography A* **2007**, *1168*, 170-188, DOI: 10.1016/j.chroma.2007.06.010.

(9) Khandurina, J.; Guttman, A. *Journal of Chromatography A* **2002**, *943*, 159-183, DOI: 10.1016/s0021-9673(01)01451-0.

(10) Gardeniers, J. G. E.; van den Berg, A. *Analytical and Bioanalytical Chemistry* **2004**, *378*, 1700-1703, DOI: 10.1007/s00216-003-2435-7.

(11) Squires, T. M.; Quake, S. R. *Reviews of Modern Physics* **2005**, *77*, 977-1026, DOI: 10.1103/RevModPhys.77.977.

(12) Jacobson, S. C.; Hergenroder, R.; Koutny, L. B.; Ramsey, J. M. *Analytical Chemistry* **1994**, *66*, 2369-2373, DOI: 10.1021/ac00086a024.

(13) Rathore, A. S. *Electrophoresis* **2002**, *23*, 3827-3846, DOI: 10.1002/elps.200290004.

(14) Bazant, M. Z.; Ben, Y. X. *Lab on a Chip* **2006**, *6*, 1455-1461, DOI: 10.1039/b608092h.

(15) Anderson, E. C.; Weston, M. C.; Fritsch, I. *Analytical Chemistry* **2010**, *82*, 2643-2651, DOI: 10.1021/ac9020177.

(16) Weston, M. C.; Fritsch, I. *Sensors and Actuators B-Chemical* **2012**, *173*, 935-944, DOI: 10.1016/j.snb.2012.07.006.

(17) Grant, K. M.; Hemmert, J. W.; White, H. S. *Journal of the American Chemical Society* **2002**, *124*, 462-467, DOI: 10.1021/ja016544y.

(18) Leventis, N.; Gao, X. R. *Analytical Chemistry* **2001**, *73*, 3981-3992, DOI: 10.1021/ac010172u.

(19) Qian, S.; Bau, H. H. *Mechanics Research Communications* **2009**, *36*, 10-21, DOI: 10.1016/j.mechrescom.2008.06.013.

(20) Iverson, B. D.; Garimella, S. V. *Microfluidics and Nanofluidics* **2008**, *5*, 145-174, DOI: 10.1007/s10404-008-0266-8.

(21) Pamme, N. *Lab on a Chip* **2006**, *6*, 24-38, DOI: 10.1039/b513005k.

(22) Weston, M. C.; Gerner, M. D.; Fritsch, I. *Anal Chem* **2010**, *82*, 3411-8, DOI: 10.1021/ac901783n.

(23) Kang, H. J.; Choi, B. *Sensors and Actuators a-Physical* **2011**, *165*, 439-445, DOI: 10.1016/j.sna.2010.11.011.

(24) Weston, M. C.; Nash, C. K.; Fritsch, I. *Analytical Chemistry* **2010**, *82*, 7068-7072, DOI: 10.1021/ac101377a.

(25) Scrape, P. G.; Gerner, M. D.; Weston, M. C.; Fritsch, I. *Journal of the Electrochemical Society* **2013**, *160*, H338-H343.

(26) Arumugam, P. U.; Fakunle, E. S.; Anderson, E. C.; Evans, S. R.; King, K. G.; Aguilar, Z. P.; Carter, C. S.; Fritsch, I. *Journal of the Electrochemical Society* **2006**, *153*, E185-E194, DOI: 10.1149/1.2352040.

(27) Wagner, C. *Journal of the Electrochemical Society* **1951**, *98*, 116-128, DOI: 10.1149/1.2778113.

(28) Parrish, W. R.; Newman, J. *Journal of the Electrochemical Society* **1970**, *117*, 43-48, DOI: 10.1149/1.2407436.

(29) Fosset, B.; Amatore, C. A.; Bartelt, J. E.; Michael, A. C.; Wightman, R. M. *Analytical Chemistry* **1991**, *63*, 306-314, DOI: 10.1021/ac00004a003.

(30) Bard, A. J.; R., F. L., Electrochemical Methods: Fundamentals and Applications. Second Edition ed.; Wiley: New York, 1980.

(31) Gao, F.; Kreidermacher, A.; Fritsch, I.; Heyes, C. D. *Analytical Chemsitry* **2013**, *85*, 4414-4422.

2.S Supporting Information: Flat Flow Profiles Achieved With Microfluidics Generated by Redox-Magnetohydrodynamics (MHD)

The Supporting Information includes chemicals and materials used, procedure for electrode chip fabrication, cyclic voltammetric characterization of individual microband electrodes, chronoamperometry responses and determination of current for use in applied current studies, assignments for electrode configurations in 2.0 and 5.6 mm gap redox-MHD studies, schematics for the poly(dimethylsiloxane) gasket placement with reference to the electrodes, horizontal flow profile and discussion for the 500-μm intraset gap, magnetic flux density distribution over the regions where fluid flow was measured, a representative image processed by the particle image velocimetry software and details of recording the videos and their timing, flow patterns at the end of the gap, plots of dependence of velocity with location over active electrodes of increasing numbers, a table of average velocities across different gap widths, a table comparing velocities and magnetic fields at different locations in the gaps, and calculation of the Reynolds number for the device.

2.S1 Chemicals and Materials

All chemicals were reagent grade and used as received. Aqueous solutions were prepared using high purity deionized water (Ricca Chemical Company, Arlington, TX). Potassium chloride was purchased from EMD^{TM}, USA. Potassium ferricyanide ($K_3Fe(CN)_6$) and potassium ferrocyanide ($K_4Fe(CN)_6$) were obtained from EM Science, Gibbstown, NJ and J.T. Baker, Phillipsburg, NJ, respectively. Polystyrene latex microbeads (10 μm diameter, 2.5 % wt. dispersion in water) were purchased from Alfa Aeser, Wardhill, MA. The cylindrical, 0.5 in. thick × 1.0 in. diameter, 0.36 T NdFeB permanent magnet was obtained from Amazing Magnets, Irvine, CA. Silicon (100) wafers (125 mm diameter, 650 μm thickness, 2 μm thermally grown silicon dioxide) purchased from Silicon Quest International, Santa Clara, CA were used as the substrate material for the chips with patterned electrodes. Chromium and gold layers were deposited on the silicon wafers using chromium coated tungsten rods (Kurt J. Leskar Company, Clairton, PA) and small pieces of gold (Canadian Maple Leaf, 99.99 %) placed in a molybdenum boat (Kurt J. Leskar Company, Pittsburg, PA). Positive photoresist (AZ 4330) was used for the pattern transfer from photo plot masks (Advance Reproductions Corporation, North Andover, MA) to the wafer. Tetramethyl ammonium hydroxide (TMAH) solution was used as a developer in the photolithography process. Gold etchant (Transene, GE8148) and chromium etchant (HTA enterprise, CEP200) were used a received. Negative photoresist, benzocyclobutene, BCB (Cyclotene, 4024-40) was purchased from Dow Chemical Company. Sylgard 184 silicon elastomer base, Sylgard 184 silicon elastomer curing agent and OS-30 solvent (Ellsworth Adhesives, Milwaukee, WI) were used to form the poly(dimethyl siloxane), PDMS, gasket.[1] Pre-cleaned microscope glass slides (1.5 × 1.0 × 0.1 in.^{3}) were obtained from VWR.

2.S2 Electrode Chip Fabrication

The microfluidic chip was made using conventional microfabrication techniques with a procedure that was modified from earlier work performed in our laboratory.[1] Briefly, two different photo plot masks were designed using AutoCAD for pattern transfer of the gold microelectrode and BCB (insulator). In particular, the following steps were performed to fabricate the chips for redox-MHD studies. (a) RCA clean: wafers were cleaned using Radio Corporation of America (RCA) procedure. This involves an organic clean (using 5:1:1 mixture of DI H_2O:NH_4OH:H_2O_2 maintained at 75 °C) followed by an oxide stripping process (50:1 mixture of DI H_2O: HF at 27 °C) to remove ~50 nm of the silicon oxide. (b) Evaporation: the wafers were deposited with a 10.0 nm chromium adhesive layer using thermal vapor deposition (Edwards Auto 6 Evaporator) followed by another deposition of 100 nm gold layer, without breaking the vacuum seal between the depositions. (c) Photolithography step 1: the design from the mask for the gold layer was transferred to a positive photoresist layer, spin-coated (G3P-8 Spin-Coater) on the wafer. After soft baking the photoresist (90 °C for 2 min), the wafer was exposed to ultraviolet (UV) light (325 nm) for 19 s through the mask under a Karl SUSS Mictotec MA 150 aligner followed by developing the photoresist in a 2.5% tetramethylammonium hydroxide (TMAH) solution. (d) Wet etching: exposed metal regions on the wafer were selectively removed using gold and chromium etchants. The entire wafer was further exposed to UV radiation followed by another TMAH bath step to remove the remaining photoresist. (e) Photolithography step 2: BCB was used in this step to insulate leads and define the electrochemically active regions on the wafer. A 5.5 μm BCB layer was coated followed by a soft baking step at 80 °C for 90 s. The wafer was then exposed to UV light through the BCB layer mask. Unexposed/undesired BCB was removed by washing the wafer with DS2100, a BCB

remover, followed by a 4 h hard baking process under an N_2 environment. (f) Reactive ion etching: residual organic material on electrodes was removed using a "descum" procedure. The BCB-patterned wafer was placed in a reactive ion etching (RIE) chamber (Plasma Therm SLR 720) having a mixture of O_2 at 36 sccm, SF_6 at 4 sccm, at a pressure of 300 mtorr using radio frequency power of 300 W for 1 min. (g) Dicing: the processed wafer was cut into individual chips using a dicing saw (Micro Automation 1100). The resistance between adjacent band electrodes was beyond the measurement range of FLUKE 77 III multimeter (Fluke Corporation, WA, USA), confirming that the RCA clean did not remove sufficient oxide layer to short the electrodes via the underlying semiconductor substrate.

2.S3 Microband Electrode Characterization

The individual microband electrodes were characterized using cyclic voltammetry (CV) before they were used for the redox-MHD studies. Representative CV responses are provided in Figure 2.S1. They were obtained in the absence of a magnetic field and without microbeads in a static solution of 20 mL 0.1 M $K_3Fe(CN)_6$, 0.1 M $K_4Fe(CN)_6$, and 0.1 M KCl contained in a beaker, where the chip was positioned vertically, using a three-electrode setup with an off-chip Pt flag counter and Ag/AgCl (saturated KCl) reference electrodes. CV was performed by scanning from 0.6 V to -0.2 V at 0.05 V/s, and with 0.6 V as the initial potential held at a 2 s quiet time prior to the initial forward scan. A correlation with the expected behavior was found using calculated current from the Digisim (Bioanalytical Systems Inc., West Lafayette, IN) simulations, which confirmed the quality of the electrodes to be used for further studies. For a single electron transfer homogenous reaction, the average of the absolute values of the cathodic and anodic simulated peak currents was 539 µA ± 12 µA (over three cycles) using a double layer capacitance (C_{dl}) of 2.5×10^{-6} F and a planar electrode geometry. Other Digisim parameters were

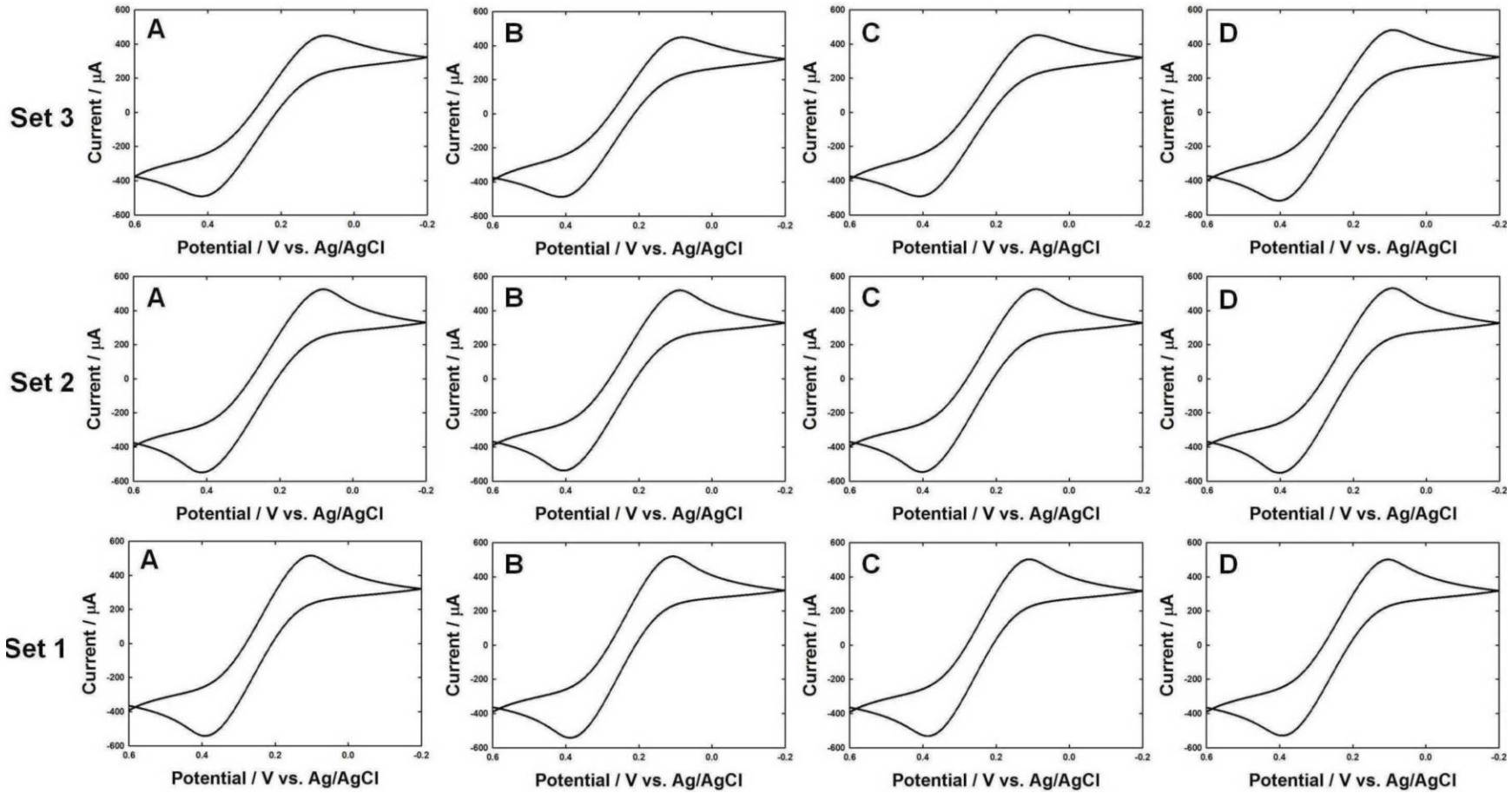

Figure 2.S1 Electrode characterization by cyclic voltammetry of individual microband electrodes was performed in the absence of a magnet, in a beaker containing 20 mL of a static solution of 0.1 M $K_3Fe(CN)_6$, 0.1 M $K_4Fe(CN)_6$, and 0.1 M KCl (without polystyrene microbeads), and using a three-electrode configuration, where each microband electrode served as the working electrode, a Pt flag as the counter electrode, and a Ag/AgCl (saturated KCl) as the reference electrode. The designations of the electrodes and sets are shown in Figure 2.S3.

the same as given for the experiments. The average of the absolute values of the experimental peak current was quite reproducible (RSD = 6%), 519 µA ± 31 µA for N = 24 (two peaks for each cycle of 12 electrodes), and was 3.7% less than the value based on the simulations. (Peak currents were measured from their maximum values to zero, instead of to the usual extension of the baseline prior to the peak. This is because the starting composition of the solution involved a non-standard 1:1 mole ratio of the two forms of the redox species, where faradaic current is present in all parts of the CV response, and the composition at the electrode will vary with starting potential, switching potential, and scan rate. However, because all experimental CV responses were under the same conditions and all peaks were measured in the same way, we feel that the comparison to the simulations is adequate for our purposes here.)

The peak splitting in the CV responses is 294 mV ± 18 mV, and for the Digisim simulations is 276.1 mV. This is much larger than the ~60 mV expected for a kinetically reversible redox couple, where n = 1. Because the high concentration leads to high current, the iR_u drop is substantial, even for these microelectrodes, where R_u is the uncompensated resistance. An uncompensated resistance of only 225 Ω is all that is needed to produce an iR_u drop of 117 mV (117 mV past the usual 30 mV from E°') in a linear sweep where the peak current is 519 µA (R_u = 0.117 V / 519 x 10^{-6} A = 225 Ω). The measured uncompensated resistance using the potentiostat's built-in function was 160 ± 10 Ω for pure electrolyte alone (0.1 M KCl), which is of a significant magnitude as that estimated from the large peak splitting. A two-point resistance measurement using an ohmmeter between a contact pad and a larger electrode on the chip gave a value of 126 Ω, which suggests that the majority of the resistance is most likely coming from the device and connections, rather than from the solution.

2.S4 Chronoamperometry (CA) and Selection of Applied Currents for the Redox-MHD Studies

MHD fluid flow can be induced either by directly applying a current or by applying a potential at selected electrodes in the presence of a magnetic field. Figure 2.S4 shows the schematic representation for the location of the poly(dimethylsiloxane) (PDMS) gasket with respect to the electrode positions. A solution containing 0.095 M $K_3Fe(CN)_6$, 0.095 M $K_4Fe(CN)_6$ in 0.095 M KCl containing polystyrene latex microbeads was poured onto the chip in the open region. A microscope slide was placed on top as a lid. Figure 2.S2 shows the current responses for the 2.0 mm interset electrode gaps when a potential step (+0.4 V) was applied (CA) for a two-electrode setup (using one, two, three, and four working-electrode configurations, Figure 2.S3a) in the presence of a magnet. At first, the current is high due to charging of the double layer and the faradaic transient current. The charging current is then expected to fall off exponentially, while the faradaic current decreases more gradually due to mass transfer limitations. There is some fluctuation in the current at times greater than 25 s, probably because of convection caused by density gradients.[2,3] Because the MHD force, and therefore the fluid flow depends linearly on current for this kind of cell, a changing current makes fluid flow analysis challenging.[4] Therefore, applied current (chronopotentiometry, CP) was used in the redox-MHD studies reported here to avoid the variations associated with CA. CP was performed with currents no greater than 70% of the mass transfer limited values at 100 s obtained by CA for each respective working-electrode configuration (120, 180, 246, and 307 μA, respectively). This time was chosen because it is the time needed to perform the longest MHD fluid flow study. Applied currents higher than the mass transfer limit damaged the anodes because of overoxidation. Thus, to err on the side of caution, the applied current was restricted to 70% of the mass transfer limited values.

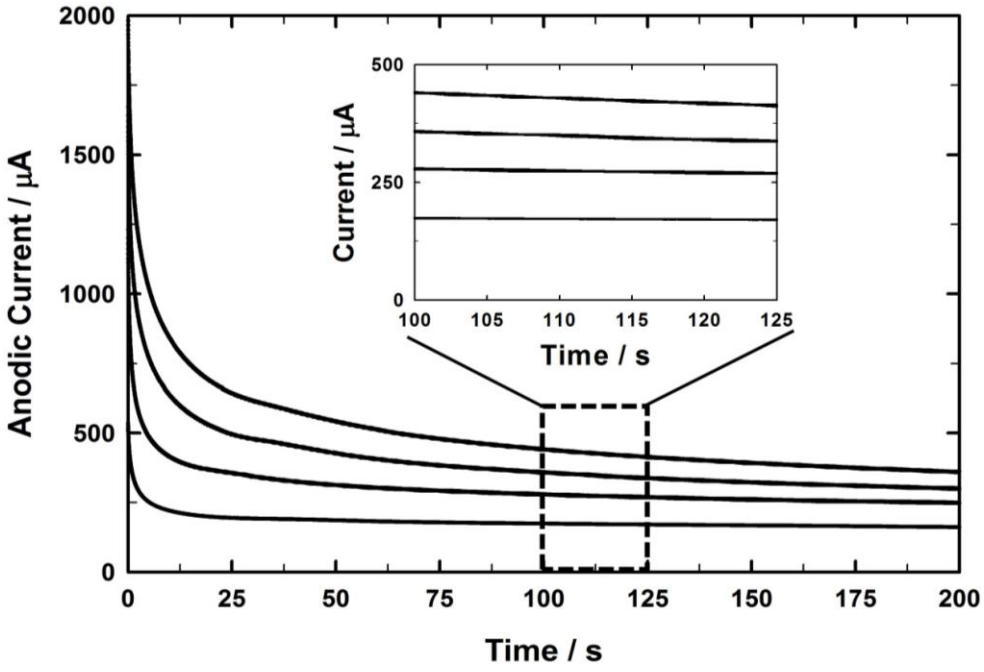

Figure 2.S2 Determination of maximum current for use in applied current experiments. Chronoamperometry was performed using a solution containing 0.095 M $K_3Fe(CN)_6$, 0.095 M $K_4Fe(CN)_6$), 0.095 M KCl, and polystyrene beads (2.5% wt dispersion in water) and in the presence of a 0.36 T magnetic field. The current for the one, two, three, and four electrode configurations (Figure 2.S3a), correspond to the CA responses having the lowest to highest current, respectively. Currents at 70% of the mass transfer limited values at 100 s were used for the applied current studies. The inset provides an expanded view for the data at times for which the 70% of the mass transfer limited current values were taken.

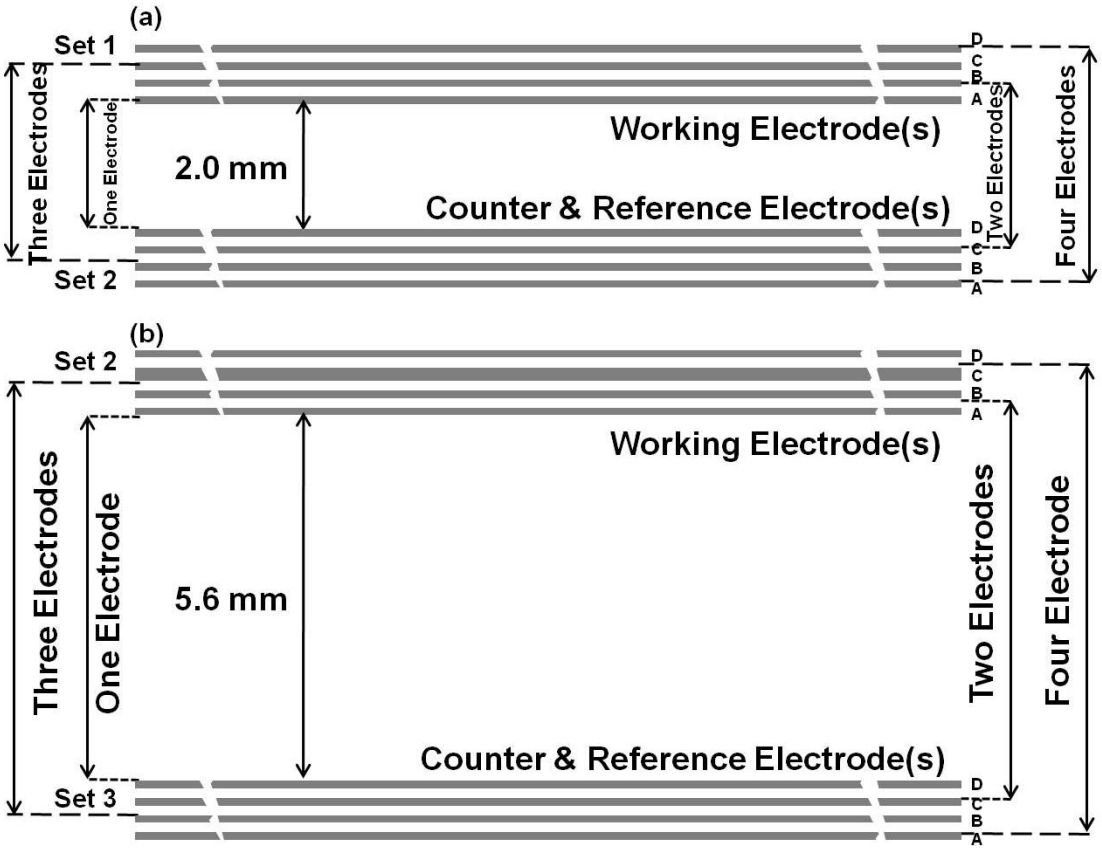

Figure 2.S3 Assignments of electrode configurations (1-electrode, 2-electrode, 3-electrode, and 4-electrode) and electrode sets (sets 1, 2, and 3) used in redox-MHD experiments for the **(a)** 2.0 mm and **(b)** 5.6 mm interset gaps. For experiments with the 2.0 mm interset gap the electrode(s) from set 1 were used as the working anode(s), and the corresponding electrode(s) in set 2 served as the combined counter/reference cathode(s). For experiments with the 5.6 mm interset gap the electrode(s) in set 2 were used as the working anode(s) and the corresponding electrode(s) in set 3 served as the combined counter/reference cathode(s).

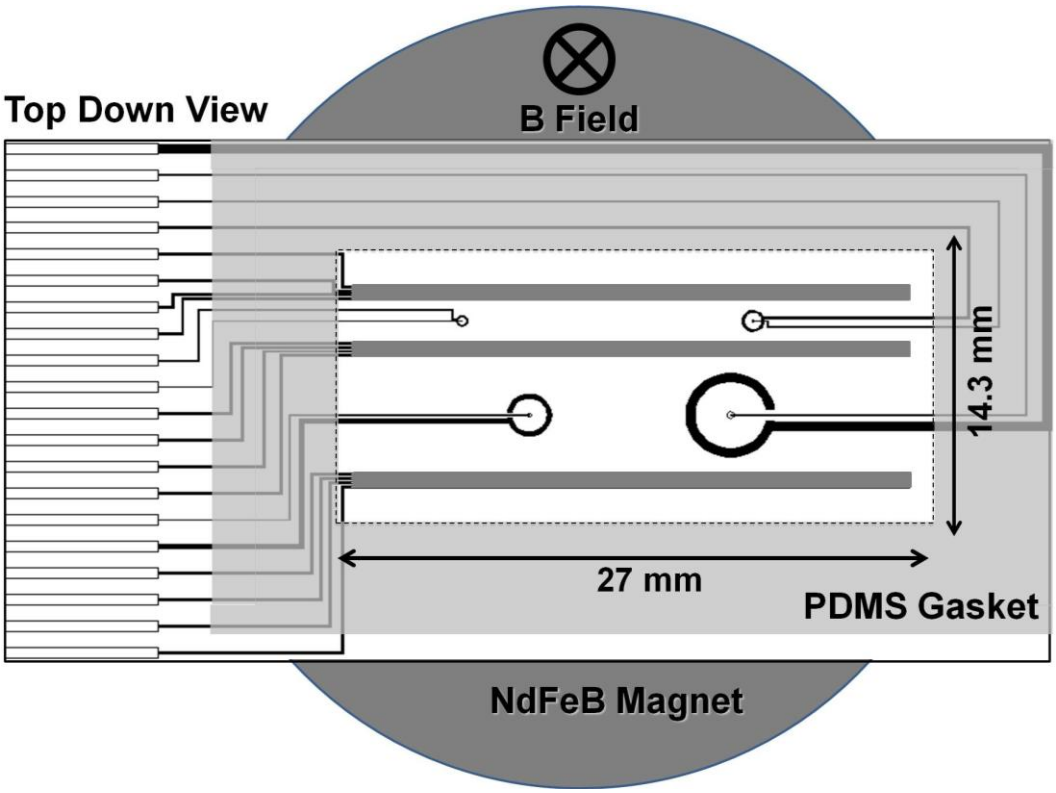

Figure 2.S4 Schematic shows the location of the PDMS gasket (light gray) relative to the electrode positions. The opening (14.3 mm wide × 27.0 mm long) is outlined by dashed lines, and the height (620.0 µm) is not shown in the figure. Microband electrodes are grouped in three sets of four electrodes each, where each set is represented by the dark gray rectangular regions. Black lines on the left side of those electrodes indicate the BCB-insulated leads. The redox species solution dispensed into the open region was contained by the PDMS sidewalls and a microscope slide placed on top (not shown). All the redox-MHD studies were performed inside the PDMS reservoir by application of a current or voltage at specific electrodes.

2.S5 Horizontal flow profile for the 500 µM intraset gap and One- electrode configuration for a fixed applied current

Figure 2.S5 shows a horizontal flow profile that was obtained across a much narrower (intraset) gap of 500.0 µm for a one-electrode configuration for the same fixed current (120 µA) and similar height (245 µm) as for the 2.0 mm and 5.6 mm studies. The profile is not parabolic and velocities are within a standard deviation of each other. There is an increase in average velocity from a gap of 500 µm (50.5 ± 6.5 µm/s) to one of 2.0 mm (63.6 ± 2.4 µm/s), but then a decrease with further widening of the gap to 5.6 µm (51.4 ± 2.2 µm/s) (Table 2.S1). The variation in magnetic field in these different locations is insufficient to explain the magnitude of this trend. The observed behavior is, however, compatible with the earlier findings for redox-MHD studies of widening gap but for electrodes <1/10th of the length,[1] and is consistent with the notion that shear forces slow the velocity between oppositely polarized electrodes for very narrow gaps, but as the gap increases further, the resistance to ion motion decreases, and therefore velocity increases. With additional separation, however, more ions from the ends contribute to the ionic current and therefore the ionic current density decreases, producing a slower flow.

2.S6 Reynolds Number

The redox-MHD fluid flows under the laminar flow conditions as calculated by the numerical values for Reynolds number, Re. The Reynolds number is the ratio of inertial to viscous forces and is determined by[5]

Table 2.S1 Average velocities across gaps under different conditions

Electrode Gap	Type of Experiment	Current (μA)	Electrode Configuration	Average velocity (μm/s)	Pooled Standard Deviation (μm/s)	Relative Standard Deviation (%)
500 μm Gap (Measurements Across Entire 500 μm)	One Current	120	1	50.5	6.5	12.8
2.0 mm Gap (Measurements Across Central 1.39 ± 0.06 mm)	Different Configurations, One Current	120	1	63.6	2.4	3.8
		120	2	63.1	1.9	3.1
		120	3	62.9	2.5	4.0
		120	4	60.5	2.0	3.3
5.6 mm Gap (Measurements Across Central 4.61 ± 0.06 mm)	Different Configurations, One Current	120	1	51.4	2.2	4.3
		120	2	49.2	2.5	5.1
		120	3	47.5	2.4	5.1
		120	4	46.1	1.9	4.2
	One Configuration, Different Currents	118	4	40.9	1.8	4.4
		180	4	64.4	2.3	3.5
		246	4	89.3	2.9	3.2
		307	4	110.0	3.8	3.5
	Different Configurations, Different Currents	118	1	52.8	6.3	11.9
		180	2	74.3	8.7	11.6
		246	3	94.2	11.8	12.5
		307	4	114.6	13.2	11.5

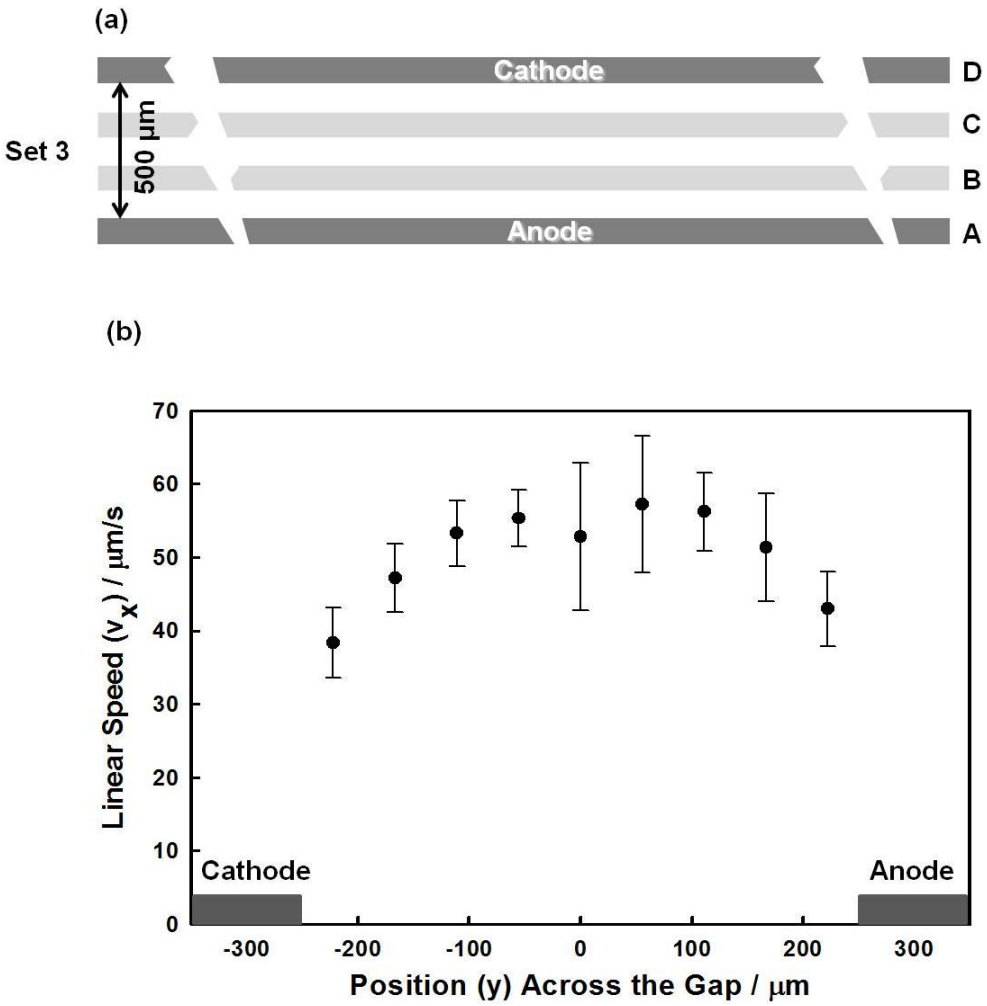

Figure 2.S5 Horizontal flow profile for the intraset electrode configuration for a fixed applied current (120 µA). The velocity (v_x) was measured as a function of position in y at a constant z plane (245.0 µm above the chip surface) across the intraset electrode gap of 500.0 µm within electrode set 3 where microband A served the working electrode (anode) and D served as the combined counter/reference (cathode).

$$Re = \frac{\rho v l}{\mu} \quad \text{(Eq. 2.S1)}$$

Here, ρ is the solution density, v the mean fluid flow velocity, l the hydraulic diameter given by 4 × cross sectional area / wetted perimeter (which equals 2 × separation between the plates),[6,7] and μ is the dynamic viscosity. The value for the Reynolds number under the redox-MHD conditions is 0.19 (where ρ = 1045.39 kg/m^3, v = 125 µm/s, l = 2 × PDMS cell height (620 µm) = 1.24 × 10^{-3} m, μ = 8.4849 × 10^{-4} kg/m.s), which is less than unity and hence suggests that the solution in the device is under laminar flow conditions.

2.S7 Magnetic Flux Density Distribution

The magnetic flux density was measured experimentally at different locations on the NdFeB permanent magnet using a dc magnetometer (Alfalab Inc.), and its magnitude was 0.356 T ± 11.4 mT. Simulations were also performed, using AMPERES (3D Magnetic V.6.4, Integrated Engineering Software, Winnipeg, Manitoba, Canada), and include all the regions for which fluid velocity is reported in the main document. Briefly, a material corresponding to NdFeB permanent magnet was assigned to the AMPERES followed by an autocad drawing providing the dimensions of the 38.1 mm × 12.7 mm cylindrical magnet. To-scale projection of the inter electrode sets (floating lines in the solution in Figure 2.S6) was also drawn at a constant z = 0.26 mm. It is assumed that the electrode materials, substrate, lid, and PDMS do not interfere with the magnetic flux density distributions. The side view of the simulated magnetic field superimposed over the magnet, and hand drawn electrode chip, PDMS gasket, and the glass lid are given in Figure 2.S6.

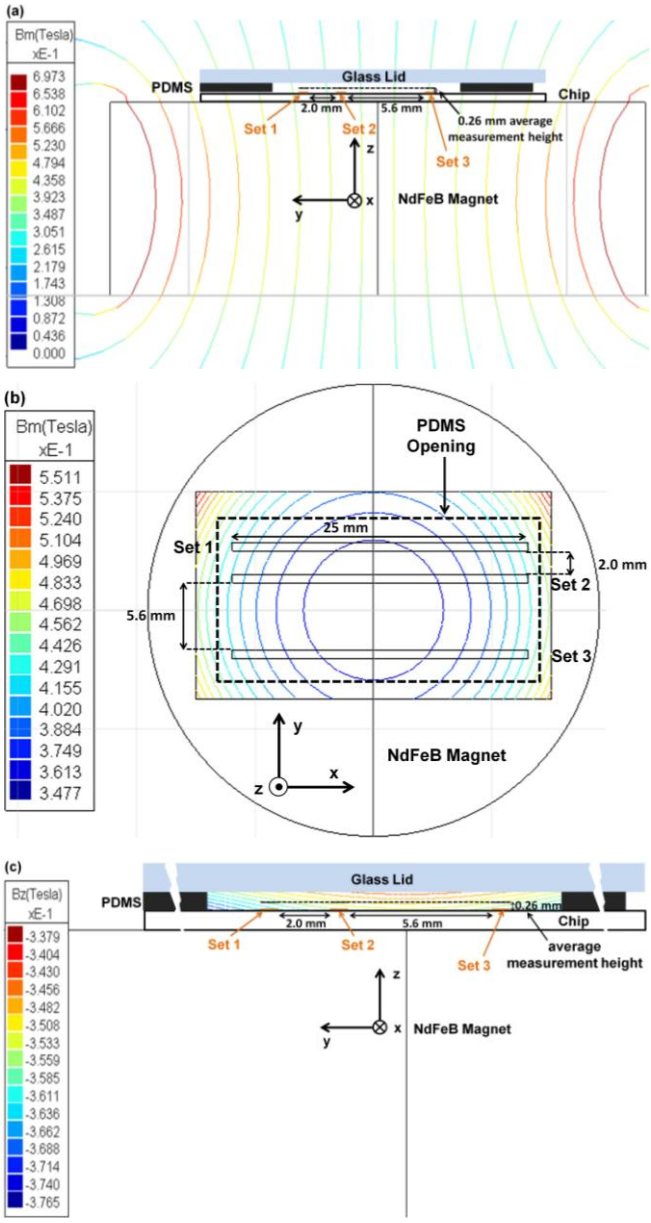

Figure 2.S6 Distribution of the magnetic flux density. (a) Front view of the magnetic field lines simulation in the y-z plane shows a strong field at the edges whereas it decreases going toward the center. (b) Magnetic field distribution for the x-y plane at a constant z (0.26 mm above the chip surface). For both the interset gaps, the field density changes significantly from the center toward each end. (c) Magnetic field contours for Bz above the chip surface, and within the electrochemical cell. The variation in magnetic flux density across the interset electrode gap is fairly uniform, however it decreases going toward the glass lid. Floating lines in the solution represent projection of electrode set (1, 2, and 3) from the chip surface. Dotted line in the figure denotes the approximate average height at which the velocity measurement was performed. The orange colored electrode sets designed on the chip surface are not to scale. Together the dotted line or the colored electrode sets did not interfere with the magnetic field simulations.

Table 2.S2 Percent change in velocities (V) and magnetic fields (B) between a location near the anode [position 1, (436.89 ± 27.64) µm to (545.26 ± 34.29) µm] a location in the center of the gap [position 2, (54 ± 11.31) µm to (-54.2 ± 11.31) µm], and a location near the cathode [position 3, (-436.89 ± 27.64) µm to (-545.26 ± 34.29) µm]. These experiments involved 120 µA current.

		Percent Change in Velocities			Percent Change in Magnetic Fields		
Electrode Gap	Electrode Configuration	Between V2 and V1	Between V3 and V2	Between V3 and V1	Between B2 and B1	Between B3 and B2	Between B3 and B1
2.0 mm Gap	1	1.96	1.98	3.94	0.48	0.25	0.73
	2	-1.59	3.90	2.61			
	3	2.05	3.52	5.58			
	4	-1.94	2.48	0.55			
5.6 mm Gap	1	-10.80	3.04	-7.76	0.14	-0.63	-0.48
	2	-4.49	-1.57	-6.06			
	3	-4.76	-7.58	-12.33			
	4	3.06	-3.58	-0.52			

Figure 2.S6a shows the magnetic field distribution as the streamlines, and depicts the fairly uniform pattern in y direction across the interset electrode gap for a constant height, but a significant change in the upward z direction (43.6 mT) was observed. Figure 2.S6b shows the magnetic field distribution in the x-y plane at a constant z (0.26 mm). For both the interset gaps, the field density changes significantly from the center toward each end. For the 2.0 mm interset electrode gap, the magnetic field changes by 54.3 mT in positive x direction, and 81.4 mT in the negative x direction. For the 5.6 mm interset electrode gap the change in magnetic field was observed to be 54.3 mT and 67.8 mT in the positive and negative x direction, respectively. Figure 2.S6c depicts the variation in z component of magnetic field, B_z. As observed, for the 5.6 mm gap, overall, the B_z decreases by 2.2 mT from cathode (0.3533 T) to anode (0.3511 T) across the interset gap for the one-electrode configuration, and at 0.26 mm height. However starting from the center, the B_z increases by 0.8 mT toward anode (0.3503 T to 0.3511 T), and it increases by 3 mT (0.3503 T to 0.3533 T) toward the cathode (See Figure 2.S6c). For the 2.0 mm gap, at z = 0.26 mm, B_z increases by 4.1 mT from cathode (0.3523 T) to anode (0.3564 T) for the one-electrode configuration. The magnetic field intensity decreases and increases by 1.9 mT (0.3542 T to 0.3523 T) and 2.2 mT (0.3542 T to 0.3564 T) from the center toward cathode and anode, respectively. In the upward z direction, and at the center of the 5.6 mm interset gap, the B_z decreases by 9 mT from the chip surface (0.3538 T) toward the glass lid (0.3448 T). Overall, a small drop in B_z (the main component contributing toward MHD force), indicates the magnetic field uniformity across the interset electrode gap for a fixed height, and hence the fluid flow profile predominantly depends upon the ionic current density.

2.S8 Particle image Velocimetry (PIV)

Figure 2.S7 shows an example of PIV processed results for a small region over which fluid flow was measured for the 5.6 mm gap having the one-electrode configuration, and at a height of 280 μm for an applied current of 120 μA. The uniform velocity magnitude and direction shows a flat flow profile over this region. From a PIV image, like the one in the Figure, an average of the magnitude of 14 velocity vectors in a single column gives one data point at a fixed location in the corresponding plots (Figures 2.3, 2.4, and 2.5) in the main document. The error bars for each point in those plots equal plus/minus one standard deviation of the magnitude of the 14 vectors at the fixed location. As the horizontal field of view of the microscope was smaller than the interset gap region, four to five videos were recorded by incrementally adjusting the position of the stage sequentially within the same experiment or separately in different experiments to cover the whole gap, but at same height from the chip and distance from the electrode ends. The times chosen for velocity analysis at each position are long enough to ensure that convection caused by manipulating the stage to reposition the chip had dampened out.

2.S9 Flow Patterns and Profile at the end of a gap

Figure 2.S8 shows that the linear flow path of the fluid can be sustained along the 2.5 cm path of the 2.0 mm gap for the one-electrode configuration, until near the end of the active electrodes (around 700 μm from the end) where it starts to turn around (Figure 2.S8b). Amazingly, the horizontal flow profile before 700 μm from the end is also relatively flat (104.4 ± 9.5 μm/s across the entire P2 region), but where the fluid flow drops about 30% across the central 1 mm of the gap from the innermost line of vectors in the P1 region to the innermost line of vectors of the P3 region. (All of the vectors in the P2 region are plotted in Figure 2.S8c. However, only a single line of vectors, the red/orange ones, were used from the P1 and P3

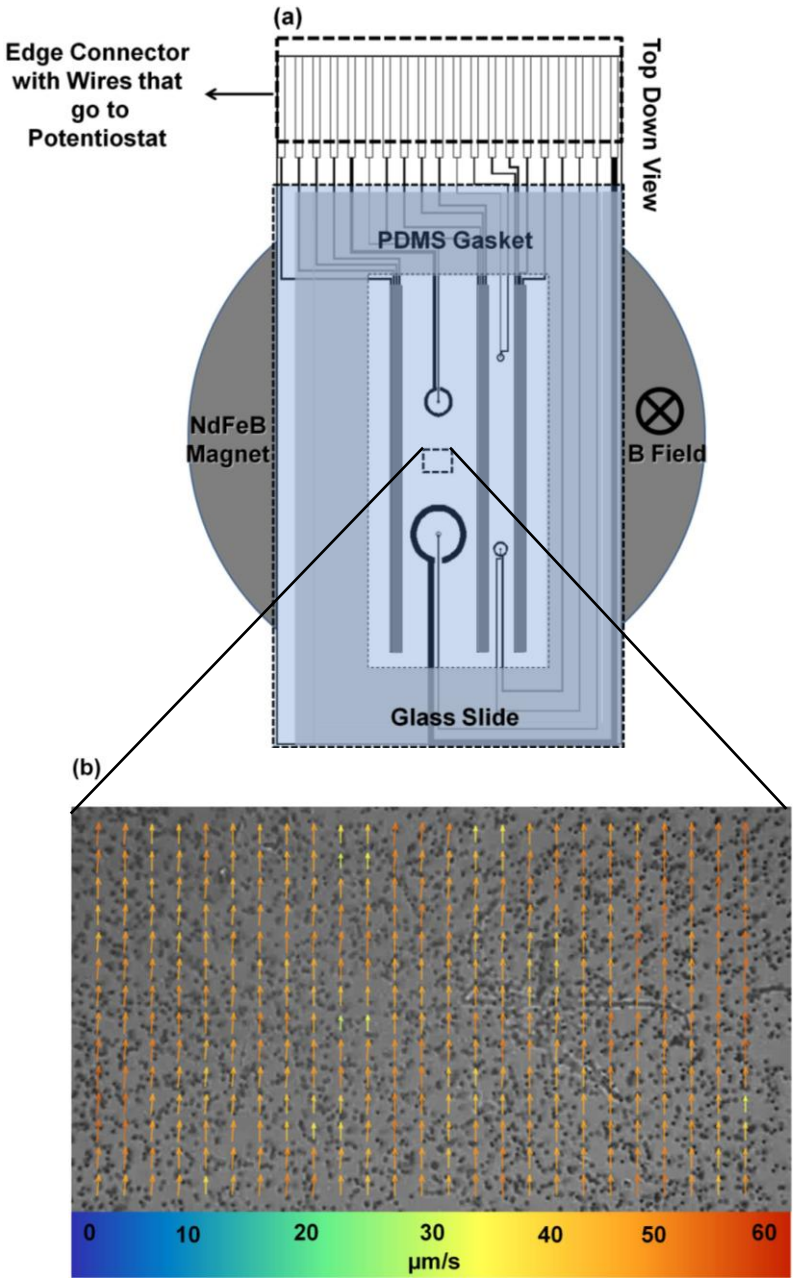

Figure 2.S7 Particle image velocimetry (PIV) processed results. The recorded microbead movement in a solution containing 0.095 M $K_3Fe(CN)_6$, 0.095 M $K_4Fe(CN)_6$), 0.095 M KCl, and polystyrene beads (2.5 % wt dispersion in water), and in the presence of a 0.36 T magnetic field, was analyzed using PIV software. (a) Figure shows top-down view of the set-up, and depicts the small region over which the PIV image is presented. (b) The representative image shown here is for a small region in the 5.6 mm interset electrode gap. The direction and magnitude of the microbead velocity indicate the uniformity of fluid flow within the interset electrode gap.

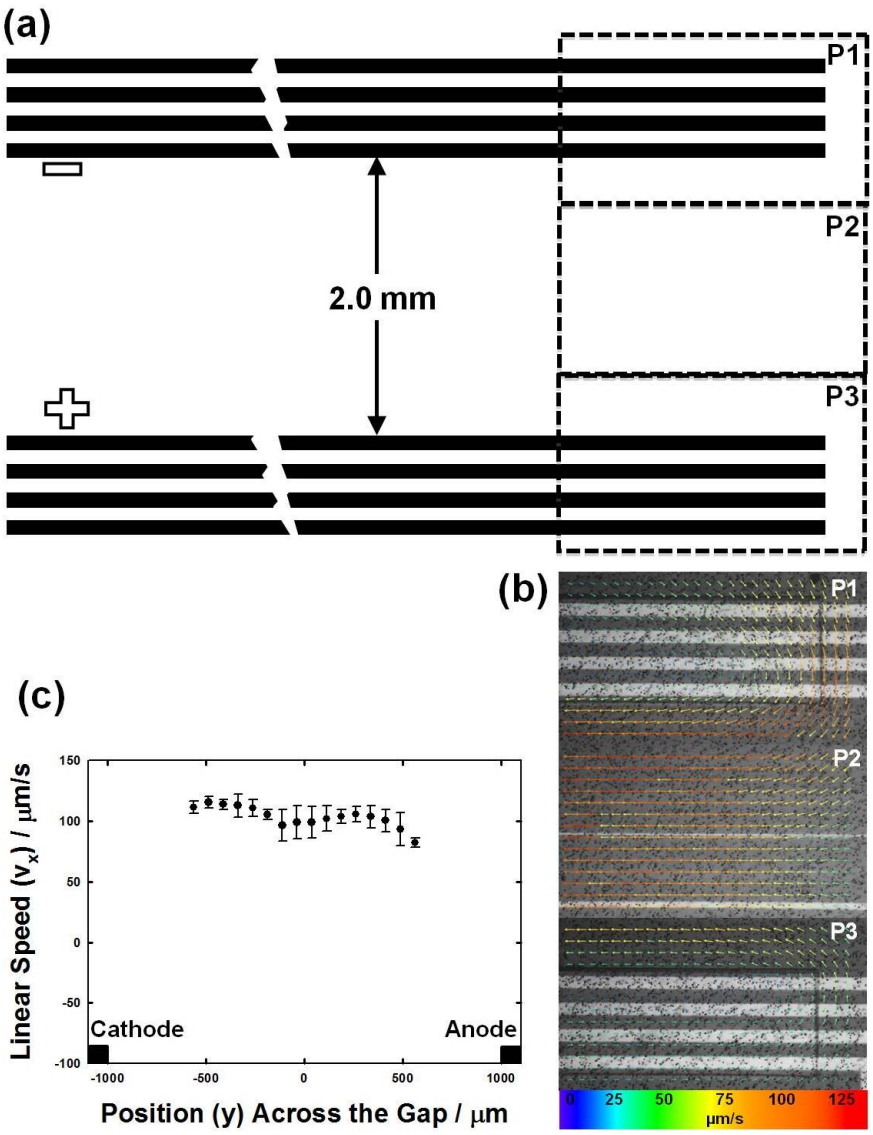

Figure 2.S8 Flow patterns and velocities attained by redox-MHD at the end of a 2.0 mm interset gap, using the one-electrode configuration, in a 620-µm high cell, and in a solution containing 0.095 M $K_3Fe(CN)_6$, 0.095 M $K_4Fe(CN)_6$), 0.095 M KCl, and polystyrene beads (2.5 % wt dispersion in water), and in the presence of a 0.36 T magnetic field. An applied potential of +0.4 V between the anode (working electrode) and cathode (combined counter/reference electrode) was used instead of an applied current, resulting in a time-dependent velocity because the current changes with time. Regions P1, P2, and P3 were recorded at 272 µm height above the chip in sequence during the experiment, where the average anodic current was 195.5 ± 0.7 µA, 176.8 ± 0.4 µA, and 166.5 ± 0.4 µA, during the times when velocities were taken for each region respectively. (a) Schematic shows the relative positions of the electrodes, gap, and recorded regions (P1, P2, and P3). (b) Velocity vectors attained by PIV analysis from videos of the beads in the three regions. (c) Horizontal flow profile of raw velocity data, taking the innermost vector lines in the P1 and P3 regions and all the vector lines in region P2.

regions in the plot, which are outside the diffusion layers at the electrodes. The other lines of vectors in P1 and P3 that were not used for this plot are inside the diffusion layer and near the turn-around point of the fluid flow.) These data were obtained using an applied potential. Thus, the current dropped during the experiment and sequentially from region P1 to P3, in the order of recording bead movement. It has been shown that the fluid speed is proportional to current in redox MHD.[4] Thus, normalizing the velocities to the current during the times of the experiment when the velocities were recorded for each region compensates for this change, and yields an average speed/current in the P1 region of 0.57 ± 0.02 μm s^{-1} μA^{-1} and in the P2 region of 0.59 ± 05 μm s^{-1} μA^{-1}, which are within a standard deviation of each other. There still remains a drop between the P1 and P3 regions, but it is only 15% (from 0.57 ± 0.02 μm/ s^{-1} μA^{-1} in P1 to 0.49 ± 0.02 μm s^{-1} μA^{-1} in P3). This experiment also further emphasizes the need to perform redox MHD studies with controlled current when the most reliable and quantitative results are desired.

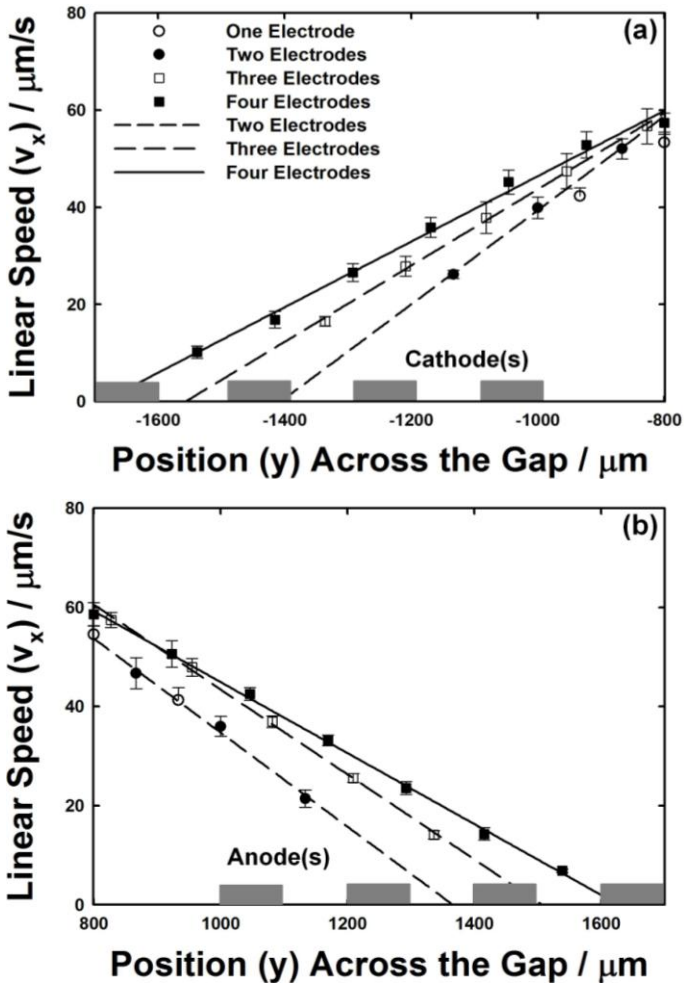

Figure 2.S9 Dependence of velocity over (a) the cathodes and (b) the anodes for the 2.0 mm gap and for which the current is constant at 120 μA and the number of active electrodes is increased from one to four. The plots of raw data are expanded views of the electrode regions from Figure 3a in the main document. The lines correspond to the least squares best fit to the raw data for each electrode configuration. Because there are only two data points in this region for the one-electrode configuration, a best fit line was not obtained for them. Equations for the lines over the cathodes in (a) are: $y = (0.0969 \pm 0.0032)\ x + (136.3 \pm 3.2)$, $R^2 = 0.9989$, x-intercept = -1406 ± 57 μm for the two-electrode configuration, $y = (0.0785 \pm 0.0018)\ x + (122.2 \pm 2.0)$, $R^2 = 0.9984$, x-intercept = -1557 ± 44 μm for the three-electrode configuration; and $y = (0.0674 \pm 0.0026)\ x + (113.8 \pm 3.1)$, $R^2 = 0.9926$, x-intercept = -1689 ± 80 μm for the four-electrode configuration. Equations for the lines over the anodes in (b) are $y = (-0.0949 \pm 0.0083)\ x + (129.6 \pm 8.3)$, $R^2 = 0.9925$, x-intercept = 1366 ± 148 μm, for the two-electrode configuration; $y = (-0.0857 \pm 0.0017)\ x + (129.1 \pm 1.9)$, $R^2 = 0.9988$, x-intercept = 1506 ± 38 μm for the three-electrode configuration; and $y = (-0.0716 \pm 0.0011)\ x + (116.5 \pm 1.3)$, $R^2 = 0.9988$, x-intercept = 1627 ± 31 μm for the four-electrode configuration. The units of the slopes are in μm/s / μm or s^{-1}; the units of the y-intercepts are μm/s.

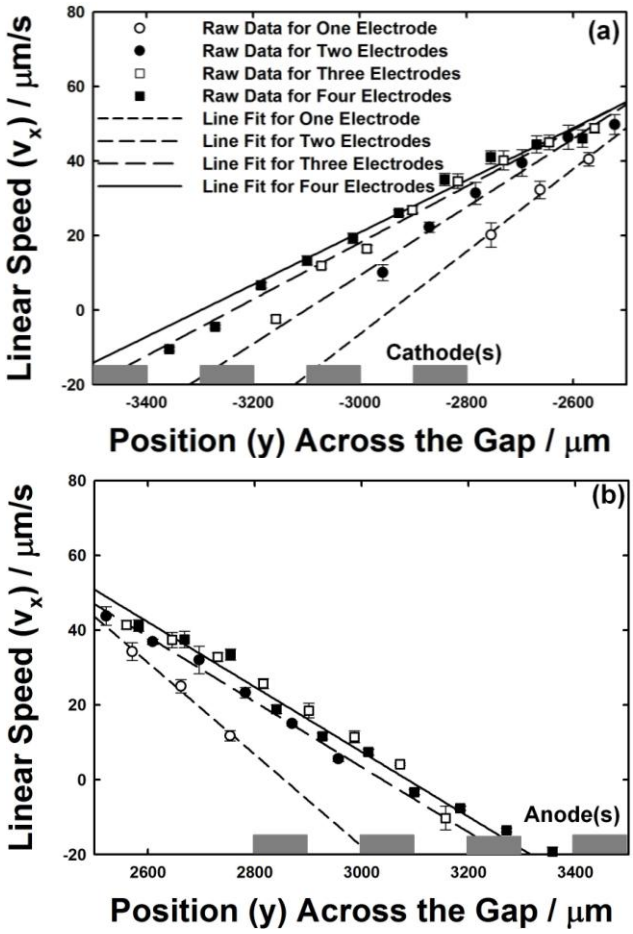

Figure 2.S10 Dependence of velocity over (a) the cathodes and (b) the anodes for the 5.6 mm gap and for which the current is constant at 120 μA and the number of active electrodes is increased from one to four. The plots of raw data are expanded views of the electrode regions from Figure 3b in the main document. The lines correspond to the least squares best fit to the raw data for each electrode configuration. Equations for the lines over the cathodes in (a) are: y = (0.1108 ± 0.0121) x + (325.9 ± 32), R^2 =0.9883, x-intercept = -2942 ± 432 μm, for the one-electrode configuration; y = (0.0917 ± 0.0080) x + (284.5 ± 21.9), R^2 = 0.9706, x-intercept = -3101 ± 361 μm, for the two-electrode configuration; y = (0.0758 ± 0.0050) x + (245.3 ± 14.1), R^2=0.9788, x-intercept = -3238 ± 283 μm, for the three-electrode configuration; and y = (0.0700 ± 0.0044) x + (230.8 ± 12.8), R^2=0.9764, x-intercept = -3298 ± 278 μm, for the four-electrode configuration. Equations for the lines over the anodes in (b) are: y = (-0.1228 ± 0.0125) x + (350.6 ± 33.4), R^2=0.9897, x-intercept = 2855 ± 399 μm, for the one-electrode configuration; y = (-0.0871 ± 0.0043) x + (264.8 ± 12), R^2= 0.9903, x-intercept = 3039 ± 203 μm, for the two-electrode configuration; y = (-0.0746 ± 0.0034) x + (234.6 ± 9.6), R^2=0.9898, x-intercept = 3144 ± 192 μm, for the three-electrode configuration; and y = (-0.0868 ± 0.0090) x + (267.8 ± 25), R^2=0.9586, x-intercept = 3086 ± 433 μm, for the four-electrode configuration. The units of the slopes are in μm/s / μm or s^{-1}; the units of the y-intercepts are μm/s.

2.S10 References

(1) Anderson, E. C.; Weston, M. C.; Fritsch, I. *Analytical Chemistry* **2010**, *82*. 2643-2651.

(2) Bard, A. J.; R., F. L. *Electrochemical Methods: Fundamentals and Applications*, Second Edition ed.; Wiley: New York, 1980.

(3) Volgin, V. M.; Davydov, A. D. *Russian Journal of Electrochemistry* **2006**, *42*. 567-608.

(4) Weston, M. C.; Fritsch, I. *Sensors and Actuators B-Chemical* **2012**, *173*. 935-944.

(5) Squires, T. M.; Quake, S. R. *Reviews of Modern Physics* **2005**, *77*. 977-1026.

(6) Munson, B. R.; Young, D. F.; Okiishi, T. H. *Fundamentals of Fluid Mechanics*, 5th ed.; John Wiley & Sons, 2006.

(7) Nguyen, N. T.; Wereley, S. T. *Fundamentals and Applications of Microfluidics*, 2nd ed.; Artech House, Inc. , 2006.

Appendix: Permission to Print the Submitted Article

EIC Office

On Tue, Oct 8, 2013 at 7:55 AM, EIC Office <eic@anchem.acs.org> wrote:

Dear Vishal Sahore:

You have my permission to use this article "***Flat Flow Profiles Achieved with Microfluidics Generated by Redox-Magnetohydrodynamics (MHD)***" in your thesis as long as the correct citations are made as directed in the ACS Thesis/Dissertation Policy and the ACS Journal Publishing Agreement.

Sincerely,

Prof. Jonathan V. Sweedler
Editor-in-Chief
Analytical Chemistry
Phone: 217-244-7359
Fax: 202-513-8699
Email: eic@anchem.acs.org

3. Microfluidic Rotational Flow Generated by Redox-Magnetohydrodynamics (MHD)

Following chapter was written in a format to be submitted as a manuscript in the Microfluidics and Nanofluidics journal. After establishing the flat flow profile, work in this chapter explores another microfluidic feature of fluid circulation induced by redox-magnetohydrodynamics (MHD) pumping. This feature is important step toward the integration of multiple chemical processes on a single lab-on-a-chip device.

3.1 Abstract

Microfluidic rotational flow (Reynolds number < 1) with velocity magnitude ≤ 14 μm/s was achieved in a small volume (14.3 mm wide × 27.0 mm long × 620.0 μm high) contained over a chip, by the redox-magnetohydrodynamics (MHD) pumping. Chip consists of an insulated silicon substrate that was fabricated with different sets of concentric disk-ring gold microelectrodes. MHD force ($\mathbf{F_B} = \mathbf{j} \times \mathbf{B}$) required for the fluid flow was generated by the ionic current density, **j**, due to the electrochemistry of 0.095 M $K_3Fe(CN)_6$, 0.095 M $K_4Fe(CN)_6$ in 0.095 M KCl solution, and the external magnetic field, **B,** with a 0.36 T NdFeB permanent magnet located beneath the chip. Fluid flow was monitored between the concentric disk (radius: 80 μm) - ring (inner radius: 800 μm) microelectrodes region, by tracking 10 μm size polystyrene latex beads mixed with the redox species solution, using video microscopy. Data analysis was performed by the particle image velocimetry (PIV) software. In a different study, the effects of redox-MHD circulation, on an externally added red dye sample to the 0.3 M $K_3Fe(CN)_6$, 0.3 M $K_4Fe(CN)_6$ in 0.1 M KCl solution, were also recorded using disk (radius: 160 μm) and ring (inner radius: 1600 μm) microelectrodes.

3.2 Introduction

Microfluidic rotational flow between concentric disk-ring microelectrodes was obtained under laminar conditions (Reynolds number < 1), using a relatively new pumping method of redox-magnetohydrodynamics (MHD). Localized fluid circulation in a small volume contained over the silicon chip was generated when a constant potential was applied across the electrodes in the presence of an external magnetic field. Fluid rotation due to radial non-uniformity in flow velocity is important to enhance the interaction between different reagents (e.g. antigen–antibody or single strands of DNA), and therefore is advantageous for lab-on-a-chip applications such as immunoassays and DNA hybridization assays.

Lab-on-a-chip technology is promising for miniaturizing chemical, biological, and environmental analysis on a single hand held chip.[1,2] Microfluidics plays an important role toward this miniaturization by controlling the movement of tiny fluid volumes over the chip.[3,4,5] For a typical lab-on-a-chip application such as an immunoassay, the interaction between antigen and antibody is important and is limited by the species mass transport, which could affect the analysis time as well as device sensitivity.[6] However, well designed localized convection in the on-chip microfluidic environment can possibly increase the mass transport as well as the rate of interactions. Microfluidic stirring and mixing are two possibilities, and have been tried before using active methods like electro-thermal, induced charge electro-osmosis, and the liquid on liquid techniques.[7,8,9,10] Most of the approaches either require a complex device design involving flow channels, or need a high voltage, which further complicate device fabrication and its operation.[11,12] In the present work, a relatively easy–to-use fluid pumping technique of redox-MHD is demonstrated that induces a localized fluid circulation. MHD works in the presence of ionic current density and magnetic field together, and is described by the magnetic part of

Lorentz force equation ($\mathbf{F_B = j \times B}$), with its direction given by the right hand rule. Here **j** is the ionic current density of a fluid element (C/m^2), **B** (Tesla) is the magnetic flux density, and $\mathbf{F_B}$ (N/m^3) is the MHD body force acting on the fluid element. MHD offers the benefits of generating a wide range of velocities, choosing various parameters to program flow, and compatibility with aqueous as well as non-aqueous solutions.[13] But in the absence of easily oxidizable or reducible chemical species, MHD needs the application of a high voltage as well, which creates the problems associated with electrode corrosion and bubble generation.[12,14,15] An alternative is to generate ionic current by introducing the redox species that can sustain a faradaic current at a lower overpotential, and is called "redox-MHD", and thus avoiding the problems commonly encountered with the traditional MHD pumps in supporting electrolyte.[16,17,18]

In this study, the redox-MHD guided microfluidic rotation, without channels, was generated under different experimental conditions. A chip containing multiple sets of concentric disk-ring gold microelectrodes was fabricated using an insulated silicon substrate. MHD body force was generated by the ionic current density (**j**), and an external magnetic field (**B**), created by the electrochemistry of potassium ferricyanide, potassium ferrocyanide in the potassium chloride electrolyte solution, and NdFeB permanent magnet, respectively (Figure 3.1). Electrochemical reactions were initiated by applying a constant potential at the selective disk-ring microelectrodes immersed in the redox-species solution contained over chip by the sidewalls of a poly (dimethyl) siloxane, PDMS, gasket. Fluid circulation was monitored by tracking the movement of polystyrene latex beads and a red dye sample in the solution, using video microscopy.

3.3 Experimental Section

3.3.1 Chemicals and Materials

All chemicals were reagent grade and used as received. Aqueous solutions were prepared using high purity deionized water purchased from Ricca Chemical Company, Arlington, TX. Potassium chloride was purchased from EMD^{TM}, USA. Potassium ferricyanide ($K_3Fe(CN)_6$) and potassium ferrocyanide ($K_4Fe(CN)_6$) were purchased from EM Science, Gibbstown, NJ and J.T. Baker, Phillipsburg, NJ, respectively. Polystyrene latex microbeads (10 µm diameter, 2.5% wt. dispersion in water) were obtained from Alfa Aeser, Wardhill, MA. A 0.5 in. thick × 1.0 in. diameter 0.36 T NdFeB permanent magnet was purchased from Amazing Magnets, Irvine, CA. Silicon (100) wafers (125 mm diameter, 650 µm thickness, 2 µm thermally grown silicon dioxide) were purchased from Silicon Quest International, Santa Clara, CA, and used as the insulated substrate material to fabricate the electrode chips. Chromium as an adhesion layer, and gold as an electrode layer, was deposited on the silicon wafers using chromium coated tungsten rods (Kurt J. Leskar Company, Clairton, PA), and the small pieces of gold (Canadian Maple Leaf, 99.99%) placed in a molybdenum boat (Kurt J. Leskar Company, Pittsburg, PA), respectively. Positive photoresist (AZ 4330) was used for the gold electrode pattern transfer from photo plot masks (Advance Reproductions Corporation, North Andover, MA) to the silicon wafer. Tetramethyl ammonium hydroxide (TMAH) solution was used as a developer in the photolithography process to remove the unwanted photoresist. Gold etchant (Transene, GE8148) and chromium etchant (HTA enterprise, CEP200) were used a received in the wet etching process. Negative photoresist, benzocyclobutene, BCB (Cyclotene 4024-40) was purchased from the Dow Chemical Company, and was used to insulate the undesired gold leads on the wafer. Sylgard184 silicon elastomer base, Sylgard 184 silicon elastomer curing agent, and the OS-30

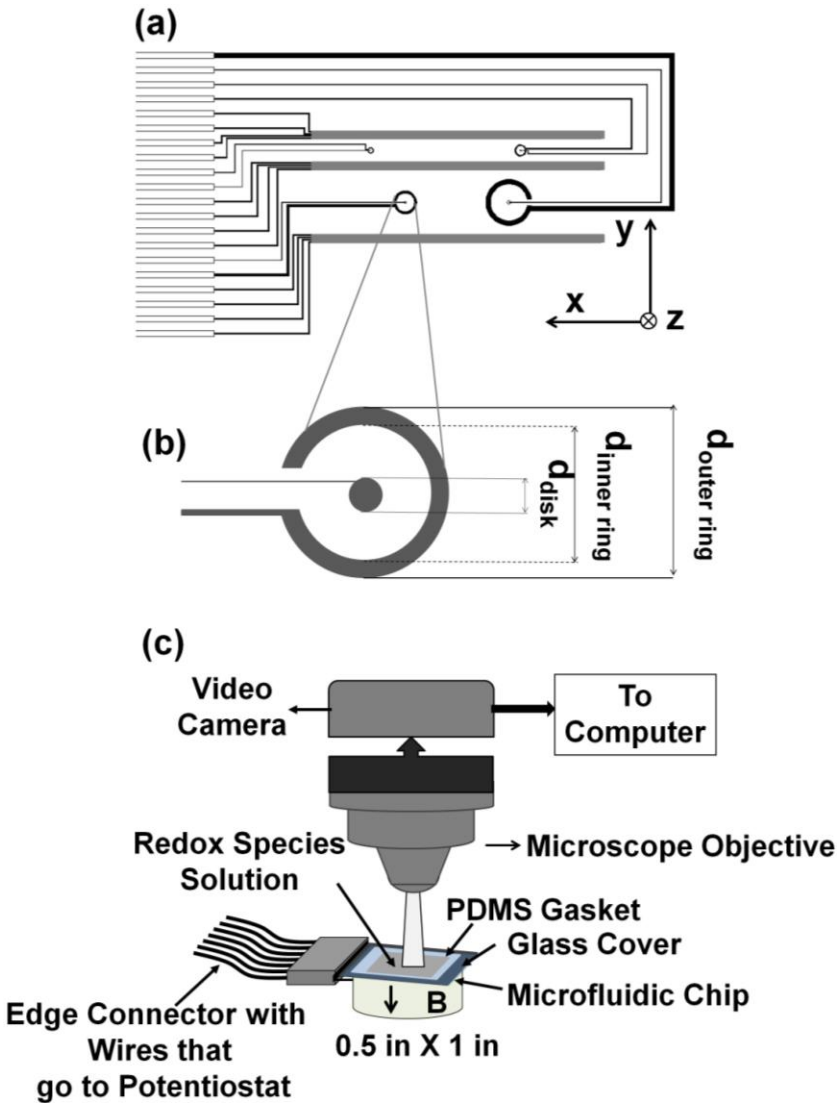

Figure 3.1 (a) Top-down view of the electrode chip. Chip includes different size, individually addressable, concentric disk-ring microelectrodes, and the same size microband electrodes, however only the disk-ring microelectrodes were used for this study. **(b)** Expanded view of the one set of microelectrodes. **(c)** Experimental set-up used for the redox-MHD studies. A 0.5 in. × 1.0 in. 0.36 T NdFeB cylindrical permanent magnet is placed underneath electrode chip to generate the MHD force, when a constant potential is applied at the on-chip electrodes immersed in the $K_3Fe(CN)_6$, $K_4Fe(CN)_6$), KCl solution containing polystyrene latex beads and red dye.

solvent (Ellsworth Adhesives, Milwaukee, WI) were used to fabricate the poly(dimethyl siloxane), PDMS gasket.[16] Pre-cleaned microscope glass slides (1.5 × 1.0 × 0.1 in.^{3}) were purchased from VWR.

3.3.2 Electrode Chip Design

A 2.0 in. (length) × 1.0 in. (width) chip contained multiple design features, but only the concentric disk-ring microelectrodes were used for this study (Figure 3.1a). The individual electrodes were 100.0 nm thick, and have different sizes; disk radius: 16, 38, 79, and 156 µm; inner ring radius: 200, 400, 800, and 1600 µm; outer ring radius: 250, 500, 1000, and 2000 µm, respectively. See Figure 3.1a and 3.1b. Electrode radius was measured using an optical microscope, whereas the thickness was measured with an uncalibrated piezoelectric monitor connected to the thermal evaporator (Edwards Auto 6 Evaporator). Electrode chip was fabricated using a method described in one of our previous work.[19]

3.3.3 Experimental Setup

The electrode chip was connected to a CHI 760B bipotentiostat (CHI Instruments, Austin, TX) with an edge connector (solder contact, 20/40 position, 0.05 in. pitch) purchased from the Sullins Electronics Corp. (San Marcos, CA). All electrochemical studies were performed at the room temperature using an equimolar mixture of potassium ferri and ferrocyanide in the potassium chloride electrolyte solution. A 1.0 mL sample containing 0.1 M $K_3Fe(CN)_6$, 0.1 M $K_4Fe(CN)_6$ in 0.1 M KCl was mixed with 50.0 µL of polystyrene latex microbeads to prepare a stock solution (changing the actual solution concentration to 95% of the original value) for the bead tracking studies. For the red dye experiments the solution concentration was increased to 0.3 M $K_3Fe(CN)_6$, 0.3 M $K_4Fe(CN)_6$ in 0.1 M KCl but without

polystyrene latex beads in it. The PDMS gasket used to contain redox species solution had a rectangular opening (14.3 mm wide, 27.0 mm long and 620.0 µm thick) in it, thus leaving disk-ring electrodes open to contact with the solution. See Figure 3.S2. A 300 µL stock solution was poured inside this PDMS placed over the chip. PDMS was covered with a microscope glass slide (with and without holes in it for the red dye and bead tracking studies, respectively), thus making a closed electrochemical cell with its dimensions defined by the PDMS thickness and size of the rectangular opening. See Figure 3.S3 and S4 a, b. Whole chip assembly was placed under a microscope (LEICA DM 2500M, NIKON) with the magnet underneath, and the bead/red dye movement was recorded using SONY HDR-XR 500V camcorder connected to the microscope (Figure 3.1c).

Cyclic voltammetry, CV, characterization of individual disk and ring electrodes was performed in the absence of the magnetic field, and without microbeads in the solution, using a three-electrode setup. See Figure 3.S1. A further comparison with the Digisim simulations was made, thus confirming the quality of the electrodes to be used. See Supporting Information.. All the redox-MHD studies were performed using chronoamperometry, CA, in a two-electrode setup (on-chip disk electrode as the working, and the corresponding ring as counter/reference shorted together). The disk-ring electrode set 3 and 4 were used for the bead tracking and red dye studies, and a potential of -0.6 V and +0.4 V was applied at the disk electrode 3 and 4, respectively. Fluid flow was recorded across the radial gap between disk and ring electrode surfaces, at an electrochemical cell height of 160.0 and 245.0 µm above the chip surface, respectively, for both the cases. The velocity data were obtained by processing the bead movement videos using particle image velocimetry, PIV (Dantec Dynamics), software.[19,20] Data analysis started 20 s after the application of potential step, and is reported over a single

hypothetical x-z plane cutting the disk-ring electrode region into two equal parts. See Figure 3.3a and 3b. As the field of view for microscope was smaller than the disk-ring set 4, therefore the region around disk electrode was mapped only for the red dye experiments. The use of set 4 microelectrodes was considered due to a comparatively stronger MHD force at the large size disk electrode. Approximately 5-10 µL red dye sample was inserted using Pasteur pipette to the on-chip solution, via a 1 mm diameter hole drilled in the microscope slide. See Figure 3.S4. Dye insertion was carefully practiced to minimize the impacts of external forces on the sample's natural movement. Glass slide had two same sized holes in it, and the second hole allowed the release of pressure generated with the dye insertion, by exiting the displaced solution. For control experiments the camcorder was switched on as soon as the dye was inserted, however for the full experiments a time lag was kept between dye insertion and the onset of redox-MHD pumping, to better observe the effects of fluid circulation. Since the movement of dye was visible with the naked eyes as well as the video camera, therefore as soon as dye reached closer to the disk surface, redox-MHD pumping was switched on in the full experiment. In between the experiments, chip was cleaned using deionized water and ultrapure argon gas, and a fresh volume of redox/redox-bead solution was introduced for the new experiment.

3.4 Results and Discussion

3.4.1 Observing Redox-MHD Fluid Rotation by Bead Tracking

Fluid velocity data obtained by tracking polystyrene latex beads shows a circular movement between disk-ring microelectrodes. See Figure 3.3a. For a constant magnetic field and distant location from the PDMS cell walls**,** redox-MHD fluid flow is determined by the distribution of ionic current density.[17,19] Assuming cylindrical symmetry for the disk electrode,[21]

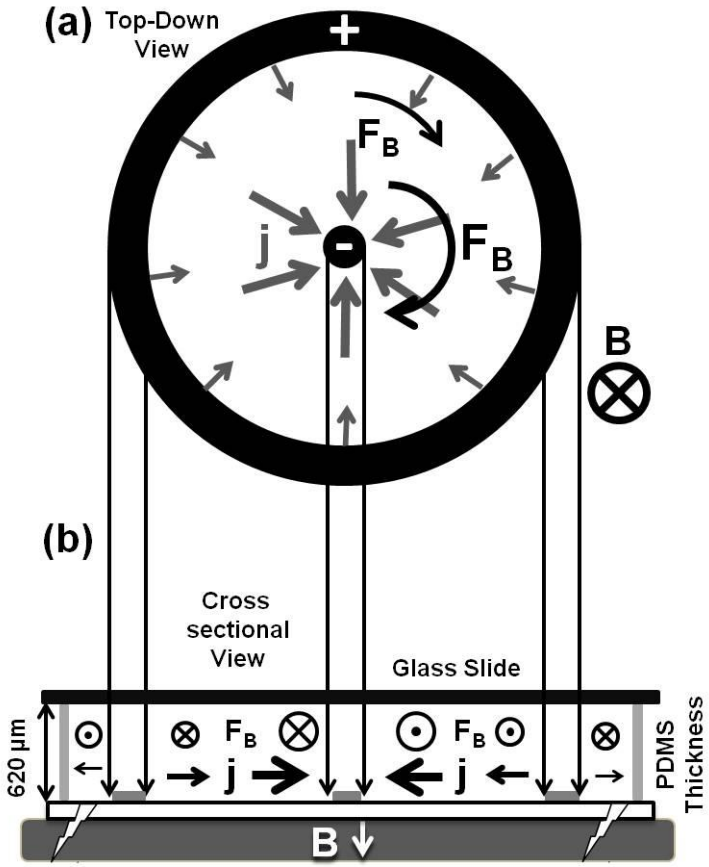

Figure 3.2 Redox-MHD fluid rotation working mechanism. **(a)** Top-down view of the fluid flow direction. At the region between oppositely biased disk-ring microelectrodes, MHD force moves the fluid in a circular direction with a strong force close to the disk surface due to a higher ionic current density there. **(b)** Cross sectional view of the redox-MHD fluid flow for the given disk-ring electrode set. Electrochemical conversion at the disk electrode/solution interface generates a net ionic current density toward the disk electrode, and in the presence of an external magnetic field the MHD force generates a fluid flow with its direction given by the right hand rule.

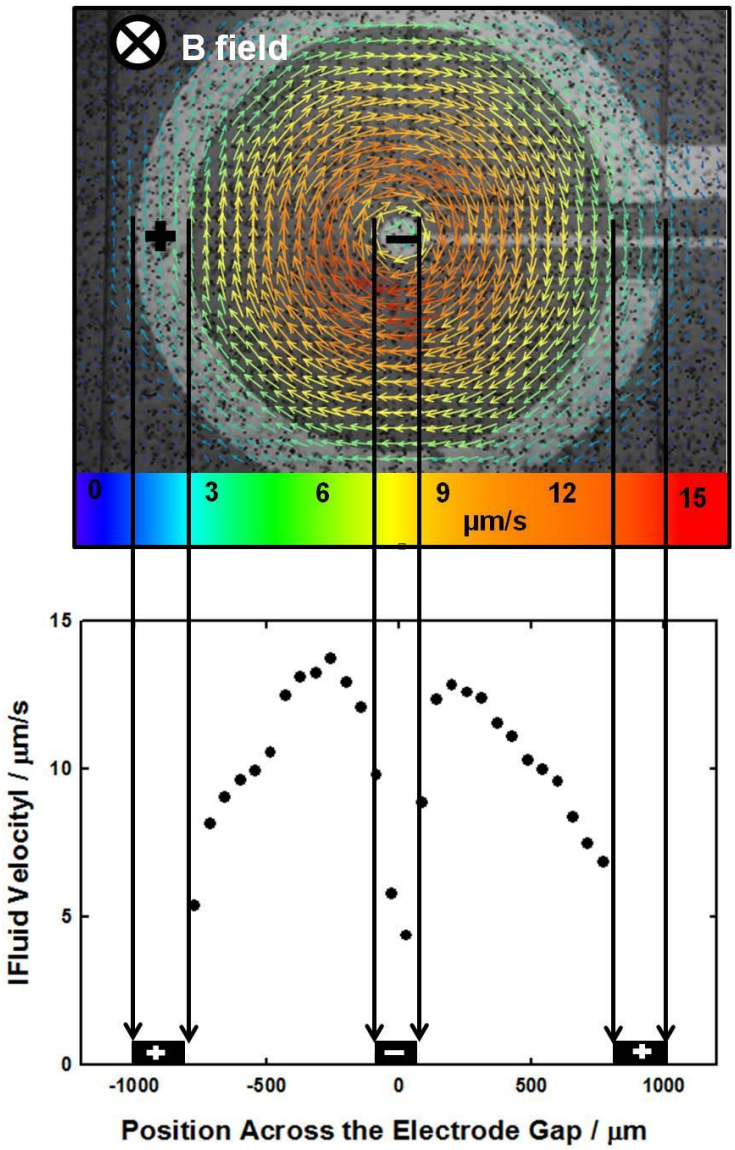

Figure 3.3 Redox-MHD fluid rotation using polystyrene latex bead tracking. **(a)** Redox-MHD fluid flow imaged by the particle image velocimetry (PIV) software. The data were processed 20 s after the application of -0.6 V potential at the disk electrode, and at a height of 160 µm above the chip surface. **(b)** The fluid velocity at a region between disk and ring surfaces is plotted as a function of distance. An imaginary x-z plane was marked dividing disk-ring electrode set in to two equal parts, and the velocity reported in this figure was measured over the x-direction of that plane. Velocity drops as the measurement distance increases radially from the disk electrode toward the inner ring, due to a decrease in the ionic current density.

and at a fixed height (z-coordinate) above the chip surface, the ionic current density drops radially ($j \alpha 1/r$) in the outward direction. Figure 3.3b demonstrates similar behavior with a strong MHD force close to the disk electrode, which drops radially after increasing up to a distance that extends close to the diffusion layer thickness (~200 μm). Less velocity at the disk electrode is expected due to the opposing surface forces acting against the fluid flow, thus decreasing the influence of the MHD force. Direction of ionic current vectors should also affect the fluid movement here, which might cause a zero MHD force in the directions that are parallel with the magnetic field. Therefore, overall, the fluid velocity has decreased reaching close to the disk electrode edge. However, with an increasing distance from the disk electrode the redox-MHD convection dominates; this increased the fluid velocity up to a location close to the diffusion layer thickness. Thereafter, the velocity decreased due to its radial dependence on the ionic current density; however the dependence is not strongly linear ($R^2 = 0.9597$). A weak linearity might be due to a large depth of focus (DOF) of the microscope, averaging bead movement above and below the fixed measurement height. On the other hand, the ring electrode would also generate an MHD force based upon the opposite electrochemistry from that of the disk. Because of the large ring size the ionic current density has a weak distribution, and hence a weak MHD force, thus the associated fluid flow is primarily due to the processes taking place at the disk electrode. Moving outside the ring electrode, the ionic current distribution should also be negligible; the direction of bead movement suggests a similar behavior: a weak fluid flow that is still dependent upon MHD force generated at the disk electrode.

3.4.2 Visualizing Redox-MHD Fluid Rotation with a Red Dye

Effects of redox-MHD fluid circulation on an external red dye sample are given in Figure 3.4. Two types of experiment were performed, with (full) and without (control) redox-MHD

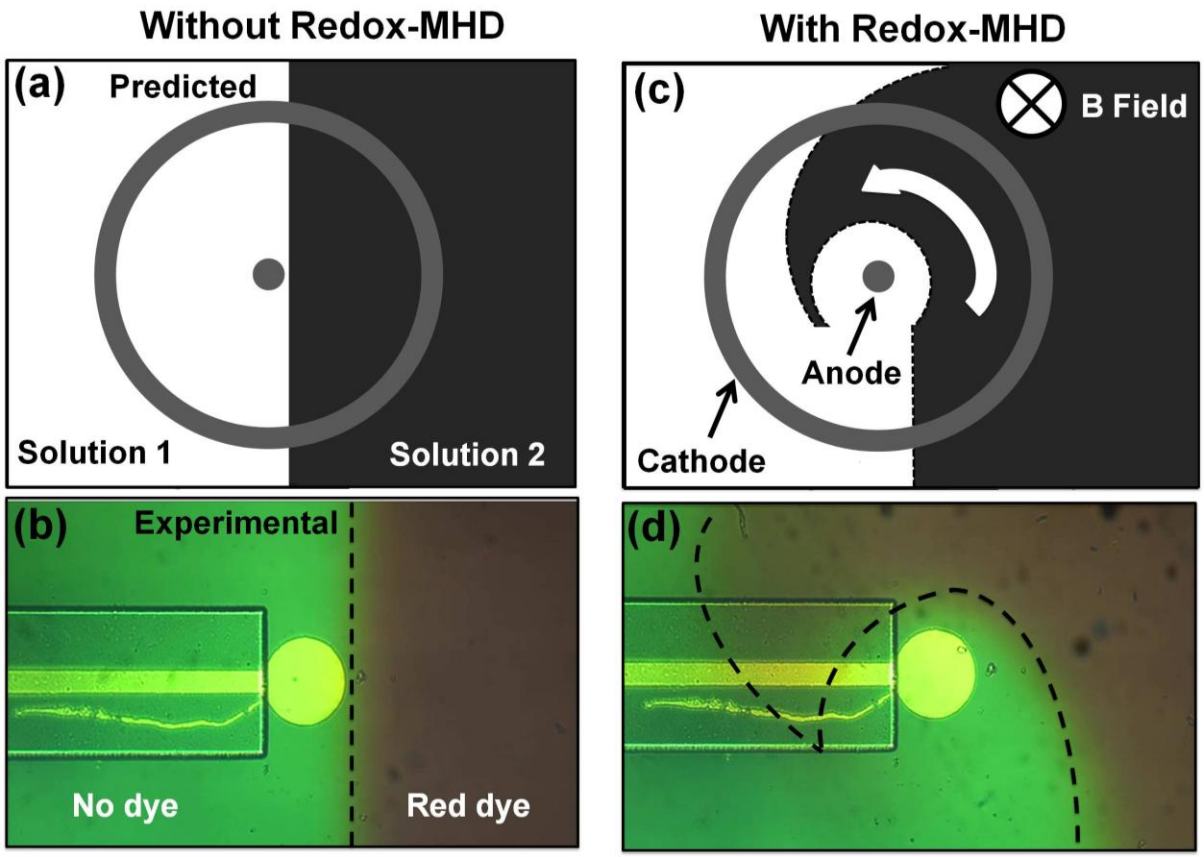

Figure 3.4 Visualizing redox-MHD fluid rotation using red dye. **(a)** Predicted, and **(b)** experimentally measured movement of the externally added red dye without redox-MHD force, and due to its natural movement only. **(c)** Predicted and **(d)** experimentally observed movement of the red dye under the redox-MHD conditions. A potential of +0.4 V was applied for 180 s at the 156 µm radius disk electrode, in the presence of a 0.36 T NdFeB permanent magnet, and the red dye movement was recorded at a 245 µm height above the chip surface. A stronger MHD force near the disk surface moves the red dye in a circular fashion. In Figure b and d, the presence of undesired stripe of gold layer did not affect the final results as it was covered and insulated by the thick BCB layer on it.

convection.

For control experiments the red dye movement is shown in Figure 3.4b. Intuitively, due to minimal external forces, the dye would have travelled inside the solution without any particular flow pattern. Expected and measured results given in Figure 3.4a and 3.4b were a good match for each other, thus confirming the notion of doing the control experiment. Image given in Figure 3.4b was captured at the 76^{th} s of the video recording, but a complete time evolution of the dye under similar conditions is given in Figure 3.S5. Effects of redox-MHD circulation on the dye are also given in Figure 3.4d. Glass slide location and the dye insertion point were both designed in a similar way as used in the previous part. Intuitively, the dye circulation was predicted with the onset of the MHD force (See Figure 3.4c), and experimentally (See Figure 3.4d) a similar behavior was observed. As the dye reached close to the disk surface, a strong MHD force at the disk diverted its path to move the dye in a circular direction, thus confirming the influence of redox-MHD pumping. It may also be noted here that for the whole duration of the experiment, the dye was moving under the combined influence of redox-MHD convection, density gradients induced-natural convection, and natural diffusion; however the circular nature of this path is due only to the redox-MHD convection. A time evolution for the dye circulation under these conditions is also given in Figure 3.S6. Results obtained for the red dye sample are consistent with the polystyrene latex bead tracking studies (See Figure 3.3a and 3.3b), thus confirming the radial nature of MHD force around the disk electrode. Results also demonstrate the capability of the redox-MHD circulation to move an external sample to the sites having immobilized species, important for the lab-on-a-chip immunoassay applications. The effects of MHD convection can further be tuned by increasing the magnetic field strength or the electrode size.

3.5 Conclusions

The redox-Magnetohydrodynamics (MHD) microfluidics is capable of inducing a fluid rotation using on-chip concentric disk-ring microelectrodes, without using channels. The attainment of microfluidic circulation provides an important feature that can be exploited for the lab-on-a-chip device applications, such as the immunoassays or the DNA hybridization assays. Redox-MHD circulation is further expected to enhance the rate of interaction between different analytes, and hence may provide an overall improvement in the analysis time as well as the device sensitivity.

3.6 Acknowledgement

We are thankful to the National Science Foundation (Grant number: CHE-0719097), and the Arkansas Biosciences Institute, the major research component of the Arkansas Tobacco Settlement Proceeds Act of 2000, for their financial support.

3.7 Supporting Information

Supporting information includes CV characterization of the individual disk-ring microelectrodes, poly(dimethylsiloxane) gasket placement schematics with reference to the electrodes, fluid circulation PIV imaging, schematics for the red dye insertion and its monitoring, time evolution of red dye with and without redox-MHD convection and the Reynolds number calculations.

3.8 References

1. H. Craighead, *Nature*, 2006, **442**, 387-393.

2. S. Mouradian, Current Opinion in Chemical Biology, 2002, **6**, 51-56.

3. P. S. Dittrich and A. Manz, *Nature Reviews Drug Discovery*, 2006, **5**, 210-218.

4. S. Haeberle and R. Zengerle, *Lab on a Chip*, 2007, **7**, 1094-1110.

5. D. Erickson and D. Q. Li, *Analytica Chimica Acta*, 2004, **507**, 11-26.

6. M. Stenberg and H. Nygren, *Journal of Immunological Methods*, 1988, **113**, 3-15.

7. M. Sigurdson, D. Z. Wang and C. D. Meinhart, *Lab on a Chip*, 2005, **5**, 1366-1373.

8. H. Zhao and H. H. Bau, *Physical Review E*, 2007, **75**.

9. R. C. Yeh, J. K. Hyun, A. K. Boehm, J. T. Lis and C. Franck, *Journal of Biochemical and Biophysical Methods*, 2005, **64**, 59-68.

10. C. Y. Lee, C. L. Chang, Y. N. Wang and L. M. Fu, *International Journal of Molecular Sciences*, 2011, **12**, 3263-3287.

11. M. Z. Bazant and Y. X. Ben, *Lab on a Chip*, 2006, **6**, 1455-1461.

12. N. Pamme, *Lab on a Chip*, 2006, **6**, 24-38.

13. P. U. Arumugam, E. S. Fakunle, E. C. Anderson, S. R. Evans, K. G. King, Z. P. Aguilar, C. S. Carter and I. Fritsch, *Journal of the Electrochemical Society*, 2006, **153**, E185-E194.

14. M. C. Weston, M. D. Gerner and I. Fritsch, *Anal Chem*, 2010, **82**, 3411-3418.

15. H. J. Kang and B. Choi, *Sensors and Actuators a-Physical*, 2011, **165**, 439-445.

16. E. C. Anderson, M. C. Weston and I. Fritsch, *Analytical Chemistry*, 2010, **82**, 2643-2651.

17. M. C. Weston and I. Fritsch, *Sensors and Actuators B-Chemical*, 2012, **173**, 935-944.

18. M. C. Weston, C. K. Nash and I. Fritsch, *Analytical Chemistry*, 2010, **82**, 7068-7072.

19. V. Sahore and I. Fritsch, *Analytical Chemsitry*, Submitted July 2013.

20. P. G. Scrape, M. D. Gerner, M. C. Weston and I. Fritsch, *Journal of the Electrochemical Society*, 2013, **160**, H338-H343.

21. A. J. Bard and F. L. R., Electrochemical Methods: Fundamentals and Applications, Wiley, New York, 1980.

3.S Supporting Information: Microfluidic Rotational flow obtained by Redox-Magnetohydrodynamics (MHD) Pumping

Supporting information includes CV characterization of the individual disk-ring microelectrodes, poly(dimethylsiloxane) gasket placement schematics with reference to the electrodes, fluid circulation PIV imaging, schematics for the red dye insertion and its monitoring, time evolution of red dye with and without redox-MHD convection and the Reynolds number calculations.

3.S1 Disk-Ring Microelectrode Characterization

The individual disk and ring microelectrodes were characterized using cyclic voltammetry (CV), before they were used for the fluid circulation studies. Representative CV responses are given in Figure 3.S1. They were obtained without microbeads or red dye in a static solution of 20 mL 0.1 M $K_3Fe(CN)_6$, 0.1 M $K_4Fe(CN)_6$, and 0.1 M KCl contained in a beaker, where the chip was positioned vertically, using a three-electrode setup with a Pt flag counter and Ag/AgCl (saturated KCl) reference electrodes. CV was performed by scanning from 0.6 V to -0.1 V at 0.05 V/s, and with 0.6 V as the initial potential held at a 2 s quiet time prior to the initial forward scan. A correlation with the expected behavior was found using currents calculated from the Digisim (Bioanalytical Systems Inc., West Lafayette, IN) simulations, which confirmed the quality of the electrodes to be used for further studies. For a single electron transfer homogenous reaction, the maximum theoretical current measured from the zero current line was 5.2, 20.0, 252.0, and 825.9 µA for the disk 3-4 and ring 3-4 electrodes, respectively. Double layer capacitance (C_{dl}) used for the Digisim calculation was 0.0200, 0.0804, 1.1304, and 4.5200 µF, whereas the uncompensated resistance was 3467, 1489, 264, and 180 Ω for the disk 3-4 and ring 3-4 electrodes, respectively. Other Digisim parameters were the same as given in the experiments. The experimental maximum currents measured from the zero current baselines were 5.5, 20.0, 240, and 750 µA for the disk 3-4 and ring 3-4 electrodes, respectively. Except ring 3, the experimental and theoretical currents are well matched to each other; a possible reason for the observed difference for ring 3 might be the variations in the actual and theoretical electrode size. Peak splitting is 120, 120, 170, and 320 mV for the disk 3-4 and ring 3-4 electrode, respectively, the corresponding numbers from Digisim simulations were 108, 139, 230, and 420 mV, respectively. This is much larger than the ~ 60 mV expected for a kinetically

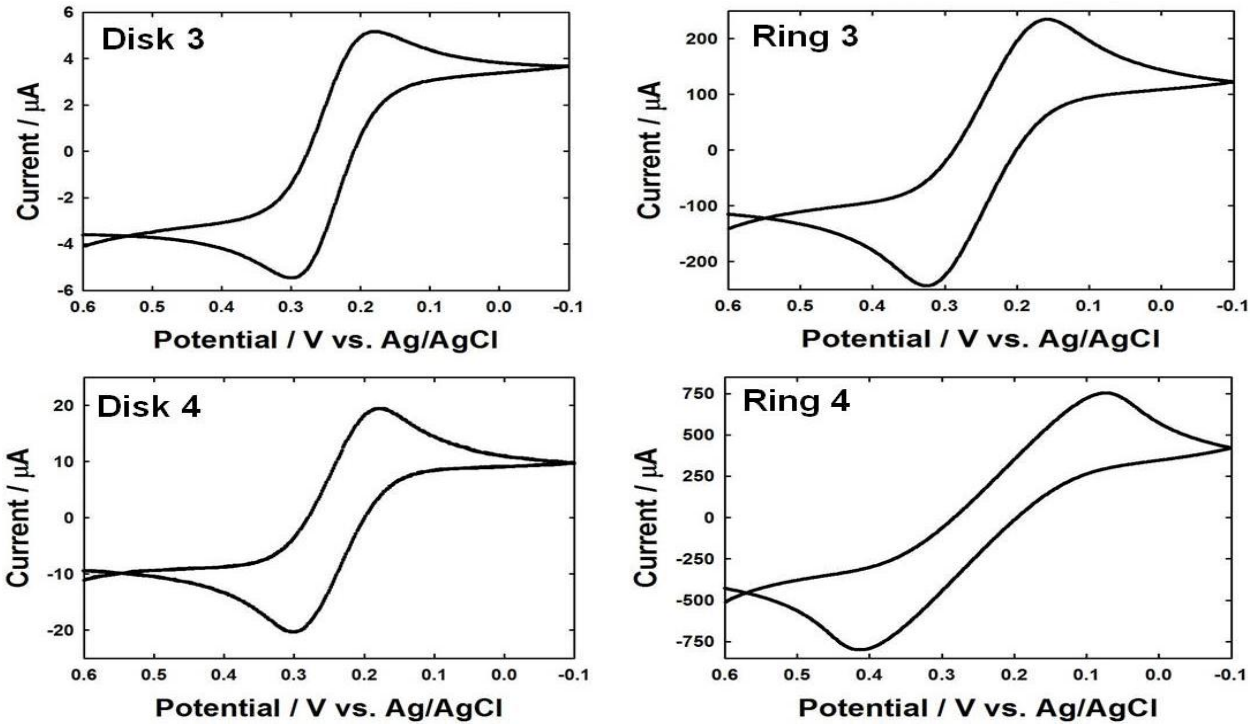

Figure 3.S1 Individual disk and ring microelectrodes were characterized by cyclic voltammetry in a beaker containing 20 mL static solution of 0.1 M $K_3Fe(CN)_6$, 0.1 M $K_4Fe(CN)_6$, and 0.1 M KCl (without polystyrene microbeads), and in the absence of a magnet. A three-electrode configuration was used for the CV experiments. Here the individual disk and ring served as the working electrode, a Pt flag as the counter electrode, and Ag/AgCl (saturated KCl) as the reference electrode.

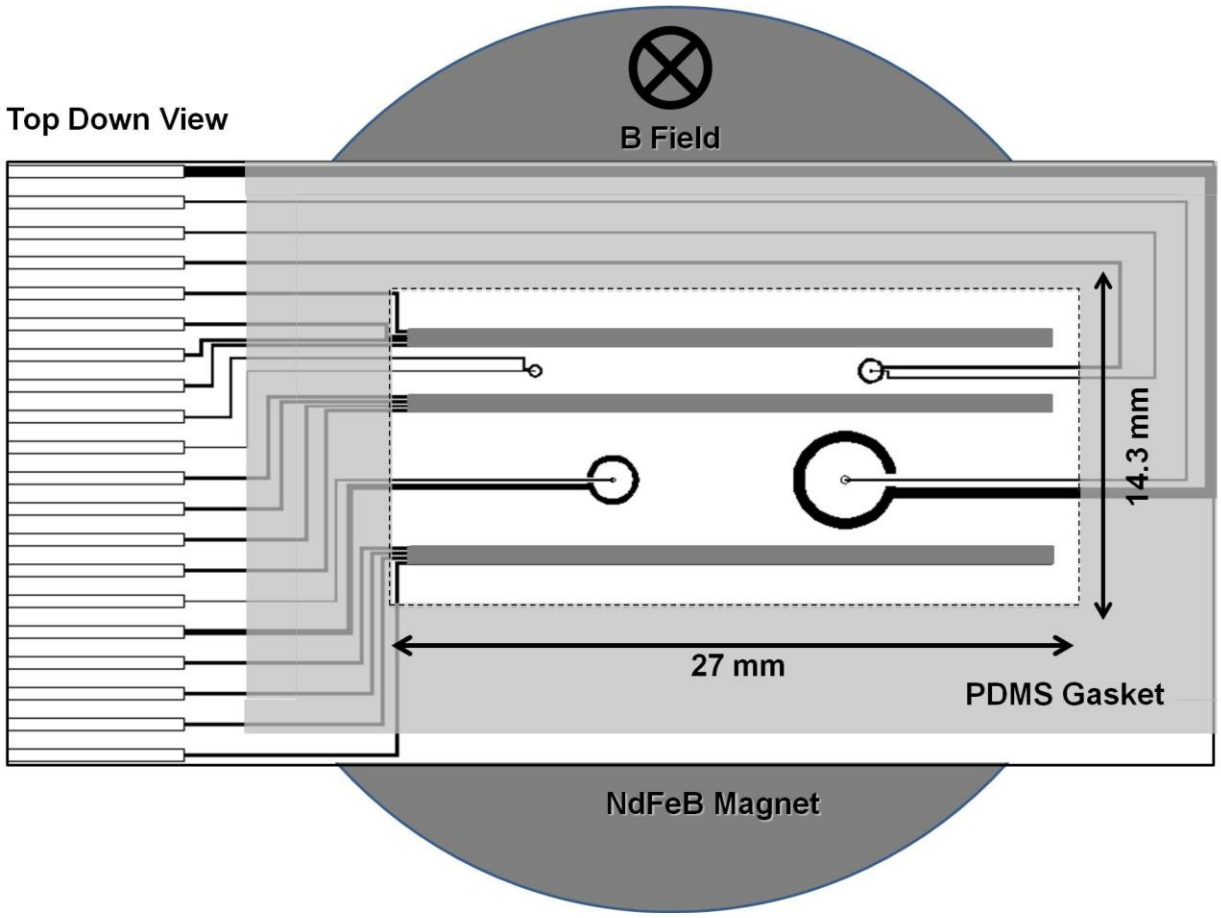

Figure 3.S2 Schematic shows the location of the PDMS gasket (light gray) relative to the electrode positions. The opening (14.3 mm wide × 27.0 mm long) is outlined by dashed lines, and the height (620.0 μm) is not shown in the figure. A single chip has four different sets of disk-ring microelectrodes; each set is represented by the black color. The black/gray lines on the left/right side of those electrodes indicate the BCB-insulated leads. The disk-ring electrode set 3 and 4 were used for the redox-MHD studies. The redox species solution dispensed into the open region was contained by the PDMS sidewalls and a microscope slide placed on top (not shown). All the redox-MHD studies were performed inside the PDMS reservoir by applying a constant voltage at specific electrodes.

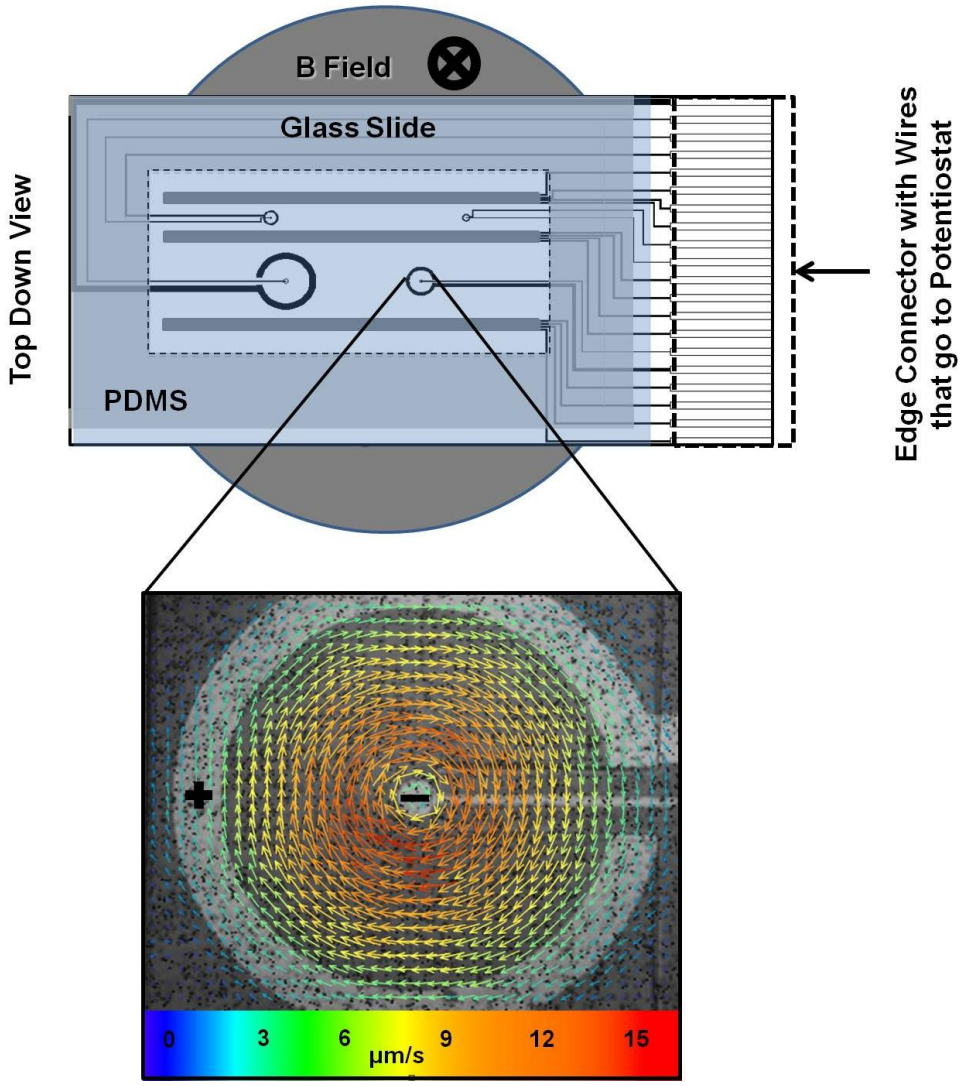

Figure 3.S3 Polystyrene latex bead tracking processed by the particle image velocimetry (PIV) software. The microbead movement was recorded in a solution containing 0.095 M $K_3Fe(CN)_6$, 0.095 M $K_4Fe(CN)_6$), 0.095 M KCl, and polystyrene latex beads (2.5 % wt dispersion in water), and in the presence of a 0.36 T magnetic field. (a) Figure shows top-down view of the set-up, and illustrates the small disk-ring electrode set 3, over which the PIV image is taken. (b) Expanded view of redox-MHD circulation PIV image captured over the disk-ring electrode set 3, 20 s after the application of potential, and at a height of 160 µm above the chip surface. The direction and magnitude of the microbead velocities indicate radial dependence for the fluid flow between the disk and ring microelectrodes.

reversible redox couple, where n = 1. A possible source for this deviation is the effects of uncompensated resistance, which are significant even at the microelectrodes. The above reported, measured value for uncompensated resistance with 0.1 M KCl solution using potentiostat's built-in function is sufficient to cause the peak splitting of the observed nature.

3.S2 PDMS and the Particle image velocimetry Schematics

Figure 3.S2 shows the PDMS schematics drawn to scale relative to the electrode locations over the chip. After PDMS fabrication, it was carefully cut from the inside to make a gasket shape that can withhold redox species solution.

Figure 3.S3 shows top-down view of the redox-MHD fluid circulation set-up, and a captured PIV image as an expanded view. Here the disk electrode was kept at the reduction potential of -0.6 V, and the bead velocity was measured at 160 μm above the chip surface, starting 20 s after the application of potential.

3.S3 Red Dye Insertion and Its Time Evolution With and without redox-MHD Convection

Figure 3.S4 shows the schematics for red dye insertion, and the region over which its movement was measured. A glass slide having two holes in it was strategically placed on top of the chip assembly to facilitate the dye insertion, and its subsequent movement recording. Two, 1 mm diameter holes were drilled in to the glass slide using a diamond coated drill bit, and the placement of glass slide was such that one hole is exactly facing the disk electrode. Red dye was inserted using a Pasteur pipette while minimizing the insertion forces with careful monitoring of the insertion procedure. Time evolution of the dye movement is given for both the control and full experiments in Figure 3.S5 and 3.S6. Figure 3.S5 shows the dye path without applied potential and magnetic field. As soon as the dye enters redox solution, it exerts a pressure on the

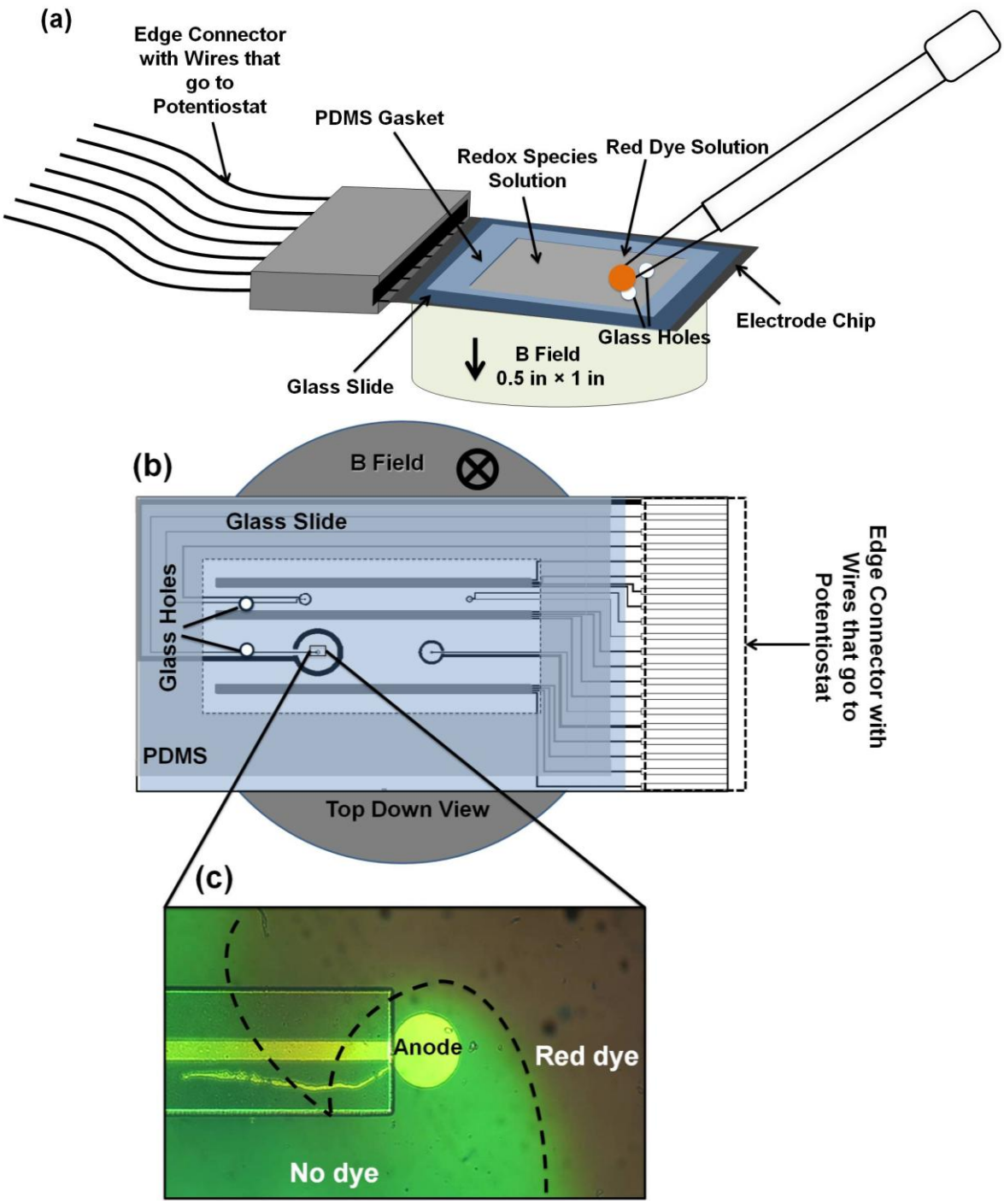

Figure 3.S4 Red dye insertion and its monitoring under redox-MHD fluid flow. **(a)** A red dye sample was inserted into redox solution via 1 mm hole drilled in the microscope glass slide. The glass slide has two same size holes (white circles) in it. **(b)** Top-down view shows the placement of drilled glass slide, it also illustrates the region over which red dye movement was recorded. **(c)** The captured movement of the externally added red dye sample under redox-MHD circulation at 13th second after applying a constant potential.

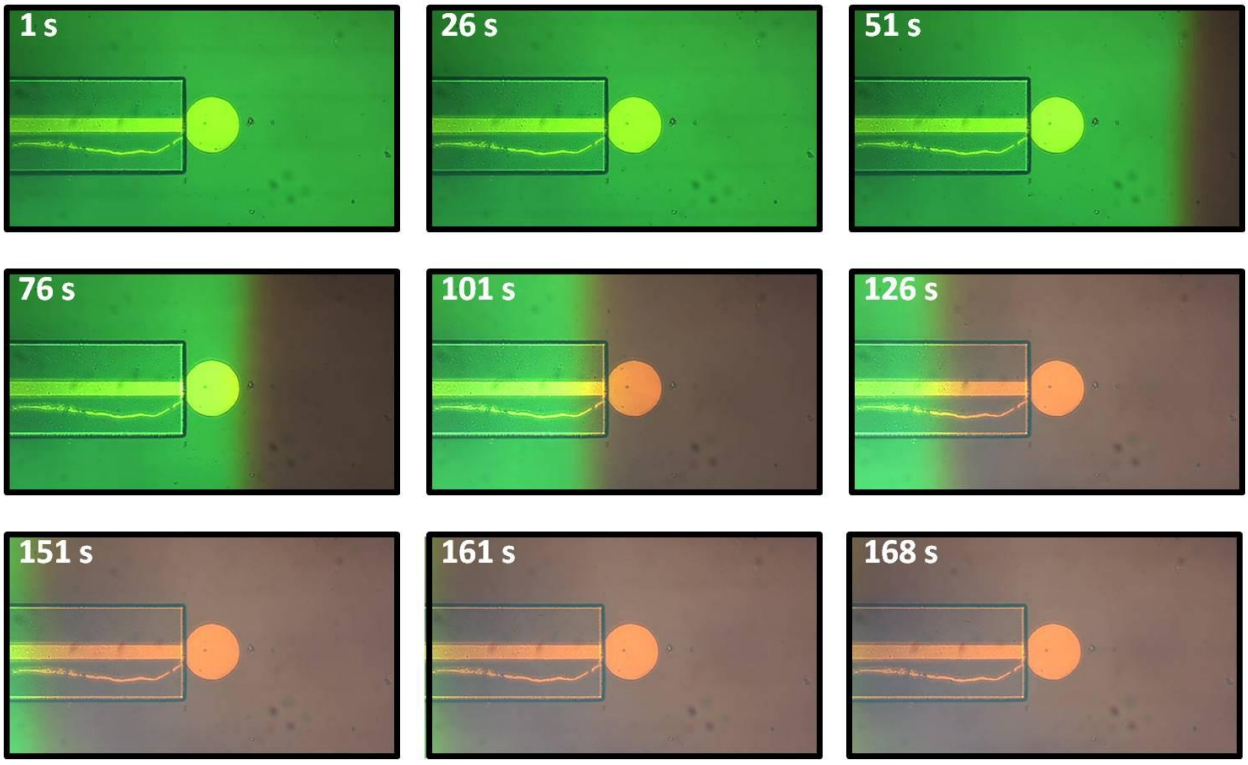

Figure 3.S5 Red dye's natural movement with time, without redox-MHD convection. Dye was inserted using similar method shown in Figure 3.S4, however no potential was applied, and there was no magnet underneath the electrode chip. As predicted, the dye sample continued to move forward without any flow pattern. The movement was recorded for 168 seconds, and the captured images at different times are given here.

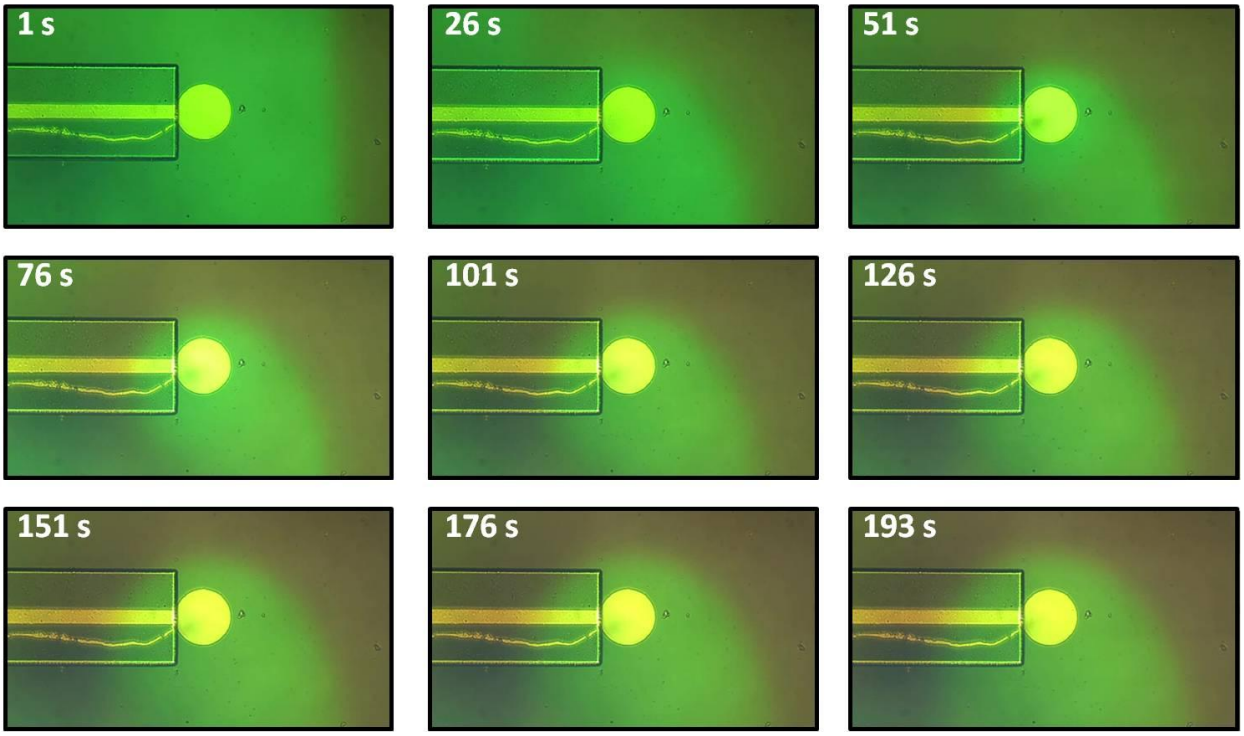

Figure 3.S6 Red dye's movement with redox-MHD convection over time. Dye was inserted using a method similar to figure 3.S4, with an applied potential of + 0.4 V, a 0.36 T NdFeB magnet underneath the electrode chip. As predicted the dye sample continued to follow a path under the combined effect of natural diffusion and the redox-MHD convection. The potential was applied for 180 seconds; however the video recording had started 13 seconds before the potential was applied. A series of figure above shows the movement of red dye at different times.

surroundings, since the solution is enclosed from all sides the second hole in the glass slide acts as a pressure relief, which allows an exit for the displaced solution. The dye movement was recorded for 168 s, and the captured images in Figure 3.S5 were taken at 1, 26, 51, 76, 101, 126, 161, and 168th s. Redox-MHD circulation effects were also studied with the red dye, however by applying -0.6 V potential and in the presence of 0.36 NdFeB magnet. Although videos were recorded for a total time of 193 s, the potential was applied only for 180 s. The captured images in Figure 3.S6 were taken at 1, 26, 51, 76, 101, 126, 151, 176, and 193rd s.

3.S4 Reynolds Number

Redox-MHD circulation is induced under the laminar flow conditions as calculated by the Reynolds number, Re. Reynolds number is the ratio of inertial to viscous forces[1] and is determined by

$$Re = \frac{\rho v l}{\mu} \qquad \text{(Eq. 3.S1)}$$

Here, ρ is the solution density, v the mean fluid flow velocity, l the hydraulic diameter given by 4 × cross sectional area / wetted perimeter[2,3], and μ is the dynamic viscosity. Value for the Reynolds number for disk-ring electrode set 3 under redox-MHD fluid circulation conditions is 0.03 (where ρ = 1045.39 kg/m3, v = 14 μm/s, l = 2 × (inner ring radius – disk radius) = 1760, μ = 8.4849 × 10-4 kg/m.s). Reynolds number < 1 confirms that the solution in the device is under laminar flow conditions.

3.S5 References

(1) Squires, T. M.; Quake, S. R. *Reviews of Modern Physics* **2005**, *77*. 977-1026.

(2) Munson, B. R.; Young, D. F.; Okiishi, T. H. *Fundamentals of Fluid Mechanics*, 5th ed.; John Wiley & Sons, 2006.

(3) Nguyen, N. T.; Wereley, S. T. *Fundamentals and Applications of Microfluidics*, 2nd ed.; Artech House, Inc. , 2006.

4. Redox-Magnetohydrodynamics (MHD) Flat Flow Profile Guided Enzyme Assay Detection: Toward multiple, parallel analyses

This chapter was written in a format to be submitted as a manuscript to the journal Analytical Chemistry. Work in this chapter is a proof-of-concept study utilizing redox-magnetohydrodynamics (MHD) flat flow profile microfluidic feature toward multiple, parallel chemical analyses on a single chip.

4.1 Abstract

A proof-of-concept magnetic microbead enzyme assay was integrated with redox-magnetohydrodynamics (MHD) microfluidics to take advantage of the magnet beneath the chip and the uniform flat flow profiles, as a first step toward developing multiple, parallel chemical analysis on a chip. A bead-enzyme complex was formed by reacting biotinylated alkaline phosphatase (AP, a common enzyme label for biochemical assays) with streptavidin coated superparamagnetic beads. This complex was immobilized selectively at different on-chip locations using the inherent presence of a NdFeB permanent magnet beneath the chip that is needed for producing the MHD force. Electroactive species *p*-aminophenol (PAP_R), enzymatically generated at the bead-enzyme complex from its electroinactive precursor *p*-aminophenyl phosphate (PAPP) in a solution containing a redox species $[Ru(NH_3)_6]^{3+/2+}$ and Tris buffer, was transported downstream by redox-MHD with a flat flow profile and detected through oxidation at 320 μm diameter gold microdisk stationed on the fluid flow path. Pumping of fluid at < 38 μm/s from the enzyme-bead complex to the detector was achieved by a pair of flanking, oppositely biased band electrodes that were 2.5 cm long and separated by 5.6 mm gap, where oxidizing and reduction of the redox species took place. Three different locations that were ~3 μm upstream from the detector were chosen for immobilizing the bead-enzyme complex. One immobilization location lay directly on the path to detector, the other two were adjacent to the first and off the path by a distance > 5 times the diameter of the detector. The flat flow profile minimized the cross-over from parallel paths. The greatest signal at the detector was produced by the arrival of PAP_R from the bead-enzyme complex that lay upstream directly on the path to detector, whereas signal for the complex in adjacent paths was only 20% of this position. The

signal was only 8% when pumping electrodes were left off, but otherwise the bead enzyme complex was placed upstream at the position directly laid on the path to detector.

4.2 Introduction

In this work we have integrated a magnetic microbead enzyme complex with the redox-magnetohydrodynamics (MHD) microfluidics, as a proof-of-concept toward the development of multiple, parallel chemical analysis on a silicon chip. This was accomplished by combining redox-MHD flat flow profile with the selective placement of microbead enzyme complex by taking advantage of NdFeB magnet beneath the chip. It was further shown herein that the fluid containing electroactive species of *p*-aminophenol (PAP_R) travels undistorted due to the uniform flow profile, and gets detected at the electrode lying directly on its horizontal flow path, whereas it generates a minimal signal for locations adjacent to this position due to a minimized cross-over from parallel paths. Multiplexing is essential for lab-on-a-chip applications and integrates detection of multiple analytes as well as multiple detections of an analyte on a single chip, and hence decreases total analysis time, reduces operational cost, and improves overall device efficiency.

With continuous progress in point-of-care diagnostics technology more than one analysis on the same chip at approximately same time, has become important for the analytical devices.[1-5] The multiple, parallel analysis on a single platform need undistorted movement of small fluid volumes, and flat flow profile is one way to achieve this.[6, 7] Traditionally this microfluidic feature has been achieved using electro-osmotic flow, but it require the use of microchannels as well as the application of high voltages, which limit its design options and create problems associated with the heat generation, bubble formation, and electrode degradation.[8] Uniform flat flow profiles using a relatively new pumping method of redox-MHD have been achieved previously at the scales suitable for lab-on-a-chip applications, but greater than those using electro-osmotic flow. To broaden the scope of redox-MHD flat flow profile toward multiple,

parallel analysis, the magnetic bead enzyme assay is one possibility as it can then also utilize the inherent presence of a magnetic field required for redox-MHD pumping to allow more flexibility in the assay immobilization process. Magnetic bead assays have been integrated with microfluidics systems before in the past using flow cytometry, syringe pump, and electro wetting techniques[9-12]; however their combination with redox-MHD pumping would remove the requirement of microchannels as well as any external parts for its operation.

MHD is governed by magnetic part of the Lorentz force equation, $\mathbf{F_B = j \times B}$, with its direction given by right hand rule. Here **j** is the ionic current density of a fluid element (C/m^2), **B** (Tesla) is the magnetic flux density, and $\mathbf{F_B}$ (N/m^3) is MHD body force acting on the fluid element.[13-15] In the absence of easily available oxidized and reduced species the traditional MHD pumps require the application of high voltage, thus creating the problems of bubble generation and electrode degradation.[16-18] However, using redox species that can sustain faradaic current at low overpotential, problems associated with traditional MHD in electrolyte solution can be resolved; this alternative approach is coined as 'redox-MHD'. Redox-MHD generates a channel-less fluid flow with a simple device designed by the careful control of ionic current density through various electrode shapes and magnetic field.[19-22]

Herein, two advantageous features of redox-MHD will be harnessed, the flat flow profile and the presence of the magnet to immobilize magnetic beads, to demonstrate the capability of redox-MHD in multiplex assays and detection on a small scale. The MHD pumping force was generated by applying a constant potential across the microband electrodes in contact with ruthenium hexamine (II) chloride and ruthenium hexamine (III) chloride solution in Tris buffer, and in the presence of NdFeB permanent magnet underneath the chip. Electroactive species of p-amino phenol generated by the reaction between p-amino phenyl phosphate and alkaline

phosphatase derivitized superparamagnetic bead complex, were detected at the disk microelectrode lying in the horizontal flow path of the species. Studies were also performed by immobilizing alkaline phosphatase derivitized superparamagnetic bead complex at locations off the horizontal path of detector. A further comparison of *p*-amino phenol detection current signal from different enzyme locations on the chip was made to assess the effects of flat flow profile.

4.3 Experimental Section

4.3.1 Chemicals and Materials

All chemicals were reagent grade and used as received. Aqueous solutions were prepared using high purity deionized water purchased from Ricca Chemical Company, Arlington, TX. Ruthenium hexamine (II) chloride, sodium azide, and palladium (Pd) catalyst (10 wt % on activated carbon) were purchased from Sigma Aldrich, St. Louis, MO. Tris (Hydroxymethyl) amino methane and magnesium chloride were obtained from J.T. Baker, Phillipsburg, NJ. 4-nitrophenyl phosphate disodium salt hexahydrate (Alfa Aeser, Wardhill, MA) was used to synthesize p-amino phenyl phosphate (PAPP). Dynabead® M-280 Streptavidin (Life Technologies, Grand Island, NY) were used to bind/conjugate biotinylated alkaline phosphatase enzyme (Vector Laboratories Inc., Burlingame, CA). Polystyrene latex microbeads (10 µm diameter, 2.5% wt. dispersion in water) were obtained from Alfa Aeser, Wardhill, MA. A 2 in. height × 2 in. diameter 0.56 T NdFeB permanent magnet was purchased from Amazing Magnets, Irvine, CA. Sylgard184 silicon elastomer base, Sylgard 184 silicon elastomer curing agent, and OS-30 solvent (Ellsworth Adhesives, Milwaukee, WI) were used to fabricate poly(dimethyl siloxane), PDMS gaskets.[19] Pre-cleaned microscope glass slides (1.5 × 1.0 × 0.1 in.^{3}) were purchased from VWR. All the chemicals and materials used to fabricate the electrode chips are described in our previous work.[7]

4.3.2 PAPP Synthesis.

p-amino phenyl phosphate was synthesized in house.[23, 24] Briefly, 300 g of 4-Nitrophenyl phosphate disodium salt hexahydrate, and 89.5 mg of Pd catalyst was dissolved in 75 mL of deionized water, and pH of the solution was adjusted to 6.5 by adding 6 M HCl. Solution was reduced under 1 atm. H_2 at room temperature for 2 h, followed by a filtration step to remove Pd catalyst. Clear filtrate solution was lyophilized under high vacuum (< 0.5 mm Hg) for 48 hours, and the remaining solid product was then characterized using 1H NMR (Bruker 300 MHz, D2O,): 6.51 (2H, doublet, J = 8.4 Hz), 6.70 (2H, doublet, J = 8.4 Hz) to check the quality of PAPP.

4.3.3 Tris and TTL Buffer Solution

Tris buffer was prepared with 0.1 M tris(hydroxymethyl)aminomethane, 1 mM magnesium chloride, and 0.02% sodium azide, and its pH was adjusted to 8.0 by adding 6 M HCl. All redox species solutions used herein were made in 0.1 M Tris buffer (pH 8.0) that was purged for > 20 min before using. Redox species solutions were kept under Ar for the experimental duration to minimize $[Ru(NH_3)_6]^{2+}$ oxidation. TTL buffer solution, used to wash the superparamagnetic beads, was prepared with 0.1 M Tris-HCl (pH = 8), 0.1 % Tween 20, and 1 M LiCl.

4.3.4 Experimental Set-Up

An electrical connection of electrode chip was made to a CHI 760B bipotentiostat (CHI Instruments, Austin, TX) with an edge connector (solder contact, 20/40 position, and 0.05 in. pitch) purchased from Sullins Electronics Corporation (San Marcos, CA). Cyclic voltammetry (CV) characterization of individual microelectrodes was performed using a procedure described in our previous work.[7] Flat flow profile studies that were used to optimize electrode

configuration and redox species concentration, were performed with a solution containing $Ru(NH_3)_6Cl_2$ and $Ru(NH_3)_6Cl_3$ in 0.1 M Tris buffer (pH= 9). 1 mL of this solution was mixed with 50 µL of polystyrene latex beads to facilitate the particle velocimetry imaging.[7, 20] 350 µL volume poured over the chip was contained by a PDMS gasket having a rectangular opening of 12.5 mm wide × 27.5 mm long × 840 high µm high. Chip assembly was covered with a microscope glass slide, thus making a closed electrochemical cell with its dimensions defined by the PDMS gasket. Whole assembly was then placed under a microscope (LEICA DM 2500M, NIKON) with a magnet underneath the chip, and the bead movement was recorded using SONY HDR-XR 500V camcorder connected to the microscope. See Figure 4. S3a. Velocity data were obtained by processing polystyrene latex bead movement videos with particle image velocimetry software (PIV), Dantec Dynamics.[7, 20] Data analysis started 5 s after the application of the potential step. For redox species concentration and flat flow configuration optimization experiments the solution concentrations of 5 mM and 10 mM, and electrode configurations of 2 and 3 working electrodes were used. See details in supporting information.

All the detection studies were performed at room temperature using the detection solution (5 mM $Ru(NH_3)_6Cl_2$, 5 mM $Ru(NH_3)_6Cl_3$, 10 mM PAPP in 0.1 M Tris buffer, pH 8). The AP derivitized superparamagnetic bead complex was made off the chip using the following procedure:

4.3.5 Magnetic Microbead Enzyme Complex Formation

A bead-enzyme complex was formed by reacting biotinylated AP with streptavidin coated superparamagnetic beads. In particular, following steps were performed to make the assay complex. (a) Superparamagnetic Bead Washing: 80 µL solution of streptavidin coated superparamagnetic beads was added to 100 µL TTL buffer in an eppendorf tube (VWR International), followed by a wash and decant step in the presence of NdFeB permanent magnet.

Thereafter, 100 µL volume of Tris buffer (pH = 8) was added and removed twice to wash the beads, followed by the addition of 20 µL Tris-HCl (pH=8) to suspend the superparamagnetic beads in it. (b) Dilution of Biotinylated Alkaline Phosphatase: 8 µL solution containing biotinylated AP was diluted with 12 µL Tris-HCl (pH=8) by a gentle shaking. (c.) Alkaline Phosphatase-Superparamagnetic Bead Complex Formation: both the solutions from step 1 and 2 were mixed together in an eppendorf tube under gentle vortex (Vortex Gene-2, Scientific Industries) for 15 minutes, to form the AP derivitized superparamagnetic bead complex. A 100 µL solution of Tris-HCl (pH=8) was added and removed three times to wash the unbound enzyme. The final remaining enzyme bead complex was suspended in total 40 µL volume of Tris-HCl.

A 5 µL solution of microbead-enzyme complex was used for a single experiment, and was poured using a micropipette on the chip that was placed over a 0.56 T NdFeB permanent magnet. Three different immobilization locations were chosen across 5.6 mm electrode set gap, with one lying directly on the horizontal path of detector, whereas other two were not. See Figure 4.1a. 350 µL of detection solution was poured on the chip using micropipette, and was also contained by the PDMS sidewalls with microscope glass slide on top. On-chip solution was allowed to react with AP for 60 s before applying a potential at selective electrodes. Reaction between AP and its electrochemical substrate PAPP generates the electroactive species of PAP_R. A constant applied potential of + 0.3 V was held at three microband electrodes shorted together from electrode set 3 which were used the pumping electrode; whereas all electrodes together from set 2 and set 1 were acting as the counter and reference, respectively. 160 µm radius disk electrode was used as the detector electrode at which square wave voltammetry was done (-0.3 V to + 0.5 V). Pumping electrodes moved the solution in the forward direction, and toward the

detector. The enzymatically generated PAP_R was oxidized at the detector along with $[Ru(NH_3)_6]^{2+}$ to generate an electrochemical current signal. See Figures 4.1b and 4.1c. In control experiments the pumping electrode was held at open circuit potential. For full experiments both the pumping and detector electrodes are on, however the enzyme assay complex is immobilized at different locations. See Figure 4.1a. In between the experiments, the chip was cleaned using deionized water and ultrapure argon gas, and a fresh volume of redox and enzyme assay complex solution was introduced.

4.4 Results and Discussion

The ability of the redox-MHD flat flow profile to perform multiplex assay was determined by detecting the enzymaticaly generated PAP_R (byproduct of the reaction between AP and its substrate solution, PAPP) at different locations on the chip. Superparamagnetic microbead enzyme complex was immobilized on the silicon chip at different locations using inherent presence of a permanent magnet in redox-MHD microfluidics; the reaction byproduct PAP_R was transported to the detector electrode using redox-MHD flat flow profile. Herein, the typical immunoassay is represented by the AP-biotin-streptavidin-superparamagnetic bead complex similar to an enzyme labeled 2˚ antibody-antigen-1˚antibody sandwich immunoassay. The enzyme assay is immobilized at a distant location from the detector, separating the detection and assay immobilization sites. This will also improve the device sensitivity by reserving the entire detector surface area for the electrochemical signal generation and avoiding the electrode surface insulation that often occurs by the immobilization of large biomolecules.

4.4.1 Enzyme Assay Detection

Control experiments without redox-MHD flat flow profile, but with square wave

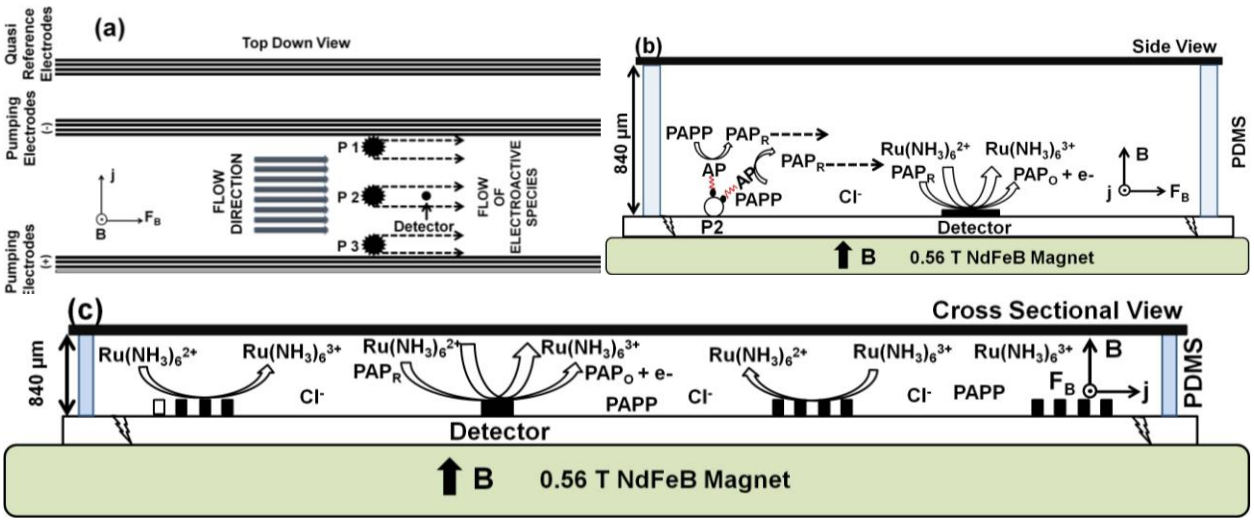

Figure 4.1 (a) Top-down view of fluid flow direction, and positions P1, P2, and P3 where magnetic microbeads containing the assay complex were immobilized using NdFeB magnet underneath the chip. There were other electrodes on the chip with different size concentric disks and rings, however for the sake of clarity those designs were omitted from the figure schematics. Due to the redox-MHD uniform flow velocity across the electrode set gap, enzymatically generated electroactive species at position P2 will reach the detector, but not from position P1 and P3 which continue moving forward without being detected.**(b)** Side view of the enzymatic conversion of PAPP to PAPR by AP derivitized superparamagnetic beads at position P2. Here a single bead represents a collection of beads, and is not to the scale. PAPR species are transported to detector electrode by redox-MHD pumping. **(c)** Cross-sectional view demonstrating electrochemical conversion and detection of different species at active electrodes.

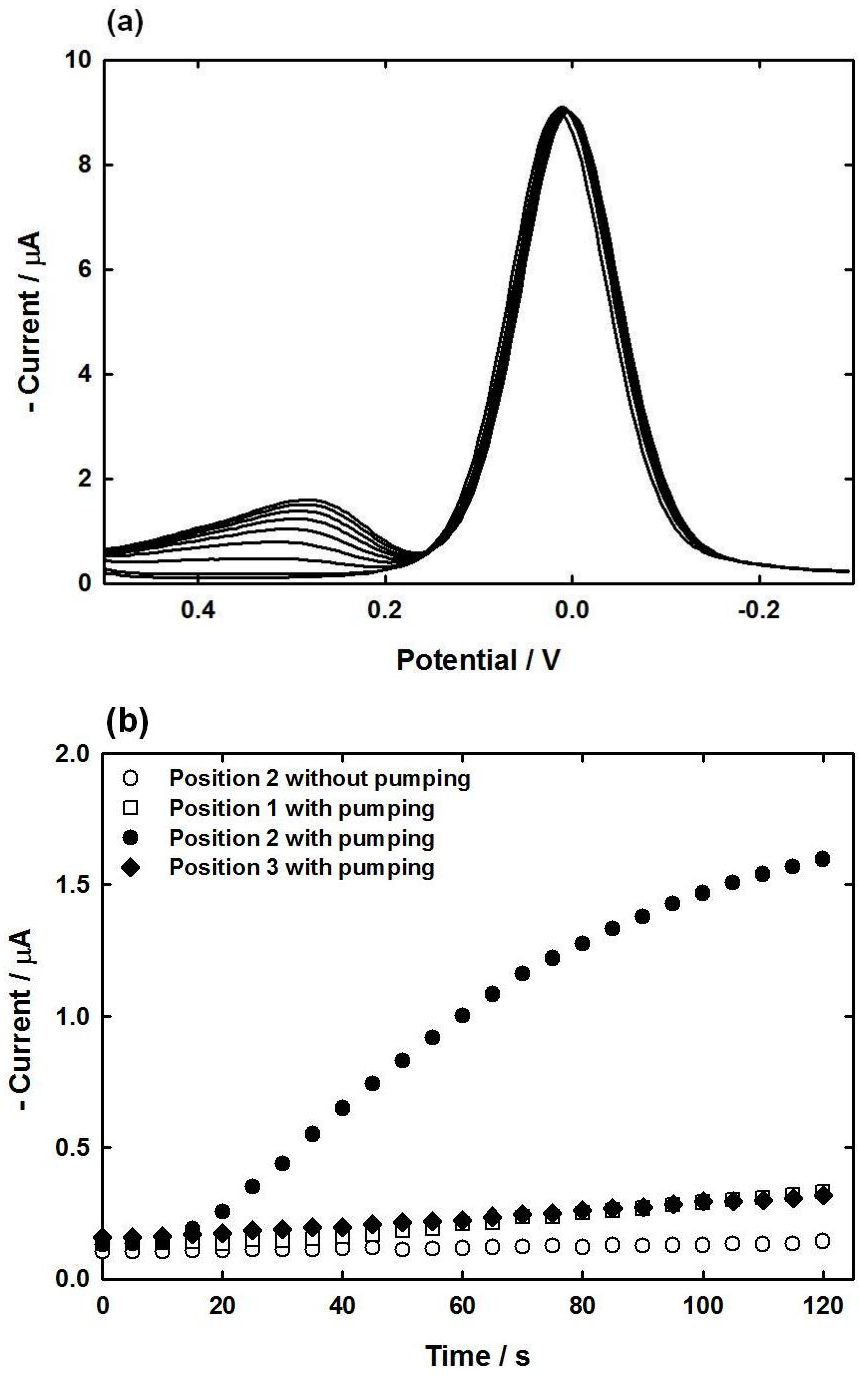

Figure 4.2 (a) SWV cycles show an increase in PAP_R current signal over time due to its continuous generation at assay site and arrival at detector. Square wave voltammogram presented in this figure were taken at every 15^{th} s, and the experiment was run for a total time of 125 s. **(b)** Plots of peak current with time from continuous square wave voltammogram at the detector electrode for different cases. Empty circles are the current data obtained from control experiments performed at position 2, with detector on, but without switching on the redox-MHD pumping.

voltammetry at the detector were performed. See Figure 4. S4. As soon as PAPP came in contact with AP, it was converted to PAP_R; since the pumping electrodes were inactive, even the presence of redox-MHD due to applied potential at the detector was unable to transport PAP_R to the detector. Therefore no electrochemical signal due to PAP_R oxidation was observed as shown in Figure 4. S4. A peak current corresponding to continuous oxidation of $[Ru(NH_3)_6]^{2+}$ was observed on the contrary that was present throughout the solution.

During the redox-MHD flat flow experiments, both the pumping and detector electrodes were on, and the microbead-enzyme complex was placed at three different locations on the electrode chip such that only one location faced the horizontal path of the detector, whereas other two were off that path by > 5 times the diameter of detector electrode (See Figure 4.1a). The reason for choosing other two locations was to differentiate between location dependent effects of flat flow profile. Due to a uniform velocity profile, the microbead-enzyme complex lying exactly on detector's horizontal path would have allowed undistorted PAP_R movement toward the detector. The undistorted movement of PAP_R from the other sites (position 1 and position 3) would carry the species along a path that was off the detector, and hence should not generate any signal at the detector. Data obtained from different experiments demonstrate a similar behavior. See Figures 4.2, 4. S5, and 4. S6. With assay complex at position 2, as soon as the electrodes were active, $[Ru(NH_3)_6]^{2+}$ oxidation started generating an electrochemical signal, but not yet from PAP_R oxidation. See Figure 4.2a. With time as PAP_R was transported toward the detector by redox-MHD pumping, its signal start to increase, and became visible at 20 s after the potential was applied, thereafter PAP_R oxidation signal continued to increase until end of the experiment. Linearity of increase was maximum until 60^{th} s, and thereafter it decreases. A possible reason for this behavior might be that during the initial incubation of PAPP with AP while the pumping was

turned off, a significant amount of PAP_R was generated; a significant amount of PAP_R therefore, arrived at the detector with the onset of the pumping. Coinciding with the onset of the pumping, the amount of PAPP reacting with AP and hence the generated amount of PAP_R was now limited which resulted in an eventual gradual decrease in the PAP_R oxidation signal. A maximum current of 1.6 µA was achieved at 120^{th} s. A comparison was made in Figure 4.2b with the PAP_R peak currents obtained from control experiment and experiments at positions 1 and 3. Data obtained clearly demonstrates an effect of the flat flow profile on PAP_R oxidation, thus validating the capability of flat flow profiles to perform multiplex detection. Least square fit analysis was also performed using data from individual plots in Figure 4.2b to statistically determine PAP_R arrival at the detector. When the device was under full operation i.e. both pumping and detector electrodes were on, and microbead-enzyme complex at position P2, best fit line was $y = 0.014$ (µA/s) $x + 0.077$ µA ($R^2 = 0.978$). A least square fit for control experiments, i.e. when pumping electrodes were off and only detector on, was $y = 0.0003$ (µA/s) $x + 0.1011$ µA ($R^2 = 0.9364$) with a peak current that was 8 % of the maximum peak current from full operation. For other experiments with device under full operation, but the microbead-enzyme complex immobilized at position 1 and 3, the best fit lines were, $y = 0.0018$ (µA/s) $x + 0.1075$ µA ($R^2 = 0.965$) and $y = 0.0014$ (µA/s) $x + 0.1478$ µA ($R^2 = 0.995$), respectively. Peak currents for position 1 and 3 had also dropped to 21 % and 20 %, respectively, of the corresponding peak current values from full operation at position 2. A comparison between slopes from different plots had also revealed that their values for control, position 1, and position 3 dropped to 2, 13, and 10%, respectively to that of the slope from position 2 under full operation. A drop in the slope reflects the rate at which the detector current increases with time, and therefore statistically confirms the preferential effects of redox-MHD flat flow profile at position 2 compared with the other experiments.

4.5 Conclusions

A proof-of-concept study toward the development of multiple, parallel chemical analysis on a silicon chip was performed using redox-MHD pumping . This was accomplished using two advantages of redox-MHD, the flat flow profile and the inherent presence of NdFeB permanent magnet to immobilize magnetic microbead-enzyme complex. Flat flow profile was generated using $[Ru(NH_3)_6]^{3+/2+}$ in Tris buffer, and the magnetic microbead-enzyme complex was formed by reacting biotinylated AP with streptavidin coated superparamagnetic beads. Superparamagnetic beads based enzyme assay complex was immobilized at different locations in the presence of NdFeB magnet. This option has further given the flexibility in enzyme assay complex placement on the chip, thus simplifying the critical immobilization step in standard immunoassays. A reaction between AP and its electrochemical substrate PAPP (that was present in the pumping solution) generates the electroactive species of PAP_R that gives the electrochemical signal at the detector electrode. Selective placement of enzyme assay complex at different locations has generated a strong current signal at the location that is in the horizontal path of the detector. Whereas at other locations that are off the detector path, current signal is insignificant, thus confirming the potential of redox-MHD flat flow profile to perform multiplex assay detection with the modified device design.

4.6 Acknowledgements

We are thankful to the National Science Foundation (Grant number: CHE-0719097), and the Arkansas Biosciences Institute, the major research component of the Arkansas Tobacco Settlement Proceeds Act of 2000, for their financial support.

4.7 Supporting Information

Supporting information includes PDMS location schematics relative to the electrode position, experimental set-up for flat flow profile and its accomplishment using new redox species that are compatible with assay detection, schematics that visualize the positions for enzyme assay complex placement and their anticipated effects on the detection signal, schematics which show the expected results for position 1, 3, and control experiments, and their experimentally determined square wave voltammogram.

4.8 References

1. E. M. Elnifro, A. M. Ashshi, R. J. Cooper and P. E. Klapper, *Clinical Microbiology Reviews*, 2000, **13**, 559-570.

2. E. R. Goldman, A. R. Clapp, G. P. Anderson, H. T. Uyeda, J. M. Mauro, I. L. Medintz and H. Mattoussi, *Analytical Chemistry*, 2004, **76**, 684-688.

3. H. Keshishian, T. Addona, M. Burgess, E. Kuhn and S. A. Carr, *Molecular & Cellular Proteomics*, 2007, **6**, 2212-2229.

4. J. A. M. Vet, A. R. Majithia, S. A. E. Marras, S. Tyagi, S. Dube, B. J. Poiesz and F. R. Kramer, *Proceedings of the National Academy of Sciences of the United States of America*, 1999, **96**, 6394-6399.

5. G. F. Zheng, F. Patolsky, Y. Cui, W. U. Wang and C. M. Lieber, *Nature Biotechnology*, 2005, **23**, 1294-1301.

6. G. M. Whitesides and A. D. Stroock, *Physics Today*, 2001, **54**, 42-48.

7. V. Sahore and I. Fritsch, *Analytical Chemsitry*, Submitted July 2013.

8. M. Z. Bazant and Y. X. Ben, *Lab on a Chip*, 2006, **6**, 1455-1461.

9. S. Y. Yang, K. Y. Lien, K. J. Huang, H. Y. Lei and G. B. Lee, *Biosensors & Bioelectronics*, 2008, **24**, 855-862.

10. V. Sivagnanam, B. Song, C. Vandevyver and M. A. M. Gijs, *Analytical Chemistry*, 2009, **81**, 6509-6515.

11. R. S. Sista, A. E. Eckhardt, V. Srinivasan, M. G. Pollack, S. Palanki and V. K. Pamula, *Lab on a Chip*, 2008, **8**, 2188-2196.

12. M. A. M. Gijs, *Microfluidics and Nanofluidics*, 2004, **1**, 22-40.

13. S. Qian and H. H. Bau, *Mechanics Research Communications*, 2009, **36**, 10-21.

14. N. Leventis and X. R. Gao, *Analytical Chemistry*, 2001, **73**, 3981-3992.

15. K. M. Grant, J. W. Hemmert and H. S. White, *Journal of the American Chemical Society*, 2002, **124**, 462-467.

16. H. J. Kang and B. Choi, *Sensors and Actuators a-Physical*, 2011, **165**, 439-445.

17. N. Pamme, *Lab on a Chip*, 2006, **6**, 24-38.

18. M. C. Weston, M. D. Gerner and I. Fritsch, *Anal Chem*, 2010, **82**, 3411-3418.

19. E. C. Anderson, M. C. Weston and I. Fritsch, *Analytical Chemistry*, 2010, **82**, 2643-2651.

20. P. G. Scrape, M. D. Gerner, M. C. Weston and I. Fritsch, *Journal of the Electrochemical Society*, 2013, **160**, H338-H343.

21. M. C. Weston, C. K. Nash and I. Fritsch, *Analytical Chemistry*, 2010, **82**, 7068-7072.

22. M. C. Weston and I. Fritsch, *Sensors and Actuators B-Chemical*, 2012, **173**, 935-944.

23. M. C. Weston, C. K. Nash and I. Fritsch, *Anal Chem*, 2010, **82**, 7068-7072.

24. L. H. Deriemer and C. F. Meares, *Biochemistry*, 1981, **20**, 1606-1612.

4.S Supporting Information: Redox-Magnetohydrodynamics (MHD) Flat Flow Profile Guided Enzyme Assay Detection: Toward multiple, parallel analyses

Supporting information includes the electrode chip design, PDMS location schematics relative to the electrode position, experimental setup for redox-magnetohydrodynamics (MHD) experiments, and the accomplishment of flat flow profile using new redox species that are compatible with the assay detection, experiments showing nature of flat flow profile in the presence of superparamagnetic beads, schematics that show the expected results for positions 1, 3, and control experiments, and their experimentally determined square wave voltammograms.

4.S1 Electrode Chip Design

A 2.0 in. (length) × 1.0 in. (width) chip has multiple design features, that includes three sets of gold rectangular microband electrodes, each set having four individually addressable electrodes of same size, and different sizes of concentric disk and ring microelectrodes. See Figure 4.S1(a). Radial dimensions of concentric disk-ring electrodes were: disk radius: 16., 38., 79., and 156. µm; inner ring radius: 200., 400., 800., and 1600. µm; outer ring radius: 250., 500., 1000., and 2000. µm, respectively, and an expanded view for one such electrode set is given in Figure 4.S1(b). Individual microband electrodes were ~100 nm thick, 100. µm wide, and 2.50 cm long (See Figure 4.S1(c)). All electrode dimensions were measured using optical microscopy, whereas the thickness was measured with an uncalibrated piezoelectric monitor attachment on the thermal evaporator (Edwards Auto 6 Evaporator). A detailed fabrication procedure for the electrode chips was described previously.[1]

4.S2 Optimizing redox species concentrations and the selection of a Suitable flat flow profile electrode configuration

Redox pumping species were selected based upon the previous work in our laboratory, where it was shown that the ruthenium hexamine ($[Ru(NH_3)_6]^{3+/2+}$) is compatible with *p*-amino phenol (PAP_R) detection, although redox species presence deteriorate the limit of detection.[2] The optimum solution concentration and optimum electrode configuration for achieving the redox-magnetohydrodynamics (MHD) flat flow profile were determined in a separate set of experiments using $[Ru(NH_3)_6]^{3+/2+}$ in Tris buffer solution and polystyrene latex beads only, and a 0.56 T NdFeB permanent magnet underneath the chip. There was no *p*-amino phenyl phosphate (PAPP) in the solution and no bead-assay complex was placed on the chip. The flow data were

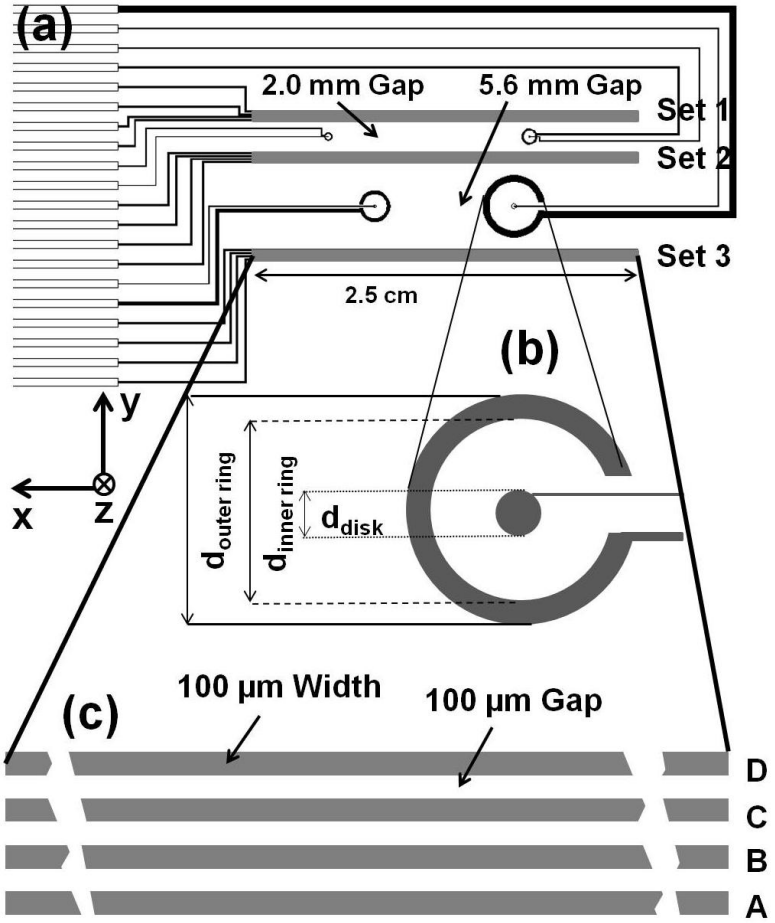

Figure 4.S1 (a) Top down view of electrode chip. An individual chip has three electrode sets ("set 1", "set 2", and "set 3") with each having four individually-addressable microband electrodes (A, B, C, D) of equal size (25.0 mm long × 98 ± 0.1 µm wide × ~100 nm thick). Concentric disk-ring microelectrodes of different sizes are also present on the same chip, but only the disk with radius 160 µm was used as the detector in this study. Intraset electrode gaps are 100 µm, whereas the interset gaps are 2.0 (between sets 1 and 2) and 5.6 mm (between sets 2 and 3). (b) Expanded view of concentric disk-ring electrode set 4. (c) Expanded view of microband electrode set 3.

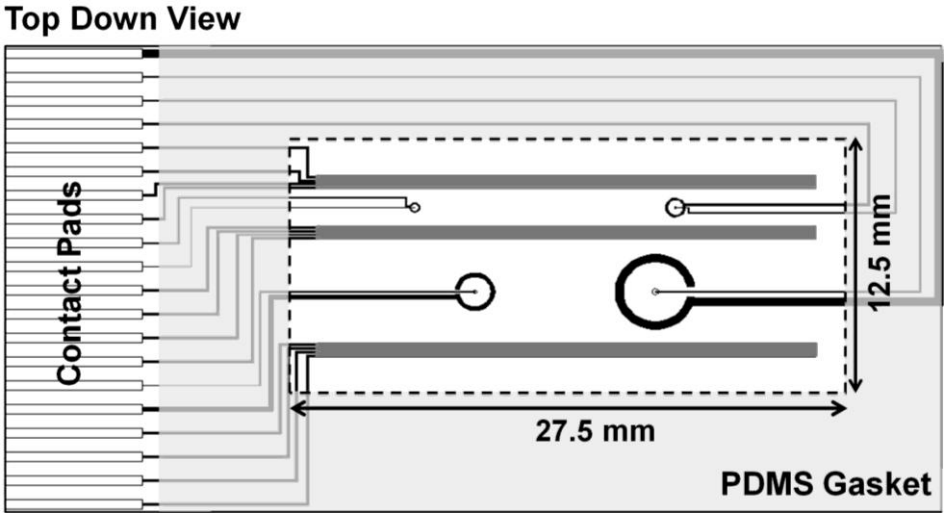

Figure 4.S2 Top-down view for the PDMS gasket schematics (light gray) relative to the electrode positions. Rectangular opening (12.5 mm wide × 27.5 mm long) of the PDMS is outlined by the dashed lines, and height (840. µm) is not shown in the figure. There were three sets of microband electrodes (gray color) with each having four rectangular microelectrodes of equal size. Each electrode chip also has four different sets of concentric ring-disk microelectrodes represented by black colors. Black lines connecting the electrodes with the contact pads indicate the benzocyclobutene (BCB)-insulated leads. A microscope slide placed on top (not shown) served as a lid and the PDMS sidewalls contained the redox species solution that was dispensed onto the chip within the open region of the PDMS.

processed 5 s after the application of the potential at a height of 300 μm above the electrode chip surface; whereas the total experimental duration was 120 s. The poly dimethyl siloxane (PDMS) location with respect to the electrodes is shown in schematics that are drawn to-scale in Figure 4.S2. Two concentrations of 5 and 10 mM (this is the total concentration that includes both forms of the redox species), applied potentials of +0.2 and +0.3 V, and an electrode configuration with two and three innermost working electrodes from Set 3 (see Figure 4.S1) were chosen. All the microband electrodes shorted together from set 1 and set 2 worked as reference and counter electrode, respectively. Results obtained are given in Figure 4.S3, and a maximum fluid velocity of 38 μm/s was measured for the 10 mM concentration and using three working electrode. This was sufficient to observe the flat flow profile effects on the assay detection signal. In a different experiment, a four working electrode configuration was used, however this has consistently lead to degradation of the counter electrodes for multiple chips. This is likely due to the inability of the counter electrodes to support the current at the working electrodes without shifting to very large potentials that cause electrode oxidation. Therefore three bands were combined to serve as the working electrode to avoid electrode corrosion, ensure electrode quality, and increase the electrode chip life time.

4.S3 Flat Flow in the Presence of Superparamagnetic Beads

Redox-MHD experiments were performed in the presence of superparamagnetic beads immobilized at the 160 μm diameter disk electrode. A redox species solution containing 12.5 mM of ruthenium hexamine (II) chloride [$Ru(NH_3)Cl_2$], 12.5 mM of ruthenium hexamine (III) chloride [$Ru(NH_3)Cl_3$] in 0.1 M Tris buffer (pH = 9.2) was used in this work. A four electrode configuration with all microband electrodes from set 3 shorted together as working, and the

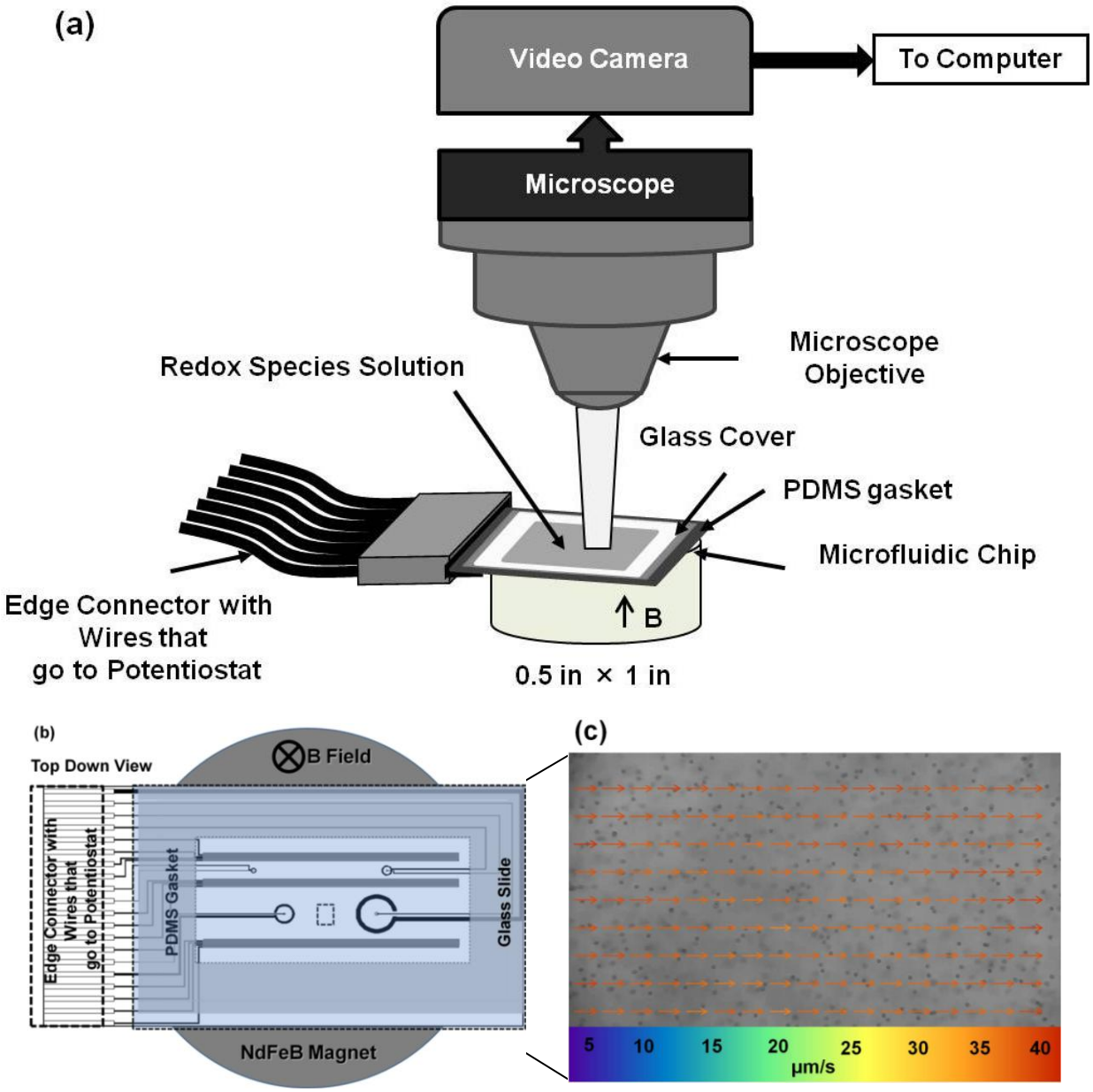

Figure 4.S3 Particle image velocimetry (PIV) processed flat flow profile imaging and experimental setup. **(a)** Experimental setup used for the experiment. The recorded microbead movement in a solution containing 5 mM of ruthenium hexamine (II) chloride [$Ru(NH_3)_6Cl_2$], 5 mM of ruthenium hexamine (III) chloride [$Ru(NH_3)_6Cl_3$] in 0.1 M Tris buffer, polystyrene latex beads (2.5 % wt dispersion in water), and in the presence of a 0.56 T NdFeB permanent magnet, was analyzed using particle image velocimetry (PIV) software. **(b)** Top-down view of the setup, and also the small region over which the PIV image is presented. **(c)** Representative PIV image of a small region near the center of the 5.6 mm interset electrode gap. The direction and magnitude of the microbead velocity confirms the uniformity of fluid flow within the interset electrode gap.

corresponding electrodes from set 2 shorted together as the counter/reference, was used. Redox-MHD convection was generated by a 0.56 T NdFeB magnet underneath the chip, and by applying a 120 μA current across the active electrodes. Fluid velocity was measured at a height of 245 μm above the chip surface. Although the field of view over the disk electrode was obscured by the presence of magnetic beads, the fluid still flows in a straight line path by visualizing the flow adjacent to those locations and is evident in Figures 4.S4 (b), (c), and (d). Therefore, the concept of a flat flow profile is still valid in the presence of the superparamagnetic beads.

4.S4 Enzyme assay detection control experiments

Control experiments were performed by immobilizing the bead-assay complex at position 2 in the presence of a magnet underneath the chip, however the redox-MHD pumping between band electrodes was intentionally turned off. In this case all the microbands from set 1 and set 2 served as the reference and counter electrodes, respectively, whereas the disk 4 electrode was the only working electrode under a varying potential. Figure 4.S5(a) shows the basic mechanism for the control experiments, here the PAP_R is generated as soon as PAPP from solution reaches the alkaline phosphatase (AP). However, due to the absence of pumping the generated electroactive species were not able to reach the detector electrode. Therefore electrochemical signal at the detector was only due to the oxidation of $[Ru(NH_3)_6^{2+}]$. Overlays of square wave voltammograms taken continuously reflect a similar behavior (see Figure 4.S5(b)), where a PAP_R oxidation signal at the detector is absent. It may also be noted that due to a varying potential at the disk electrode in the presence of NdFeB magnet, the redox-MHD phenomenon still occurs. However, the absence of PAP_R signal clearly suggests that diffusion on the time scale of this experiment is insufficient to carry the PAP_R species to the detector electrode.

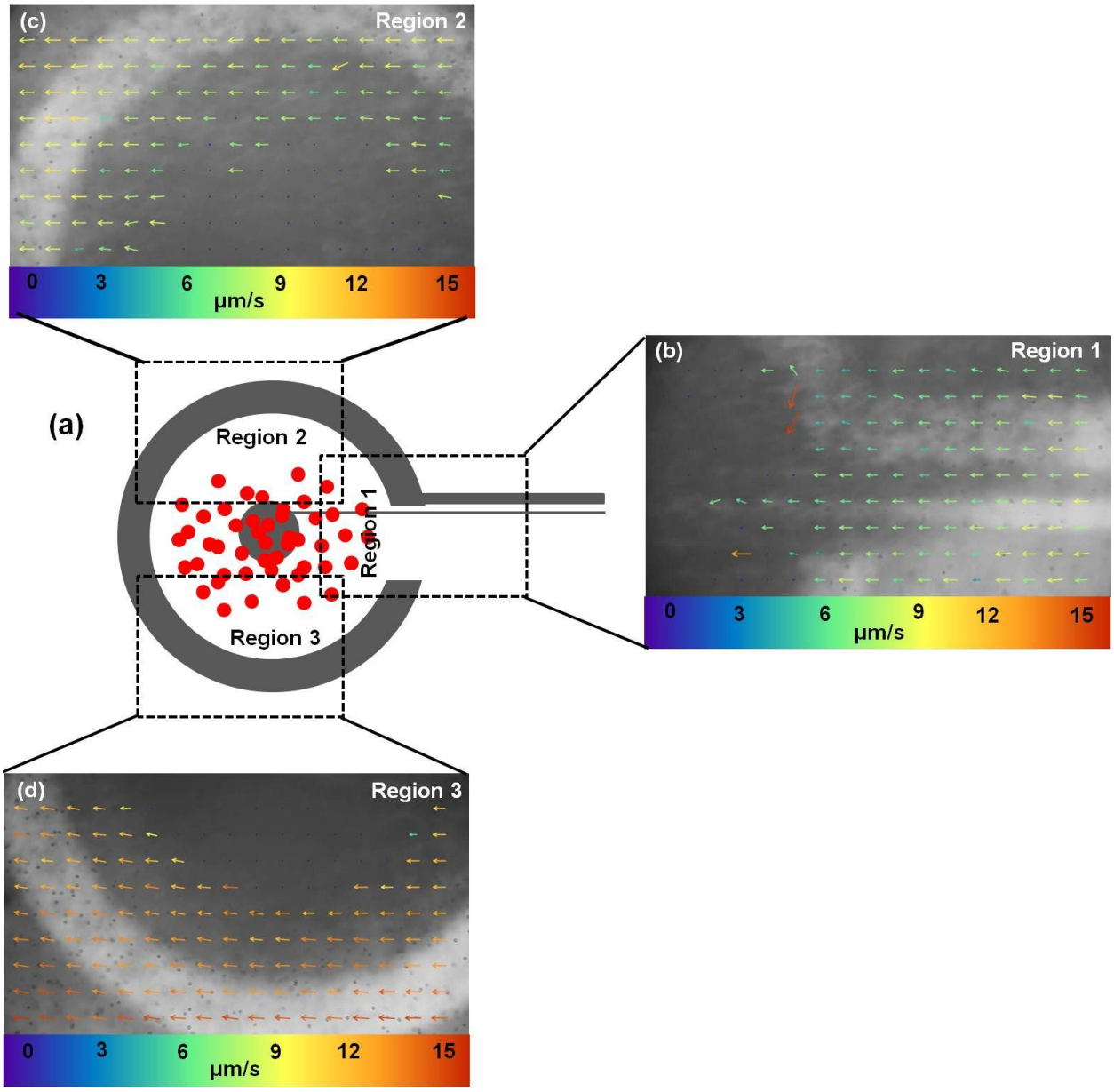

Figure 4.S4 Redox-MHD fluid flow in the presence of superparamagnetic beads. **(a)** Schematic shows the superparamagnetic bead placement (red dots) and the relative rectangular regions for which the expanded view of PIV processed flow velocities are shown in **(b)**, **(c)**, and **(d)**. The field of view for video microscopy was obscured around the disk electrode due to the presence of the superparamagnetic beads which produce a dark background, making it impossible to see the polystyrene latex microbeads (also dark) that were used for tracking fluid flow; therefore the PIV software analysis did not generate velocity vectors over those locations.

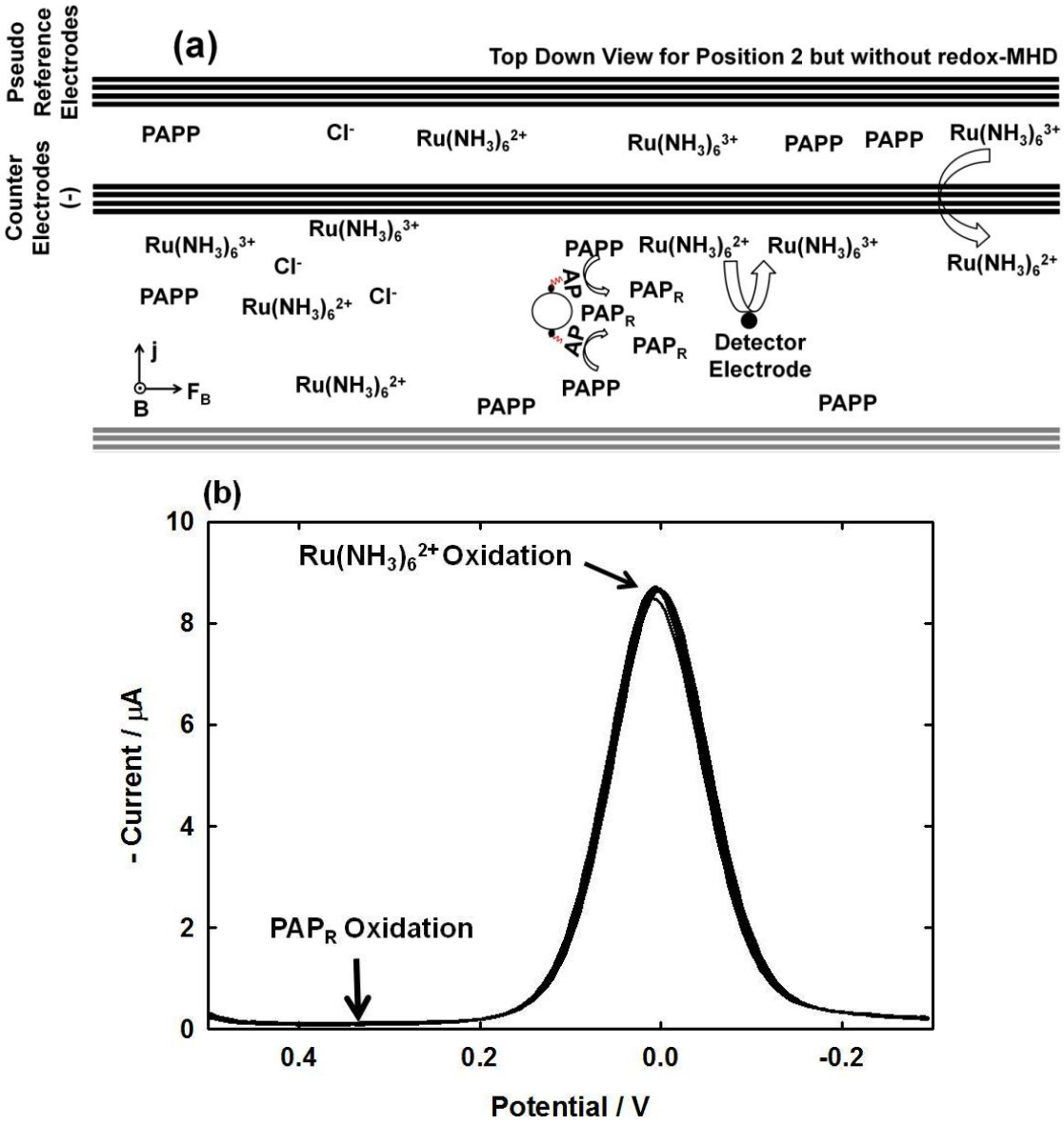

Figure 4.S5 (a) Figure depicts the basic mechanism for control experiments when the magnetic microbead complex was immobilized at position 2. Control experiments were performed with a magnet underneath the chip; however the band electrodes were left at open circuit (pumping was intentionally turned off). As soon as the solution containing PAPP reaches the AP, it converts to PAP_R. With increasing time PAP_R can only reach the detector through natural diffusion, which is very slow. Therefore the detector signal should only be due to oxidation of $[Ru(NH_3)_6^{2+}]$ which is present everywhere in the solution. **(b)** Overlay of square wave voltammograms taken continuously reflect this behavior where a PAP_R oxidation signal is absent, but showing a large $[Ru(NH_3)_6^{2+}]$ signal. Black colored electrodes were all active, whereas the grey colored were inactive.

Therefore the PAP_R oxidation signal observed in Figure 4.2(a) of the main document was only due to delivery via redox-MHD flat flow.

4.S5 Enzyme assay detection at Positions lying off the horizontal path to the detector

To further validate the possibility of multiplex detection using redox-MHD for microfluidic transport, the bead-enzyme complexes were immobilized at positions 1 and 3, lying off the horizontal path to the detector. Expected behavior for this setup is shown in Figures 4.S6(a) and 4.S7(a), respectively. Due to the existence of a uniform flow profile, the enzymatically generated electroactive species PAP_R was transported parallel to the detector without being detected. Hence the only electrochemical signal generated at the detector is due to the oxidation of $[Ru(NH_3)_6^{2+}]$, which is present throughout the solution. See Figures 4.S6(b) and 4.S7(b). Unlike the control experiments in the absence of pumping, the PAP_R oxidation signal is visible above the background in the presence of pumping for positions 1 and 3. Because of the manipulation of bead placement by hand, there is a chance that a few of the beads scatter into other paths. Therefore when the scattered beads that are in line with the detector come into contact with PAPP, they generate PAP_R , which oxidizes at the detector to generate a current signal that is above the background.

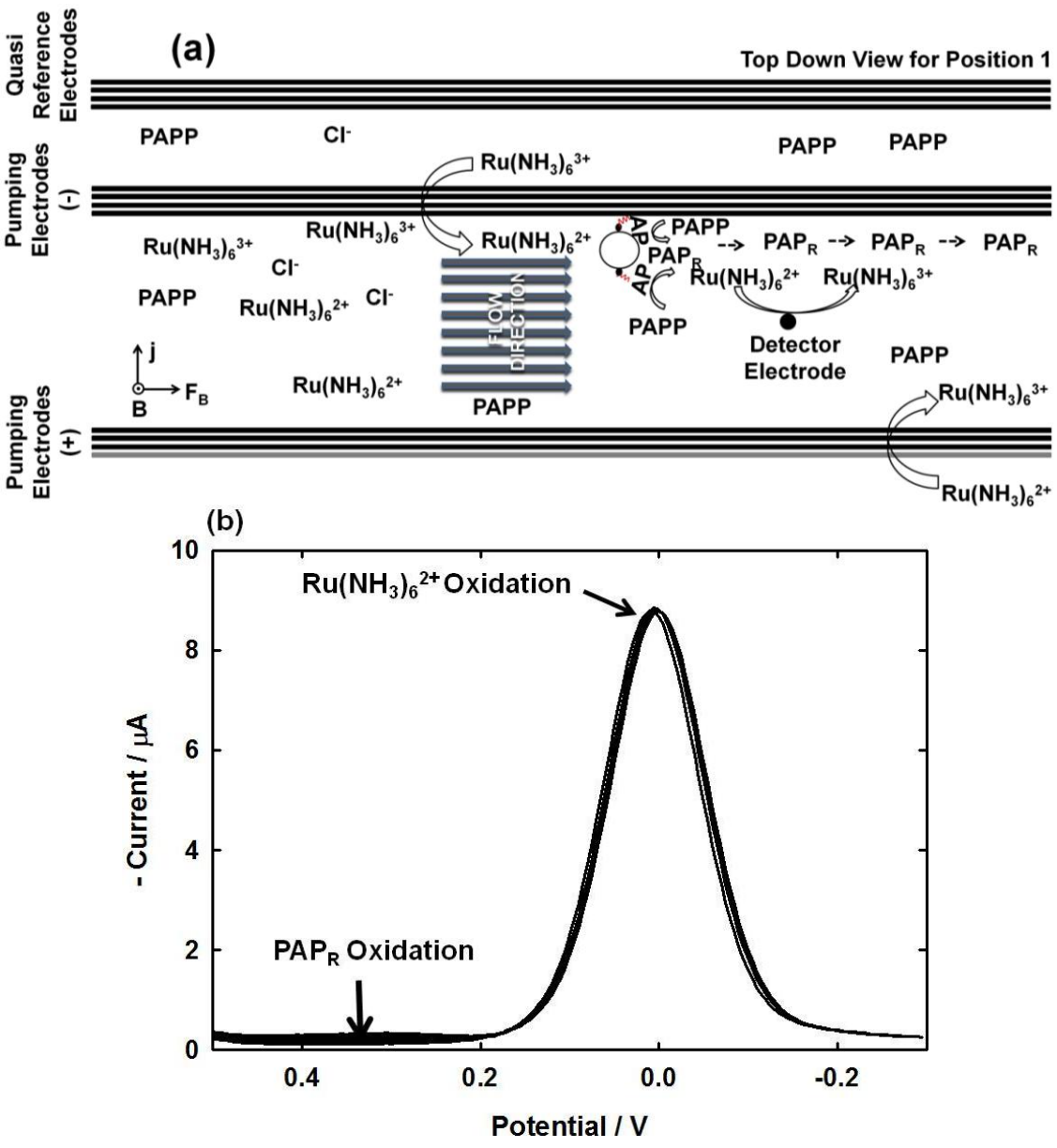

Figure 4.S6 (a) Figure shows the basic mechanism for another control experiment, when the enzyme assay complex is placed at position 1 (with a magnet underneath the chip), and the assay detection is under full operation. As soon as the solution containing PAPP reaches the AP, it converts to PAP_R, however with increasing time as the redox-MHD pumping continues, the PAP_R is transported in a straight path, without coming in contact with the detector. Therefore, the detector signal should be only due to the oxidation of $[Ru(NH_3)_6^{2+}]$ which is present everywhere in the solution. **(b)** Overlay of square wave voltammograms taken continuously reflects this behavior with a PAP_R oxidation signal that is almost indistinguishable from the background and a large $[Ru(NH_3)_6^{2+}]$ signal. Black colored electrodes were all active, whereas the grey colored were inactive.

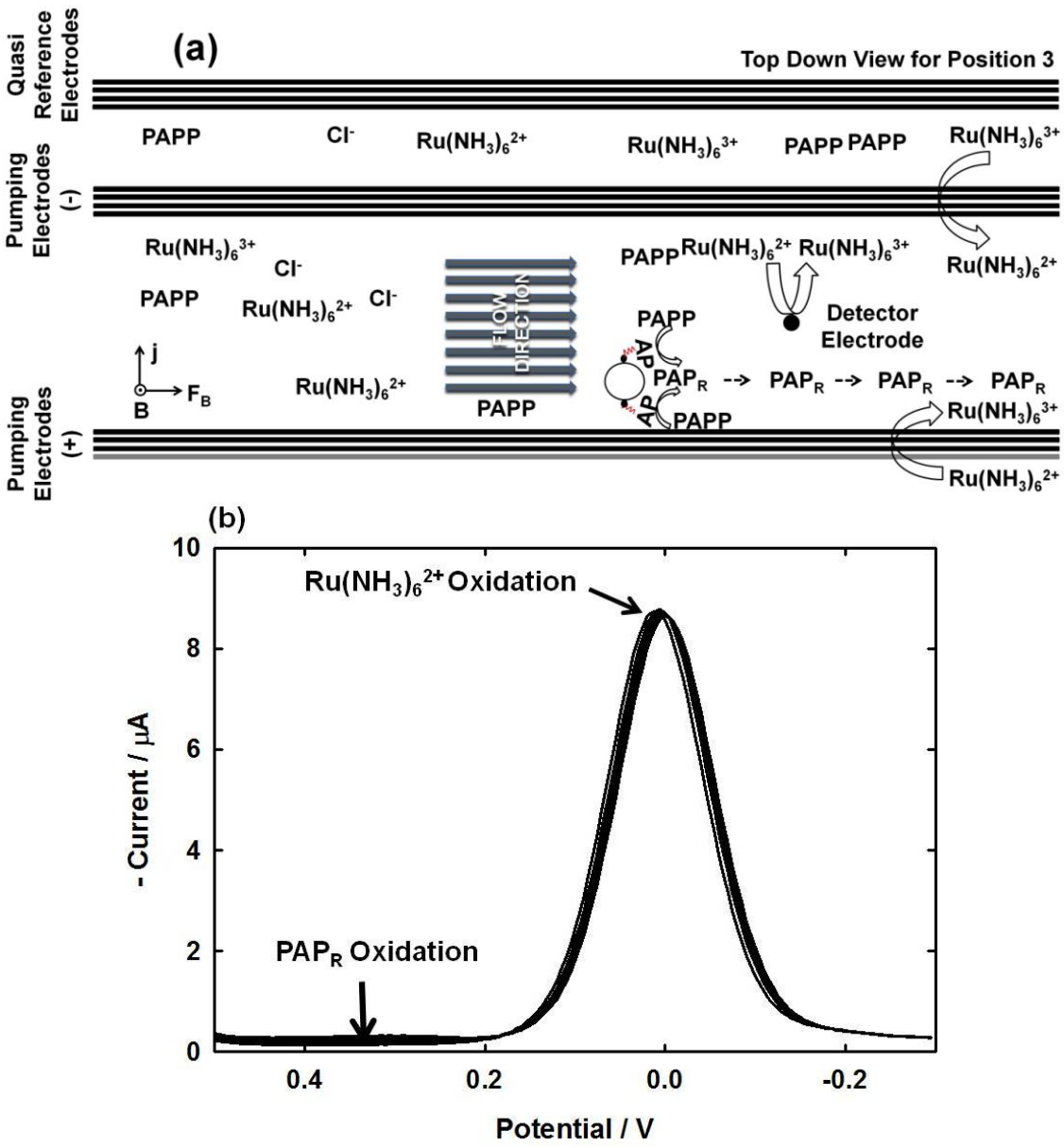

Figure 4.S7 (a) Figure shows a similar basic mechanism as given in S-4 a, however the enzyme assay complex is placed at position 3 (with a magnet underneath the chip), and the assay detection was under full operation. As soon redox-MHD pumping is on, the PAP_R is transported in a straight path, but does not reach the detector, Therefore, the detector signal should only be due to the oxidation of $[Ru(NH_3)_6^{2+}]$ which is present everywhere in the solution. **(b)** Overlay of square wave voltammograms taken continuously reflects this behavior with a PAP_R oxidation signal that is almost indistinguishable from the background and a strong $[Ru(NH_3)_6^{2+}]$ signal. Black colored electrodes were all active, whereas the grey colored were inactive.

4. S6 References

(1) Anderson, E. C.; Weston, M. C.; Fritsch, I. *Analytical Chemistry* **2010**, *82*. 2643-2651.

(2) Weston, M. C.; Nash, C. K.; Fritsch, I. *Analytical Chemistry* **2010**, *82*. 7068-7072.

5. Electrochemically Generated Density Gradient-Induced Natural Convection in Microfluidic Systems

The following chapter was formatted with an intention to publish in a peer reviewed journal. Work in this chapter was motivated by the new outcomes from redox-magnetohydrodynamics (MHD) experiments where the effects of natural convection were observed over time. To thoroughly understand the natural convection in microfluidic systems two different studies were performed. The work using concentric disk-ring microelectrodes is presented here. Natural convection is also under investigation in our laboratory using microband electrodes.

5.1 Abstract

Natural convection induced by electrochemically generated density gradients was studied in a static, confined, and small volume (12.5 mm wide × 27.5 mm long × 840. μm high) containing $K_3Fe(CN)_6$ and $K_4Fe(CN)_6$ in KCl electrolyte. A chip having variety of concentric disk (radius: 20-160 μm), and ring (inner radius: 200-1600 μm, outer radius: 250-2000 μm, respectively) gold microelectrodes was fabricated on an insulated silicon substrate. The effects on fluid convection were observed in the region between the disk and ring electrodes, as a function of their size and relative bias (anode and cathode), concentration of redox species under potential control (+0.4 V in a two electrode configuration, and 5, 10, 50 and 100 mM each of the reduced and oxidized forms), and magnitude of applied current (0.27, 0.81, 1.35, and 1.89 μA corresponding to 10, 30, 50 and 70% of the mass transfer limited value, respectively). Video microscopy was used to monitor the fluid movement by tracking 10 μm polystyrene latex beads added to the solution, and the data were processed using particle image velocimetry (PIV) software. A delayed onset in natural convection was confirmed by the output signals of the applied potential and current experiments. Natural convection increased with electrode size for both anodes and cathodes, and most noticeable at onset time of 20 s for the largest disk investigated here of 160 μm radius when serving as an anode at +0.4 V vs. the on-chip quasireference electrode in a solution of 100 mM. A maximum fluid velocity of ~10 μm/s, directed toward the disk near the electrode chip was observed under these conditions, with the flow switching direction at the top of the cell, producing a net vertical circular movement.

5.2 Introduction

This chapter quantifies the effects of natural convection induced by electrochemically-generated density gradients in a small volume system containing an initially static solution of redox species and where the Reynolds number is less than unity. Electrochemical reactions at the electrode-solution interface and their associated counter ion movement in the electrode vicinity leads to a density mismatch with respect to the bulk solution, thus generating the fluid's natural convection due to the onset of buoyant forces. Here, the effects of natural convection were measured by the sudden changes in electrode current, potential, and localized fluid velocity. Understanding electrochemically-initiated natural convection in small, confined volumes is important to account for the mass transfer at microelectrodes, to explain the analytical results involving limiting currents, to implement new mixing approaches of two fluids in microfluidic systems, and to decipher the uniformity of electrodeposited films.

Electrochemistry is a commonly used analytical technique, an integral part of energy conversion and storage devices (e.g. batteries, fuel cells, photochemical conversion, and electrochemical double layer capacitors), and central to electroplating. Electrochemical processes are governed by the electron-transfer reactions taking place at the electrode-solution interface. The rate can be limited by the electron transfer kinetics or by mass transfer. Three common modes of mass transfer are diffusion, migration, and convection. Diffusion is random Brownian motion and causes a net mass transfer in the opposite direction of the concentration gradient. Migration can be imposed in the presence of an electrostatic potential gradient. Convection, which can be either forced or natural, appears because of the local changes in solution hydrodynamics. In a static solution, the migrational flux of ionic species can be suppressed using excess supporting electrolyte, thus arguably leaving diffusion as the primary mode of mass

transfer.[1,2] However for a reversible electrochemical system the localized density gradients in solution at the electrode-solution interface with respect to the bulk solution induce a force due to buoyancy. Less dense volume elements rise, more dense volume elements sink, hence leading to mass transfer by natural convection,[3,4] which further affects the concentration distribution near the electrode–solution interface, and thus may cause the electrode current or potential to change differently than would be expected by diffusion alone.

Microelectrodes have significant advantages compared to their macro counterparts, such as the increased rates of mass transfer, rapid attainment of a steady state, and enhancement of signal-to-noise ratio.[5] At microelectrodes the natural convection is typically considered insignificant due to its screening by overwhelming diffusional fluxes.[3] However multiple studies have shown otherwise, and the effects of natural convection have been observed on electrolytic processes and concentration profiles of electroactive species around the electrode surface.[6,7] Researchers have also quantified its effects on electroanalytical and spectroscopic data for microelectrodes.[8,9,10,11,12] Simulations have been performed to better understand this phenomenon.[13,14,15] The effects of natural convection have also been noticed in redox-magnetohydrodynamics (MHD) microfluidic systems,[16,17,18,19,20] Experimental and theoretical studies have been performed to measure the concentration and velocity profiles for the electrochemical systems under natural convection conditions; however the electrode dimensions were in the mm to cm scales.[21,22]

To fully understand natural convection in chip-based microfluidic and other confined volume systems containing microelectrodes, a detailed study is needed that investigates not only the changes in current and potential but also tracks fluid motion. We accomplished that goal as described here in this work, where microbead-based video microscopy in a confined microfluidic

system allowed the monitoring of localized flow patterns resulting from electrochemically-generated natural convection between concentric disk and ring microelectrodes on a chip. Electrochemistry of ferri-/ferrocyanide and the associated counterion movement induced density gradients in an electrolyte of potassium chloride confined in a small volume over the microelectrodes led to the natural convection. The effects of natural convection on current, potential, and fluid velocity were determined as a function of electrode size, electrode polarity, applied current, and concentration of redox species.

5.3 Experimental Section

5.3.1 Chemicals and Materials

All chemicals were reagent grade and used as received. Aqueous solutions were prepared using high purity deionized water obtained from Ricca chemical company, Arlington, TX. Potassium chloride in powder form was purchased from EMD™, USA. Potassium ferricyanide ($K_3Fe(CN)_6$) and potassium ferrocyanide ($K_4Fe(CN)_6$) were purchased from EM Science, Gibbstown, NJ and J.T.Baker, Phillipsburg, NJ, respectively. Polystyrene latex microbeads (10 μm diameter, 2.5 % wt. dispersion in water) were purchased from Alfa Aeser, Wardhill, MA. Silicon (100) wafers (125 mm diameter, 650 μm thickness, 2 μm thermally grown silicon dioxide) used as the substrate material for electrode chips, were purchased from Silicon Quest International, Santa Clara, CA. Chromium and gold layers were deposited on the silicon wafers using chromium deposited tungsten rods (Kurt J. Leskar Company, Clairton, PA) and the small pieces of gold (Canadian Maple Leaf, 99.99 %) placed in a molybdenum boat (Kurt J. Leskar Company, Pittsburg, PA). The pattern transfer from photo plot masks (Advance Reproductions Corporation, North Andover, MA) to the wafer was made by using a positive photoresist (AZ 4330), and the tetramethyl ammonium hydroxide (TMAH) was used as the developer solution

for the 1st photolithography. Gold (Transene, GE8148) and chromium etchant (HTA enterprise, CEP200) were used as received during the electrode chip fabrication. Negative photoresist, benzocyclobutene, BCB (Cyclotene, 4024-40) was purchased from Dow Chemical Company and was used on the chip as an insulating material. Sylgard184 silicon elastomer base, Sylgard 184 silicon elastomer curing agent and OS-30 solvent (Ellsworth Adhesives, Milwaukee, WI) were used to made the poly(dimethyl siloxane), PDMS.[16] Pre-cleaned microscope glass slides (1.5 × 1 × 0.1 in^3) were obtained from VWR.

5.3.2 Electrode Chip Design

Each 2 in (length) × 1 in (width) chip contains multiple designs, but only the four sets of ring and disk microelectrodes were used. As shown in Figure 5.1a and 5.1b, sets I, II, III, and IV consist of disks with radii of 20, 40, 80, and 160 μm, respectively, which are centered inside rings having inner radii of 200, 400, 800, and 1600 μm and outer radii of 250, 500, 1000, and 2000 μm, respectively. The Appendix provides details of the microfabrication procedure, which was based on a procedure published previously.[23]

5.3.3 Experimental Set Up

An edge connector (solder contact, 20/40 position, 0.05 in pitch) purchased from Sullins Electronics Corp. (San Marcos, CA) was used to make electrical contact between the electrode chip and a CHI 760B bipotentiostat (CHI Instruments, Austin, TX). All electrochemical studies were performed at the room temperature using an equimolar solution of 0.1 M $K_3Fe(CN)_6$ and 0.1 M $K_4Fe(CN)_6$ in 0.1 M KCl electrolyte. The concentration studies used additional compositions of 0.05 M, 0.01 M, and 0.001 M of each redox species. Each study using video microscopy for following fluid movement involved a solution prepared by adding a 50.0 μL

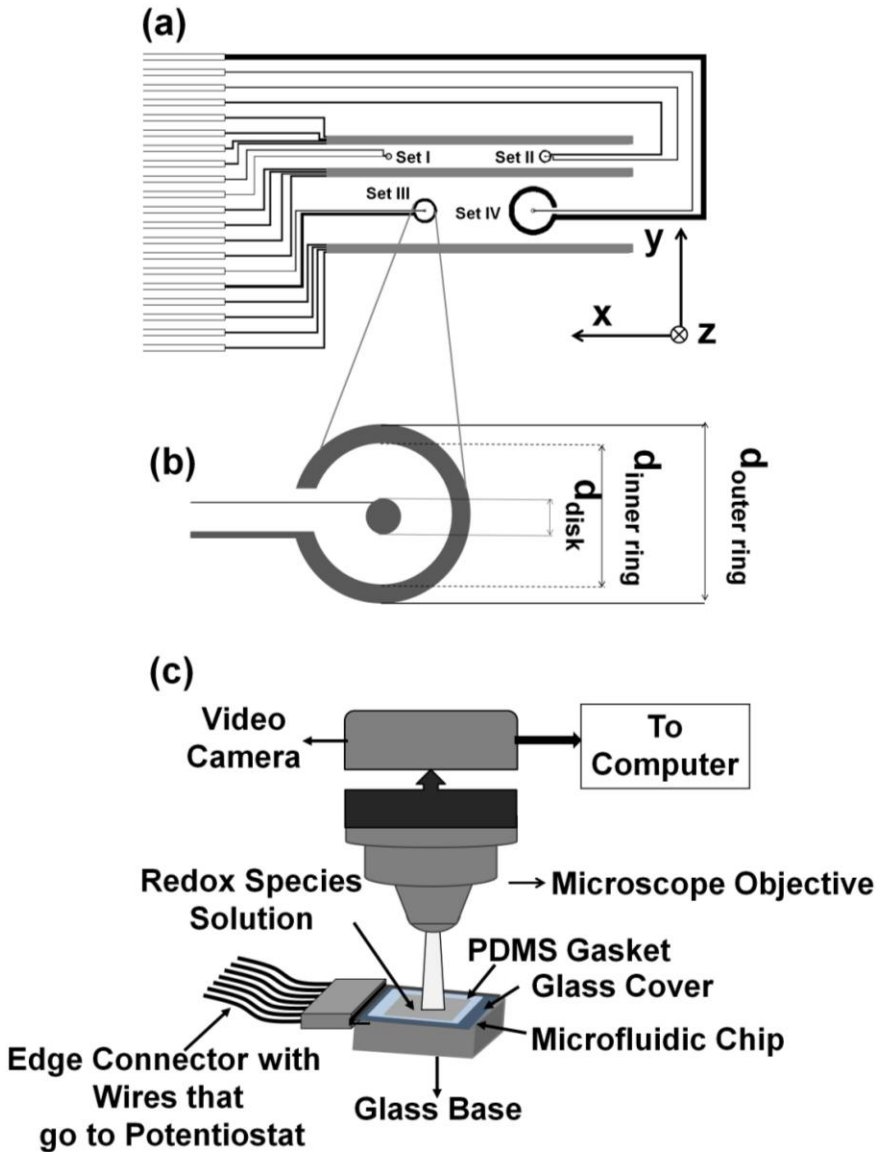

Figure 5.1 (a) Top-down view of the electrode chip design, showing all four sets of differently sized disk and ring electrodes. (The rectangular microband electrodes were not used for this study). **(b)** Expanded view of one such electrode set. **(c)** Experimental setup showing the connection of the electrode chip to a potentiostat/galvanostat, and how fluid movement was monitored by a video camera connected to a microscope.

aliquot of the polystyrene latex microbead solution to 1 mL of a stock solution of $K_3Fe(CN)_6$ and $K_4Fe(CN)_6$ in KCl electrolyte, thus changing the actual solution concentration to 95% of its original value. Electrode characterization was performed using cyclic voltammetry, CV, in a three electrode configuration, where the disk and rings served as working electrodes and an off-chip Pt flag and Ag/AgCl (saturated KCl) electrodes served as counter and reference electrodes, respectively. CV was performed in a 20.0 mL unstirred solution of redox species without polystyrene latex beads. Predicted CV responses were made using DigiSim software (BAS, Lafayette, IN) with details are given in the supporting information section. See Figure 5.S1.

The natural convection experiments used either applied potential (chronoamperometry, CA) or applied current (chronopotentiometry, CP) and were performed in a two electrode configuration, where the disk served as the working electrode and the corresponding ring functioned as the combined counter and reference electrode. Except for the electrode size study, all other experiments used the disk/ring set 3.

In all the natural convection experiments a PDMS gasket having a thickness of 840 μm and a rectangular cutout of 27.5 mm x 12.5 mm was placed directly over the chip, leaving the disk-ring microelectrodes exposed to 350 μL of redox/bead solution, which was dispensed into the opening. The PDMS was topped by a microscope slide, thus making an enclosed electrochemical cell. See Figure 5.S2. The whole assembly was placed under a microscope (LEICA DM 2500M) with an attached SONY HDR-XR 500V camcorder to record the bead movement (Figure 5.1c).

A single experiment involved first dispensing a fresh volume of redox/bead solution, capping it with the microscope slide, and setting the microscope focus to a fixed height above the electrode chip. Bead movement was then recorded for 10 s with the electrodes at open circuit to

establish bead motion due to other sources. Next, a potential or current was then applied for 180 s while continuing to record the bead motion. Between experiments, the electrode chip was rinsed with water and dried with a flow of ultrapure argon.

Videos were processed using particle image velocimetry, PIV, software (Dantec Dynamics) to attain bead velocities. Details have been described previously.[23,24] Bead movement was averaged across a radial segment from 40% to 60% (See Figure 5.S3) of the distance between the disk and ring electrodes over 10 s intervals. The corresponding bead speed, which is assumed to track the fluid speed, was then plotted as a function of time, where "negative" time precedes and "positive" time follows the start of the applied potential or current. "Positive" speed is defined to be in the direction of the disk and "negative" speed is defined to be in the direction of the ring. "Positive" current is defined to be cathodic and "negative" current is defined to be "anodic".

5.4 Results and Discussion

5.4.1 Effects of Electrode Size and Polarity

Figure 5.2 illustrates the overall electrochemical processes that result in the natural convection for two cases: when the disk serves as the anode and the ring as the cathode, and vice versa. PIV images of the velocities of the beads at a fixed height for experiments corresponding to these cases are shown in Figure 5.3 and confirm the model. When the anodic disk converts $[Fe(CN)_6]^{4-}$ (which has four K^+ nearby) to $[Fe(CN)_6]^{3-}$ (which rquires only three K^+ to be nearby), a change in the charged state occurs close to the electrode surface, within the diffusion layer. Ions must migrate to maintain electroneutrality. One could view this effect as the movement of ions in a localized electric field that is produced by the change in charge. The $[Fe(CN)_6]^{3-}$ can be neutralized by the extra K^+ ions moving away from it, other anions moving toward it, the

$[Fe(CN)_6]^{3-}$ moving away from the extra K^+, or a combination of these events. The opposite processes should take place at the cathode where $[Fe(CN)_6]^{3-}$ is converted to $[Fe(CN)_6]^{4-}$. The velocity directions shown in Figure 5.3 support the hypothesis that there is a net migration of K^+. This is because the fluid element over the anode rises, having lost the extra K^+, drawing fluid radially inward to compensate for the void near the chip (Figure 5.3a), and the fluid element over the cathode sinks at the electrode, having gained extra K^+, pushing fluid outward near the chip (Figure 5.3b). The net ionic movement can be predicted by calculating the individual transference numbers of each species, which is defined by[1]

$$t_i = \frac{|z_i| c_i \lambda_i}{\sum_j |z_j| c_{ji} \lambda_j} \qquad \text{(Eq. 5.1)}$$

Here, z is the magnitude of charge, c is the concentration, and λ, the conductivity of ionic species "i" is 101.0 and 110.5 $cm^2\Omega^{-1}$ for $1/3[Fe(CN)_6]^{3-}$ and $1/4[Fe(CN)_6]^{4-}$ ions.

The calculated transference numbers for K^+, Cl^-, $[Fe(CN)_6]^{3-}$ and $[Fe(CN)_6]^{4-}$ are 0.4173, 0.0542, 0.2150, and 0.3136, respectively. Due to its higher transport number, K^+ has a higher probability of moving away from the diffusion layer upon the oxidation of $[Fe(CN)_6]^{4-}$ to $[Fe(CN)_6]^{3-}$ than the movement of anions (Cl^-, $[Fe(CN)_6]^{3-}$ and $[Fe(CN)_6]^{4-}$) inward to compensate for the change in charge. This loss of K^+ counter ions decreases the mass per unit volume (density) near the electrode surface compared to the composition of the solution in the bulk. This density mismatch causes the less dense fluid element near the electrode surface, to move upward due to the force of buoyancy ($\mathbf{F_g}$). See Figure 5.2a. To compensate for this the surrounding solution starts to move toward the electrode surface, thus starting the fluid natural convection as shown inward moving beads in Figure 5.3a. At the reducing counter/ring electrode the opposite reactions take place and a more dense fluid element is produced at the electrode surface which spreads outward along the substrate surface.

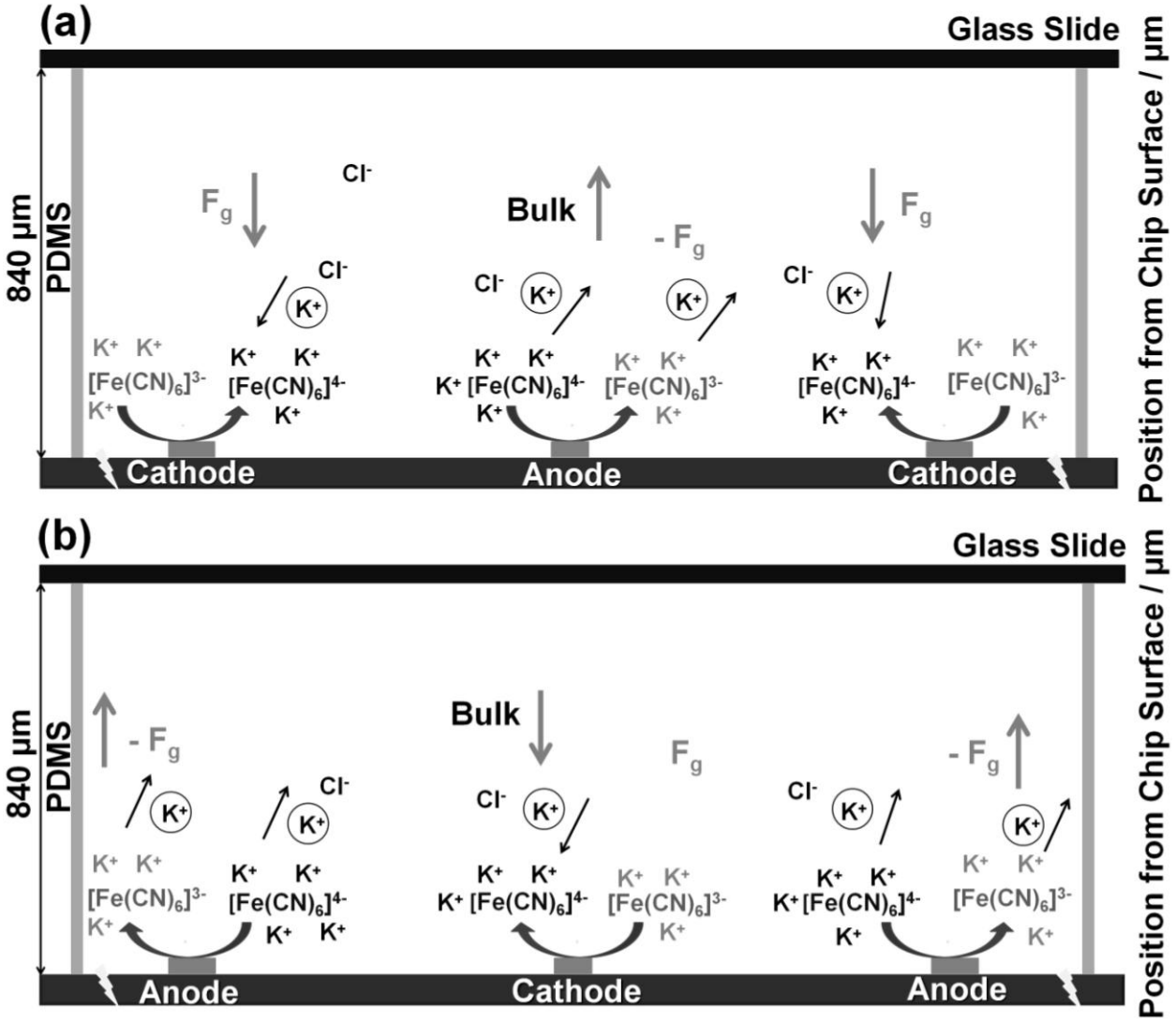

Figure 5.2 Cross-sectional views show the working mechanisms that produce the density gradients. In (a), the disk serves as the anode, and the ring as the cathode. In (b), the opposite assignments are made. Charge transfer at the anode resulting from $[Fe(CN)_6]^{4-}$ to $[Fe(CN)_6]^{3-}$ decreases density because of expulsion of K+; the opposite happens at the cathode. The addition/subtraction of the K+ ions creates a fluid density gradient, thus generating a buoyancy force ($\mathbf{F_g}$) which leads to the natural convection.

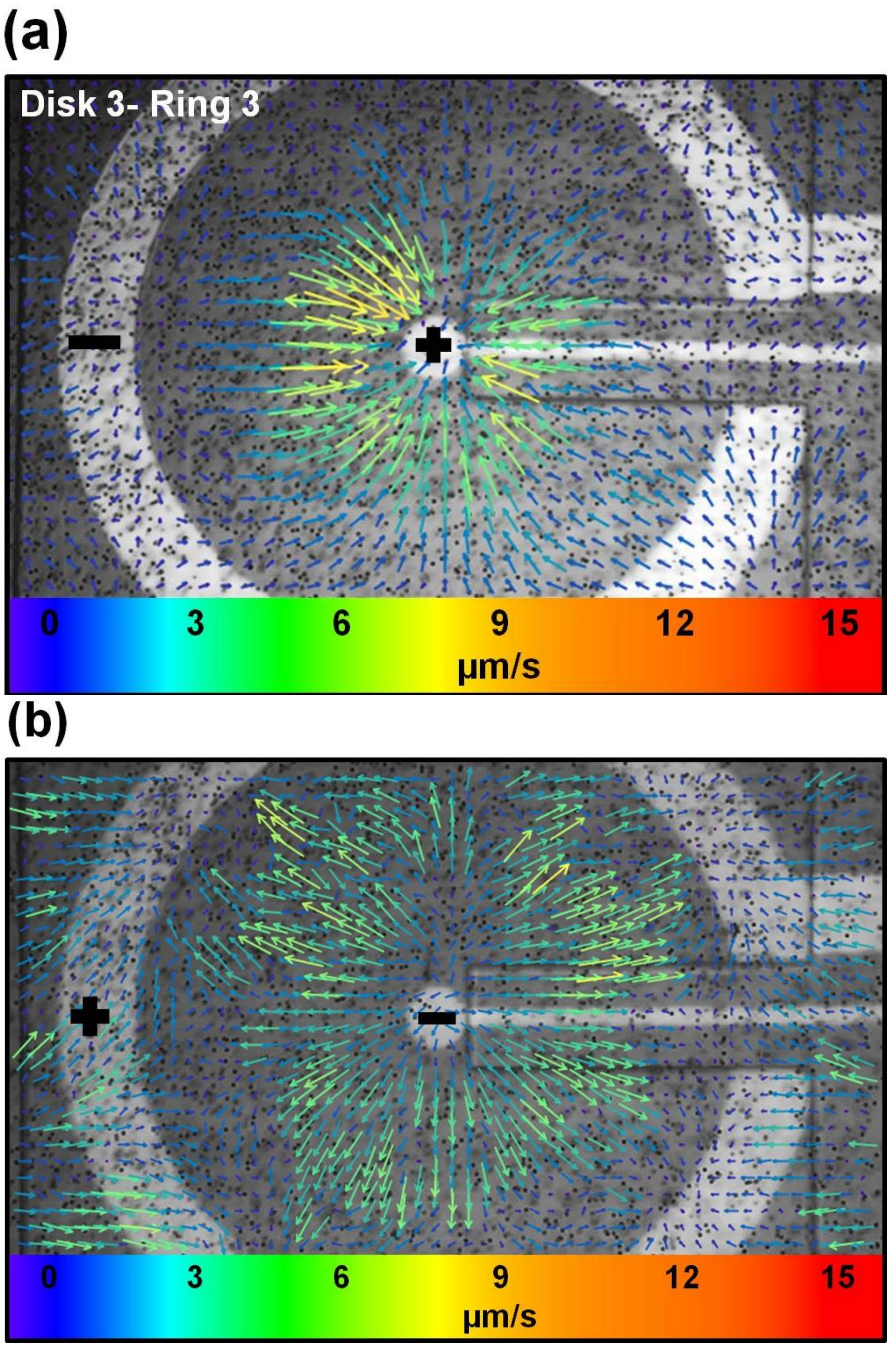

Figure 5.3 Fluid flow switches direction due to a change in the buoyancy force when the polarities of the disk and ring electrodes are reversed from (a) anode and cathode, respectively, to (b) cathode and anode, respectively. PIV processed images show velocity vectors corresponding to bead movement (associated with the fluid motion) from the natural convection at a height of 320 μm above the chip surface and averaged over a time interval of 30-40 s after the application of a potential step.

Natural convection usually refers to the effects from density differences in a fluid caused by temperature variations. While changes in temperature during the experiments are possible and can lead to additional fluctuations in fluid motion, the main cause of the convection in our studies is due to electrochemically-generated density gradients. This is supported by reversing the bias of the disk and ring and observing a change in the fluid direction, as shown in Figure 5.3a and 5.3b. If the main contribution toward natural convection were due to heating of the solution adjacent to the electrodes, where a greater heating would occur at the disk where the current density is higher than at the ring, the same fluid flow direction would have been observed, regardless of the relative bias of the electrodes. The effect of natural convection was also observed in the chronoamperograms obtained at the disk electrode, and appears as a deviation from the usual $t^{-1/2}$ fall off of the faradaic current that follows a potential step, where the current magnitude rises, reaches a maximum (bump), and then falls again, sometimes repeating the fluctuation but with dampened excursions. See Figure 5.4 The ferri-/ferrocyanide redox couple has fast electron transfer kinetics for the time scales of our experiments. Also, the application of a potential step is well beyond the standard electrode potential of the redox couple and lies in the mass-transfer limited region of the voltage window. Therefore, the current response is sensitive to the flux of redox species to the electrode-solution interface. In a static solution, the magnitude of the current response should be diffusion-limited.

The natural convection did not occur immediately upon applying the potential. It took tens of seconds for our conditions before onset. A possible reason for the delayed onset of natural convection could be the effects of opposing forces. With the change in density close to the electrode surface, the influence of surface forces act against it preventing the less dense fluid element to leave from the electrode surface. However, with time, as the density of the fluid

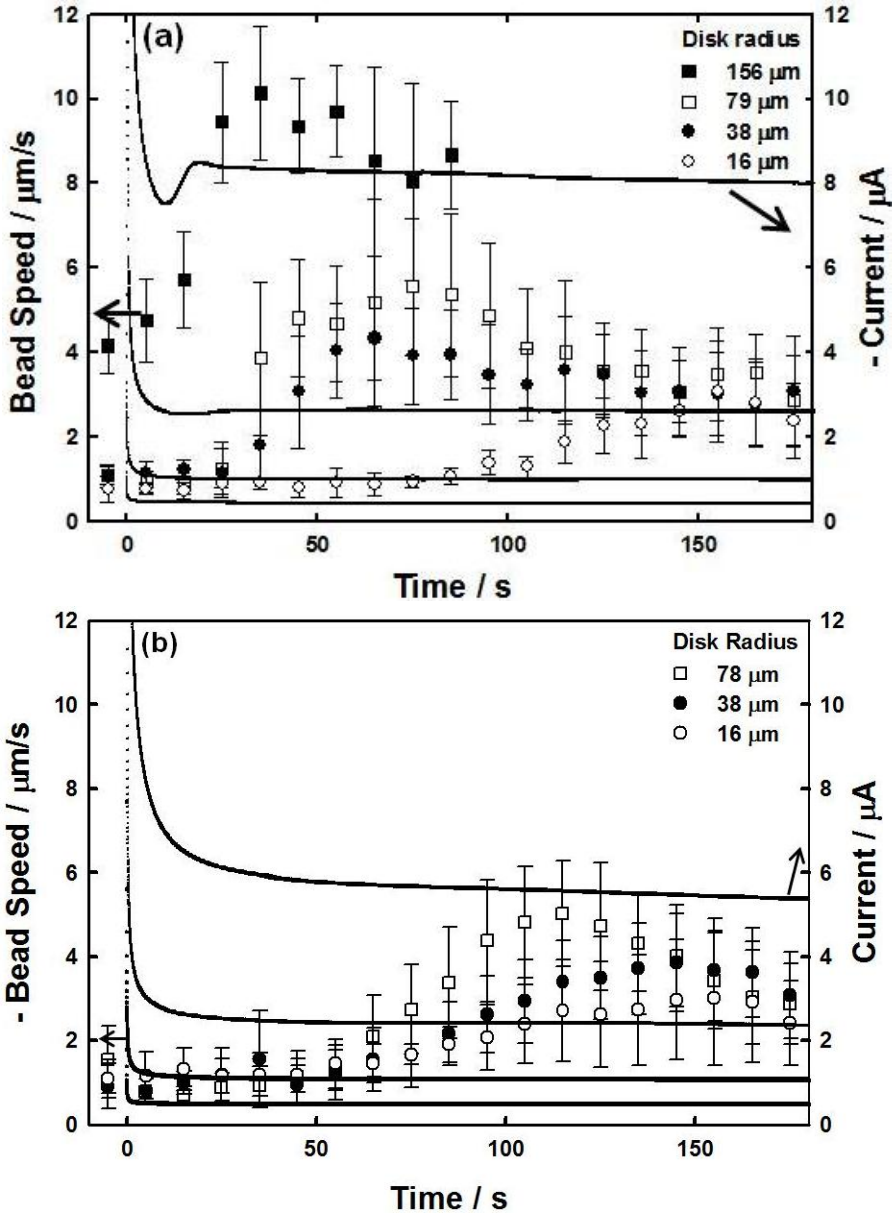

Figure 5.4 Variation of current (measured at the disk) and velocity (measured at a height of 320 μm) as a function of time for differently sized sets of ring-disk microelectrodes, before and after the application of a potential step (at time zero), where the disk and ring served as the (a) anode and cathode, respectively, and the (b) cathode and anode, respectively.

element continues to change with continued electrolysis, buoyancy overcomes the opposing forces, and the fluid element around the electrode begins to rise as is the case at the anode, or spread outward as is the case at the cathode.[4] The localized natural convection which will cause a variation of flux of the redox species toward the electrode surface will lead to variation in the current signal, as well, and therefore to the deviation from the predicted diffusion-limited mass transfer response. After an increase in the current magnitude a corresponding bead movement was also observed due to the natural convection. The impact on the current response of the onset of natural convection is more dramatic for the case when the disk serves as the anode than as the cathode. This can be explained by the greater disruption in the concentration gradient at the electrode that occurs when the volume element rises to the lid, pulling fresh fluid in radially from the surrounding regions toward a focused area at the electrode, than when it spreads outward along the base of the chip, drawing fresh fluid from above and over a larger distributed area than that of the electrode alone.

With an increased electrode area and under applied potential and mass transfer-limited conditions, comparatively more species will undergo charge transfer per unit time, and hence a larger gradient will be produced, and therefore will overcome of the shear forces more quickly. Similar effects were seen in the current signal and bead movement with the increase in electrode size (Figure 5.4a). See Figure 5.S4 for the PIV imaging of electrode size study.

The bumps in the current signal were most obvious with the 80 and 160 μm radius disk electrodes at the ~ 20 and 30th seconds, but it was not visible for the smaller disk electrodes. It was perhaps due to the insufficient gradients that were not able to generate a strong enough impact on the convective mass transfer relative to the radial diffusion. The bead speeds reach maximum values at the experimental time of 25, 35, 65, and 125 s for the 20, 40, 80, and 160 μm

radius disk electrodes, respectively. Alternatively, for experiments with disk as cathode the charge transfer involves conversion of $[Fe(CN)_6]^{3-}$ to $[Fe(CN)_6]^{4-}$. The buoyant forces now switch direction due to the opposite electrode polarity. Movement of sinking fluid element is obstructed by the chip surface underneath, and therefore the sudden natural convection would not occur but rather it will evolve uniformly due to the outward displacement of the surrounding fluid by the sinking fluid elements. See Figure 5.3b and 5.4b.The effects of natural convection for the cathode working has also increased with the electrode size.

In a different but related study by Qian et.al.[25] the effects of natural convection were reported for a toroidal conduit where the redox solution was confined between 1.2 mm high, Pt-coated inner and outer electrode walls of the toroid (inner diameter: 7.2 mm and outer diameter: 10.7 mm). There, the natural convection effects were not observed for < 0.25 M equimolar concentration of $FeCl_2$ and $FeCl_3$. Oscillations in the current response (bumps) at higher concentrations were observed. Theoretical simulations confirmed the enhanced concentration gradients close to the electrode surfaces due to natural convection. Both results are consistent with the observations reported here in our work with a microfluidic setup. However, the redox species in our case were not confined by sidewalls and the natural convection was observed at concentrations as low as 0.1 M $K_3Fe(CN)_6$ and 0.1 M $K_4Fe(CN)_6$ in 0.1 M KCl at 160 μm disk electrode.

5.4.2 Effects of Redox Concentration

Another set of experiments was performed to study the effects of changing redox species concentration. Unlike the studies in the previous section, the electrode area here remains the same (the disk/ring set corresponding to the 80-μm disk radius) so that the compositional

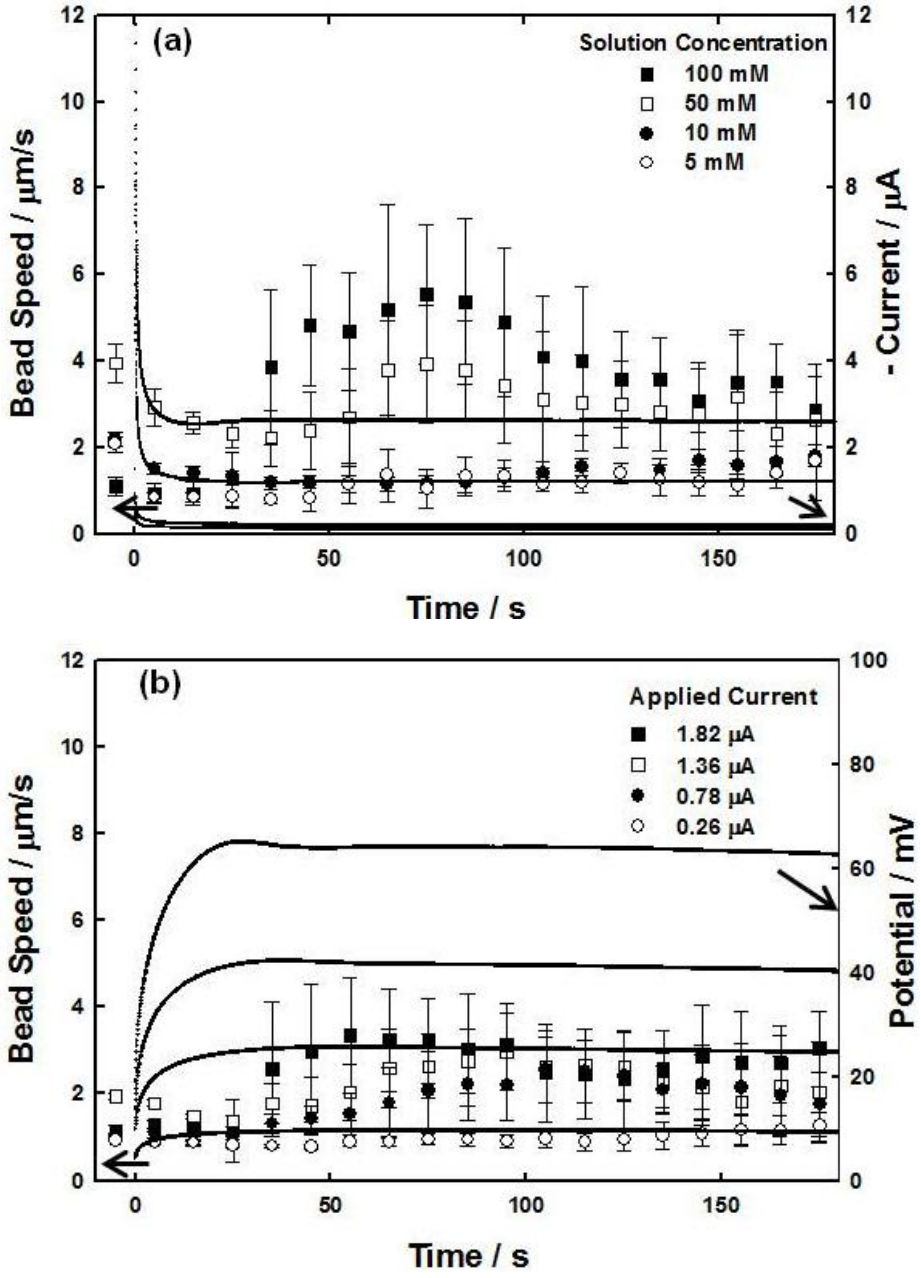

Figure 5.5 Variation of current (measured at the disk) and velocity (measured at a height of 320 µm) as a function of time, where the disk (78-µm radius) and ring (800-µm inner radius) served as the anode and cathode, respectively, for (a) different concentrations of the redox species in an applied potential study, and for (b) different currents in an applied current study for a fixed concentration (100 mM of each form of the redox couple).

changes that occur are confined to the same region. The effects on natural convection of solutions with different equimolar concentrations (5, 10, 50 and 100 mM) were evaluated. As shown in Figure 5.5a, the bead speed increases with increasing redox concentration, and the variations in current magnitude can also be seen clearly with the 100 mM solution. With 5 and 10 mM concentration natural convection effects were absent in the velocity as well as current data. However with 50 and 100 mM solution concentration the sudden increase in current was observed at 55 and 35 s, respectively, followed by an immediate increase in velocity to reach ~ 4 and 5.5 μm/s, respectively. For the same sized electrodes, the availability of electroactive species increase with the concentration, therefore although at low concentrations the electron transfer and the corresponding changes in solution density takes place, but these changes are not sufficient to overcome the opposing forces (except for the 50 and 100 mM), so their effects were minimized.

5.4.3 Effects of the Magnitude of the Applied Current

Experiments were also performed using disk (radius: 80 μm) as anode but with different applied currents (chronopotentiometry). Unlike the studies where concentration increases when there is the possibility for changes in viscosity and tranference numbers, the application of different currents for the same electrochemical setup and solution will allow a better comparison of the effect of the electrolysis rate on the onset and magnitude of natural convection. The values of 10, 30, 50 and 70% of the mass transfer limited current which is 1.82, 1.36, 0.78, and 0.26 μA, respectively, were used in these studies. The bead velocity increases with the increasing applied current due to an increase in the number of charge transfers per unit time, and the natural convection effects were most clearly observable in the data set for 70% applied current when the velocity reach to 3 μm/s after the onset time of 35 s. See Figure 5.5b. Otherwise with 30 and

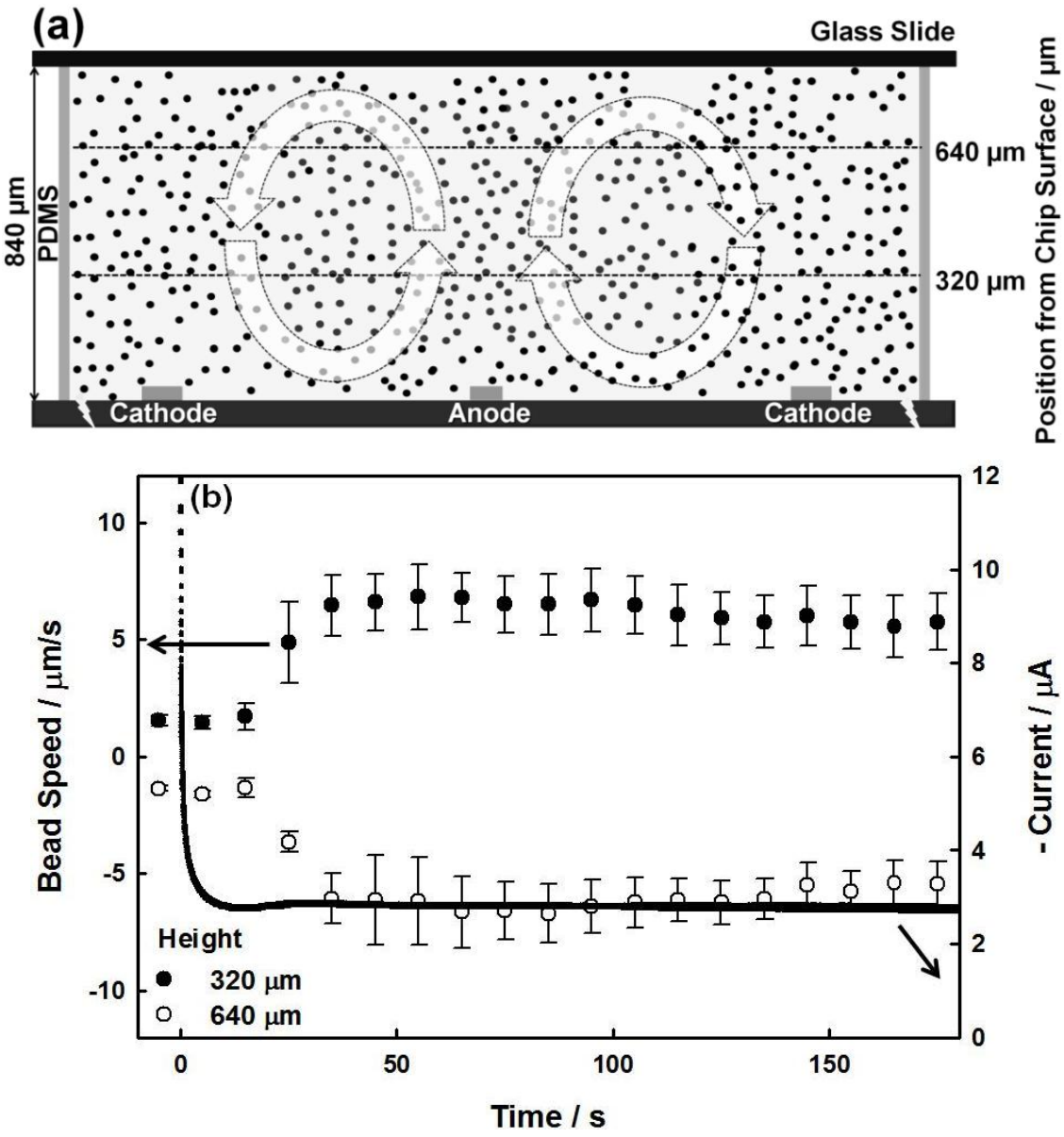

Figure 5.6 Velocity measurements at different heights. Schematic in (a) illustrates the overall fluid circulation that takes place during natural convection and two different heights where the velocity measurements were taken. In (b), speeds measured at two different heights are plotted as a function of time. The overlaying current responses (measured at the disk) that were recorded in those two experiments are indistinguishable from each other. The disk (78-µm radius) and ring (800-µm inner radius) served as the anode and cathode, respectively. A potential step was applied at time zero.

50% applied current a weak onset was seen after 55 and 75 s, respectively when the velocity reach to ~ 2 and 2.5 μm/s, respectively. For the 10% applied current there was no natural convection as evident in the velocity and current data.

5.4.4 Varying the Height where Velocity is Measured

In all of the previous studies, the bead velocity was measured in a horizontal plane at a fixed height about 1/3 of the way between the electrode chip and the lid. Until now, we have made the assumption that the fluid circulates (as illustrated in Figure 5.6a) to compensate for the rise and fall of the fluid elements at the anode and cathode, respectively. To confirm the circulation pattern, we investigated velocities at a horizontal plane that is closer to the lid, as well (approximately 2/3 of the distance from the electrode chip to the lid). Experiments were performed where the bead velocity was measured at the two different heights, but with the same electrode dimensions, solution composition, and applied potential. It was observed as shown in Figure 5.6b that the horizontal flow is in opposite directions at these two heights, as expected. The natural convection onset time for both the experiments is 35 s with a corresponding velocity magnitude ~ 6 μm/s. As observed the moving fluid changes its direction with height that is equivalent to a fluid circulation in the vertical direction, which could have a useful application in microfluidic mixing. The current and velocity data obtained here are a good match to the similar data obtained from the electrode size study.

5.5 Conclusions

Natural convection caused by electrochemically-generated density gradients was studied in a small volume setup that has dimensions comparable to lab-on-a-chip devices and energy conversion and storage devices (e.g. fuel cells, electrochemical double layer capacitors etc.).

Natural convection that was considered insignificant at microelectrodes was found to generate a maximum fluid velocity of ~ 10 μm/s, which is considerably significant for microfluidic systems. The effects of natural convection has been quantified here not only from the changes in current magnitude but also with the associated fluid movement with time and where effects of electrode size, polarity, solution concentration, current magnitude, and the velocity measurement height were investigated. This study will further help in the improvement of small scale analytical systems used in energy, microfluidics and electrodeposition technology by accounting for the mass transfer at microelectrodes, implementing new fluid mixing approaches, and deciphering the uniformity of electrodeposited films, respectively.

5.6 Acknowledgements

We are thankful to the National Science Foundation (Grant number: CHE-0719097 and CBET-1336853) and the Arkansas Biosciences Institute, the major research component of the Arkansas Tobacco Settlement Proceeds Act of 2000, for financial support. We also thank Dr Anupama Aggarwal and Mangjia Hu for helping with the electrode chip fabrication.

5.7 Supporting Information

Supporting information includes cyclic voltammetric characterization of individual disk and ring microelectrodes; schematics for the poly(dimethylsiloxane) gasket placement relative to the electrodes; schematics of the fluid velocity measurement region between the concentric ring and disk microelectrodes; representative images processed by particle image velocimetry showing the effects of natural convection on the bead movement; and calculation of the Reynolds number for this device.

5.8 References

(1) Bard, A. J.; R., F. L. *Electrochemical Methods: Fundamentals and Applications*, Second Edition ed.; Wiley: New York, 1980.

(2) Smith, C. P.; White, H. S. *Analytical Chemistry* **1993**, *65*. 3343-3353.

(3) Gao, X. P.; Lee, J.; White, H. S. *Analytical Chemistry* **1995**, *67*. 1541-1545.

(4) Volgin, V. M.; Davydov, A. D. *Russian Journal of Electrochemistry* **2006**, *42*. 567-608.

(5) Stulik, K.; Amatore, C.; Holub, K.; Marecek, V.; Kutner, W. *Pure and Applied Chemistry* **2000**, *72*. 1483-1492.

(6) Amatore, C.; Pebay, C.; Thouin, L.; Wang, A. F. *Electrochemistry Communications* **2009**, *11*. 1269-1272.

(7) Baltes, N.; Thouin, L.; Amatore, C.; Heinze, J. *Angew Chem Int Ed Engl* **2004**, *43*. 1431-5.

(8) Bograchev, D. A.; Davydov, A. D. *Russian Journal of Electrochemistry* **2008**, *44*. 453-458.

(9) Zelinskii, A. G. *Russian Journal of Electrochemistry* **2010**, *46*. 431-437.

(10) Whitney, G. M.; Tobias, C. W. *Journal of Electroanalytical Chemistry* **1987**, *229*. 429-450.

(11) You, H. J.; Fang, J. X.; Chen, F.; Zhu, C.; Song, X. P.; Ding, B. J. *Chemical Physics Letters* **2008**, *465*. 131-135.

(12) Amatore, C.; Bonhomme, F.; Bruneel, J. L.; Servant, L.; Thouin, L. *Electrochemistry Communications* **2000**, *2*. 235-239.

(13) Amatore, C.; Pebay, C.; Thouin, L.; Wang, A. F.; Warkocz, J. S. *Analytical Chemistry* **2010**, *82*. 6933-6939.

(14) Volgin, V. M.; Davydov, A. D. *Russian Journal of Electrochemistry* **2010**, *46*. 1360-1372.

(15) Amatore, C.; Szunerits, S.; Thouin, L.; Warkocz, J. S. *Journal of Electroanalytical Chemistry* **2001**, *500*. 62-70.

(16) Anderson, E. C.; Weston, M. C.; Fritsch, I. *Anal Chem* **2010**, *82*. 2643-51.

(17) Weston, M. C.; Fritsch, I. *Sensors and Actuators B-Chemical* **2012**, *173*. 935-944.

(18) Leventis, N.; Gao, X. R. *Journal of the American Chemical Society* **2002**, *124*. 1079-1088.

(19) Arumugam, P. U.; Fakunle, E. S.; Anderson, E. C.; Evans, S. R.; King, K. G.; Aguilar, Z. P.; Carter, C. S.; Fritsch, I. *Journal of the Electrochemical Society* **2006**, *153*. E185-E194.

(20) Grant, K. M.; Hemmert, J. W.; White, H. S. *Journal of the American Chemical Society* **2002**, *124*. 462-467.

(21) Ibl, N.; Muller, R. H. *Journal of the Electrochemical Society* **1958**, *105*. 346-353.

(22) Kawai, S.; Fukunaka, Y.; Kida, S. *Journal of the Electrochemical Society* **2008**, *155*. F75-F81.

(23) Sahore, V.; Fritsch, I. *Analytical Chemsitry* **Submitted July 2013**.

(24) Scrape, P. G.; Gerner, M. D.; Weston, M. C.; Fritsch, I. *Journal of the Electrochemical Society* **2013**, *160*. H338-H343.

(25) Qian, S. Z.; Chen, Z. Y.; Wang, J.; Bau, H. H. *International Journal of Heat and Mass Transfer* **2006**, *49*. 3968-3976.

5.S Supporting Information: Electrochemically Generated Density Gradient-Induced Natural Convection in Microfluidic Systems

5.S1 Ring-Disk Microelectrode Characterization

The individual ring and disk microelectrodes were characterized using cyclic voltammetry (CV) before they were used for the natural convection studies. Representative CV responses are provided in Figure 5. S1. They were obtained without microbeads in a static solution of 20 mL 0.1 M $K_3Fe(CN)_6$, 0.1 M $K_4Fe(CN)_6$, and 0.1 M KCl contained in a beaker, where the chip was positioned vertically, using a three-electrode setup with an off-chip Pt flag counter and Ag/AgCl (saturated KCl) reference electrodes. CV's were performed by scanning from 0.6 V to -0.1 V at 0.05 V/s, and with 0.6 V as the initial potential held at a 2 s quiet time prior to the initial forward scan. A correlation with the expected behavior was found using currents calculated from the Digisim (Bioanalytical Systems Inc., West Lafayette, IN) simulations, which confirmed the quality of the electrodes to be used for the further studies. For a single electron transfer homogenous reaction, the maximum theoretical current measured form the zero current line was 1.32, 3.7, 5.2, 20.0, 18.3, 67.4, 252, and 825.9 µA for the disk 1-4 and ring 1-4 microelectrodes, respectively. The double layer capacitance (C_{dl}) used for Digisim calculation was 0.0013, 0.0050, 0.0200, 0.0804, 0.0707, 0.283, 1.1304, and 4.5200 µF, whereas the uncompensated resistance was 4278, 5838, 3467, 1489, 930, 635, 264, and 180 Ω for the disk 1-4 and ring 1-4 microelectrodes, respectively. Other Digisim parameters used were the same as given in the experiments. The experimental maximum currents measured from the zero current baselines have the values of 0.5, 1.8, 5.5, 20.0, 18.3, 65, 240, and 750 µA for the disk 1-4 and ring 1-4 microelectrodes respectively. Except disk 1-2, and ring 3 microelectrodes the experimental and theoretical currents are well match to each other, a possible reason for the observed current differences could be the variations in actual electrode size than the theoretical values. The peak splitting in the CV responses is 255, 140, 120, 120, 145, 170, 170, and 320 mV

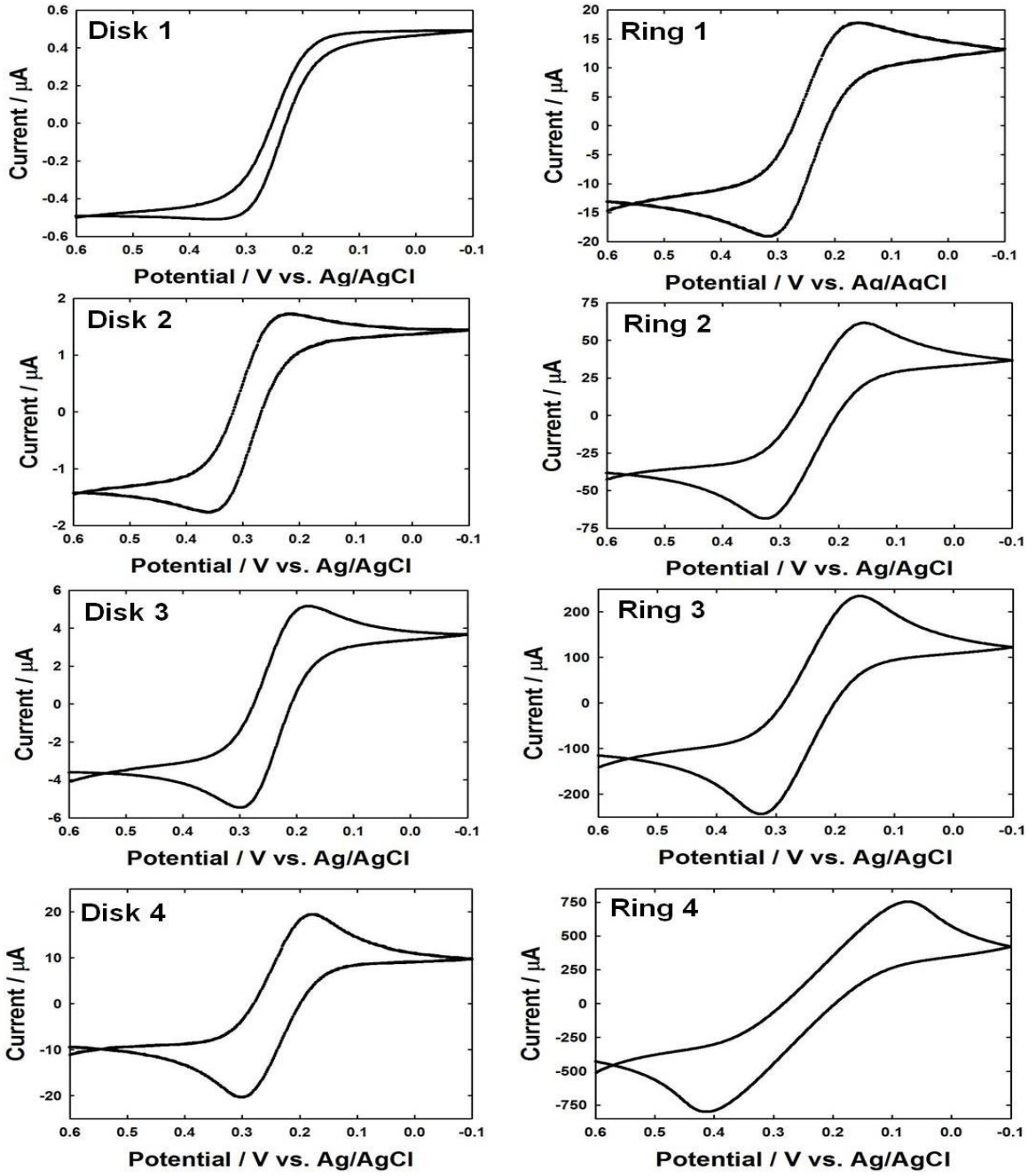

Figure 5.S1 Characterization of the ring-disk microelectrodes using cyclic voltammetry in a static solution of 0.1 M $K_3Fe(CN)_6$, 0.1 M $K_4Fe(CN)_6$, and 0.1 M KCl (without polystyrene microbeads), using a three electrode set up. Here the individual rings and disks were the working electrode, a Pt flag was the counter electrode, and Ag/AgCl (saturated KCl) was the reference electrode.

for the disk1-4 and ring 1-4 electrodes, respectively, and for the corresponding numbers from the Digisim simulations were 152, 240,108, 139, 106, 139, 106, 172, 230, and 420 mV, respectively. This is much larger than the ~60 mV expected for a kinetically reversible redox couple, where n = 1. For the system under investigation because of the high currents due to a high concentration the effects of uncompensated resistance are significant even for the microelectrodes. The measured value for uncompensated resistance with 0.1 M KCl solution using potentiostat's built-in function is sufficient to cause the peak splitting of the observed nature.

5.S2 PDMS Schematics

Figure 5. S2 shows a PDMS location drawn to the scale over the chip. After fabricating the PDMS it was cut carefully from inside to make a gasket shape that can withhold redox species solution from its sides.

5.S3 Schematics for the Velocity Measurement Locations

With the onset of natural convection the fluid in the vicinity of working electrode starts moving, and its movement is recorded by tracking the path of microbeads. The velocity data reported in the main document was taken over an annular disk region that spans from 40-60 % of the distance between a concentric ring-disk microelectrode set, and was defined manually. See Figure 5.S3. Since the phenomenon of natural convection is not symmetric, therefore over the measurement region the average bead velocity has a large standard deviation.

5.S4 Particle Velocimetry Imaging

Figure 5.S4 shows the representative PIV images for the electrode size study where disk(s) were kept at the oxidation potential of +0.4 V. The bead velocity was measured at a height of 320 μm above the chip surface. PIV images were captured at the time for which natural

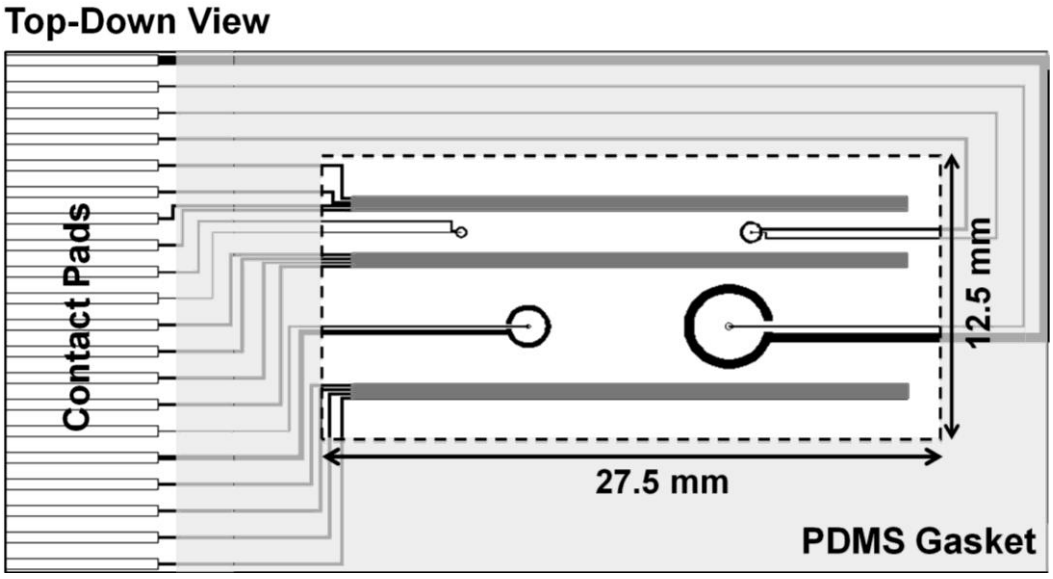

Figure 5.S2 Schematic shows the top down view for the location of PDMS gasket (light gray) relative to the electrode positions. The opening (12.5 mm wide × 27.5 mm long) is outlined by dashed lines, and the height (840.0 μm) is not shown in the figure. There are four different sets of concentric ring-disk microelectrodes represented by the black colors. Black lines connecting the electrodes with the contact pads indicate the BCB-insulated leads. The PDMS sidewalls and a microscope slide placed on top (not shown) here contains the redox species solution dispensed into the open region. All natural convection studies were performed inside the PDMS reservoir by applying a current or voltage at a specific ring-disk electrode set.

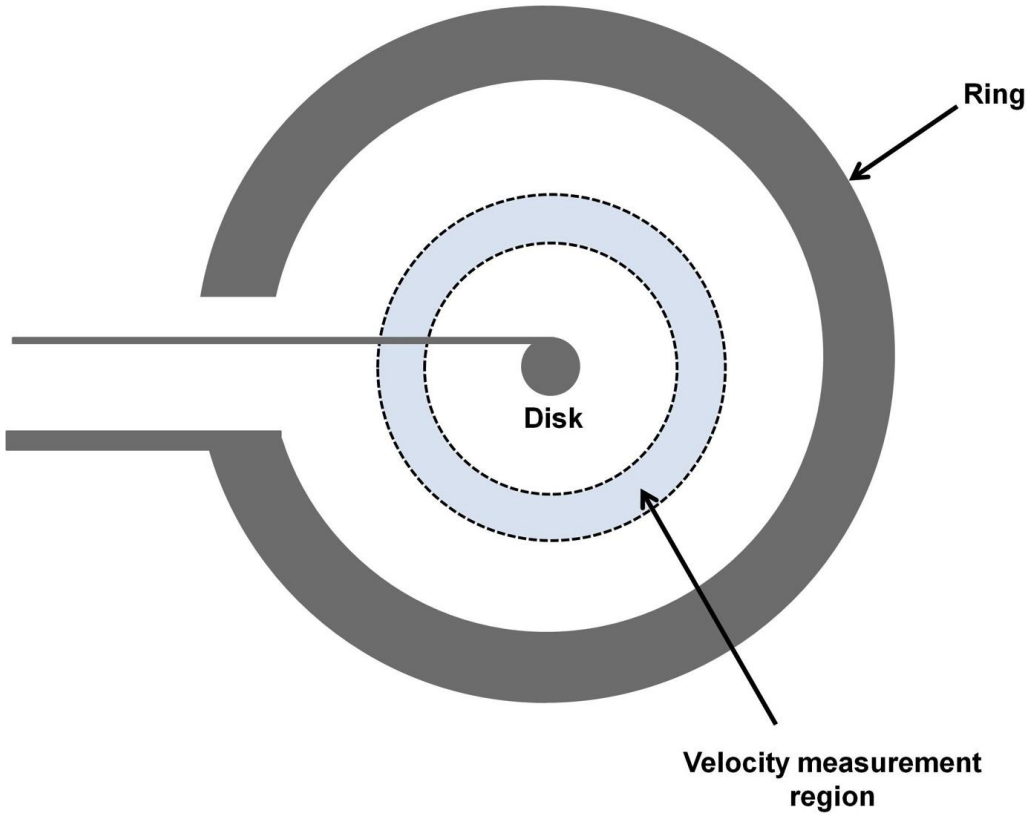

Figure 5.S3 Schematics show a light blue region marked by the dotted black line as the location over which bead velocity was reported in the main document. This region spans across 40-60 % of the distance between disk and the inner ring surface.

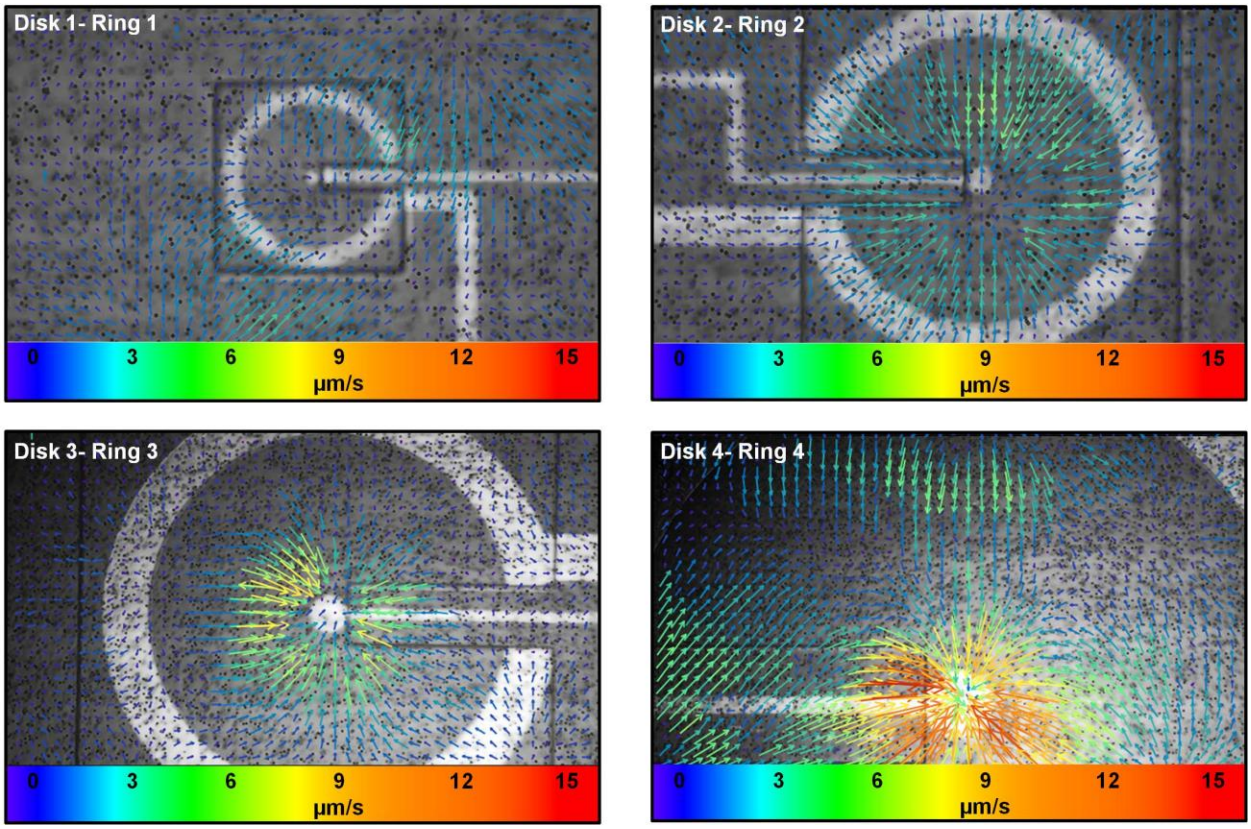

Figure 5.S4 Particle image velocimetry processed figures for the case where the disk(s) were kept at the oxidation potential of +0.4 V with rings as the combined counter/reference electrodes. With the increase in size of the disk electrode the density gradient effects increases, and are evident for the increased velocity of polystyrene latex beads in the solution. As evident from the bead velocity, the effects of density gradient-induced natural convection on horizontal motion are localized at this measurement height over a small region near the disk electrode surface.

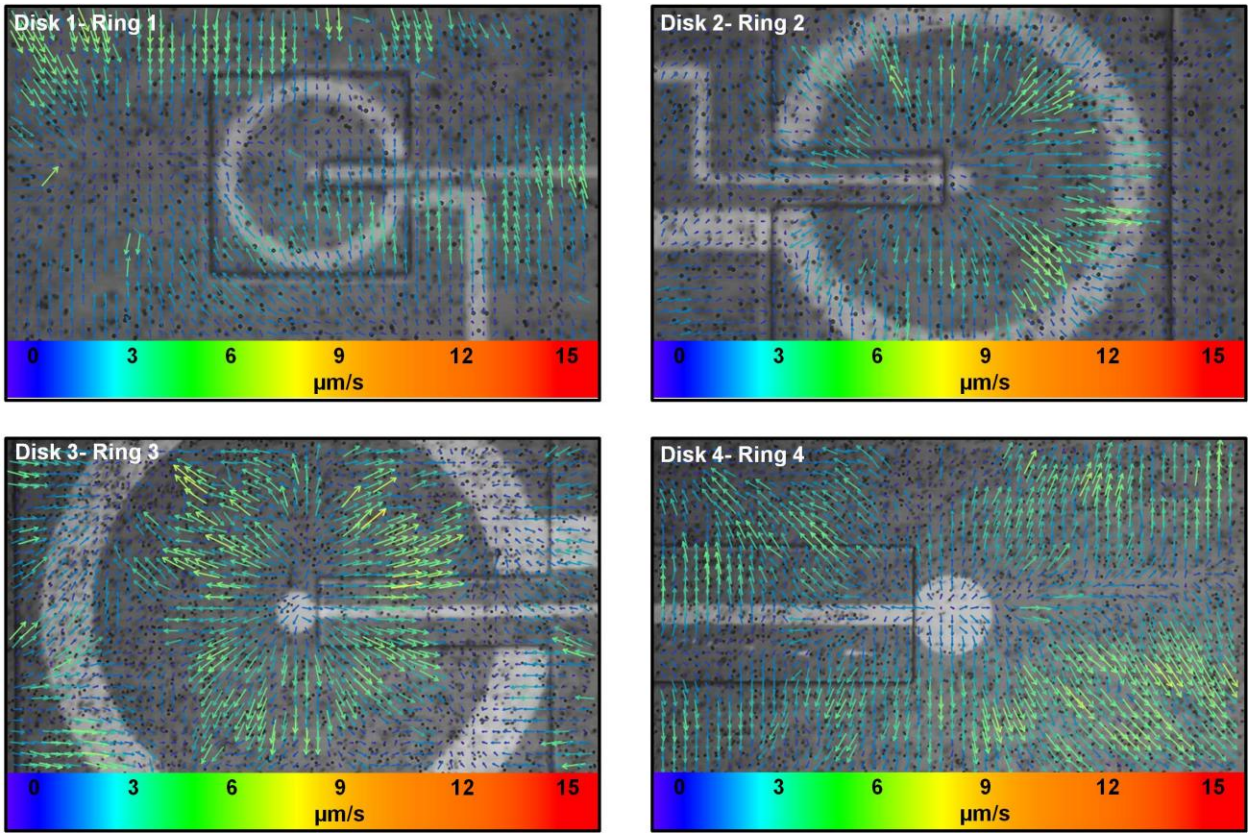

Figure 5.S5 Particle image velocimetry processed figures for the case where the disk(s) were kept at the reduction potential of -0.4 V with rings as the combined counter/reference electrodes. With the increase in size of the disk electrode the density gradient effects increases, and are evident for the increased velocity of polystyrene latex beads in the solution. As evident from the bead velocity, the effects of density gradient-induced natural convection on horizontal motion are localized at this measurement height over a region near the disk electrode surface.

convection onset had occurred for the different working electrodes. Movement of microbeads in the outward direction, and a fast velocity closer to the disk electrode surface has confirmed the density gradients induced natural convection as a localized phenomenon. Due to the limited field of view of the microscope, the effects of natural convection were recorded over half of the region for the disk4-ring4 electrode set. In a PIV image the average velocity was measured over a region depicted in the schematics of Figure 5. S3, and is reported in the Figure 5.3a of the main document. The error bars for each point in those plots correspond to the one standard deviation of the magnitude of all the vectors over this region. The time for which the PIV Figures are reported in Figure 5. S4, are 125, 65, 45, and 35 sec. for the disk-ring electrode set 1, 2, 3, and 4, respectively. For the 20 μm radius disk the natural convection did not occur as the electrochemical conversion was not sufficient to induce its effects. However at the other electrodes due to the floating of the denser fluid volume the effects were more pronounced.

Figure 5.S5 also shows the PIV processed Figures for the experiments where disk(s) were kept at a reduction potential of -0.4 V, and are reported here at 115^{th} sec. for each electrode set configuration. A comparison between Figure 5. S4 and 5. S5 shows a change in the direction of velocity vectors that are consistent with the concept of density gradients as discussed in the main document. Once again at the 20 μm radius disk electrode the natural convection did not occur. However it increases at the large size disks, and was apparent with a change in the polystyrene latex bead velocity. For disk(s) as cathode the velocity of the beads is spread over a large region compared to the disk(s) as anode. The possible explanation for this effect is due to the chip surface at the bottom. As the solution density around the cathodic disk electrode changes, the heavily dense fluid volume is trying to sink.[1] However due to the existence of the chip surface

underneath it has no place to go, therefore due to this cumulative effect the fluid velocity spreads over a comparatively larger region than the experiments with opposite polarity.

5.S5 Reynolds Number

Natural convection by electrochemical density gradients is induced under the laminar flow conditions as calculated by the Reynolds number, Re. Reynolds number is the ratio of inertial to viscous forces and is determined by[2]

$$\boldsymbol{Re} = \frac{\boldsymbol{\rho v l}}{\mu} \qquad \text{(Eq. 5. S1)}$$

Here, $\boldsymbol{\rho}$ is the solution density, $\boldsymbol{v}$ the mean fluid flow velocity, $\boldsymbol{l}$ the hydraulic diameter given by 4 × cross sectional area / wetted perimeter[3,4], and μ is the dynamic viscosity. The value for the Reynolds number under the natural convection conditions is 0.001, 0.004, 0.15, and 0.043 for the electrode set1, 2, 3 and 4, respectively (where $\boldsymbol{\rho}$ = 1045.39 kg/m3, $\boldsymbol{v}$ = 2, 4, 7, and 10 μm/s for the set 1, 2, 3, and 4, respectively, $\boldsymbol{l}$ = 2 × (inner ring radius – disk radius) = 440, 880, 1760, and 3520 μm for set 1, 2, 3, and 4, respectively, μ = 8.4849 × 10-4 kg/m.s). The value of Reynolds number is less than the unity, and hence confirms that the solution in the device is under laminar flow conditions.

5.S6 References

(1) Gao, X. P.; Lee, J.; White, H. S. *Analytical Chemistry* **1995**, *67*. 1541-1545.

(2) Squires, T. M.; Quake, S. R. *Reviews of Modern Physics* **2005**, *77*. 977-1026.

(3) Nguyen, N. T.; Wereley, S. T. *Fundamentals and Applications of Microfluidics*, 2nd ed.; Artech House, Inc. , 2006.

(4) Munson, B. R.; Young, D. F.; Okiishi, T. H. *Fundamentals of Fluid Mechanics*, 5th ed.; John Wiley & Sons, 2006.

6. Conclusions and Future Work

6.1 Conclusions

The results herein this dissertation demonstrate that tunable fluid flow and with flat profiles are achievable by redox-MHD on scales (several centimeters) consistent with lab-on-a-chip devices, and across larger breadths and with larger volumes than shown for electroosmotic flow. Thereby it is possible for redox-MHD to be applied to chip-based chemical analysis with minimal distortion of sample transport, and hence will facilitate multiple, parallel analysis in a single platform. With a different device design it is also possible to use the redox-MHD flat flow profile for separations.

Redox-Magnetohydrodynamics (MHD) microfluidics is also capable of inducing a fluid rotation without requiring flow channels, over an annular region between concentric disk-ring microelectrodes. A fundamental study using polystyrene latex beads show a circular fluid movement, however a swirling flow directed towards the center electrode was observed due to the addition of an external red dye sample. Such a swirling flow can lead to the mixing of fluids if two halves across the disk-ring had two different solutions that can then be combined with a greater speed due to the redox-MHD convection, than by the diffusion alone. Hence the attainment of microfluidic circulation provides an important feature that can be used for the lab-on-a-chip device applications, such as for the immunoassays or DNA hybridization assays. Therefore beyond these fundamental studies the redox-MHD circulation is further expected to enhance the rate of interaction between different analytes, and hence may provide an improvement in analysis time as well as an overall increase in device efficiency.

A proof-of-concept magnetic microbead assay was also integrated with redox-magnetohydrodynamics (MHD) microfluidics to take advantage of the magnet beneath the chip and the uniform flat flow profiles, as a first step toward developing multiple, parallel chemical

analysis on a chip. Choice in placing the magnetic bead assay at any location, due to the presence of a magnet in redox-MHD microfluidics has further offered design flexibility, which could simplify the critical immobilization step in standard immunoassays. Selective placement of enzyme assay complex at different locations has also generated a strong current signal at the locations that were on horizontal path of the detector. At other locations that were off the detector path, current signal is insignificant, thus confirming the potential of redox-MHD flat flow profile to perform multiple, parallel assay detection. Presence of the separate assay immobilization and detection sites at the same platform could further help in the signal enhancement due to less interference at the detector electrode. Bidirectional pumping feature of redox-MHD can further be used with the existing device design to detect different electroactive species at detector electrodes placed on both ends of the microbands. A new device having multiple detector electrodes sitting parallel to each other can also be designed to perform multiplex assay detection during the same experiment.

Natural convection generated by electrochemical processeswas also studied in a microfluidic set up. Natural convection that was considered insignificant at microelectrodes was found to generate a maximum fluid velocity of < 10 μm/s, which is significant from microfluidics perspective. Natural convection effects were quantified from the changes in current and the associated fluid movement, and were dependent on electrode size, electrode polarity, solution concentration, applied current, and velocity measurement height. This will further help in understanding and improvement of small scale analytical systems that are used in microfluidics and electrodeposition technology. A change in fluid flow direction was also observed as a function of height above the chip surface, this feature can further be used to mix two reagents inserted into the on-chip microfluidic system through different inlets. For

electrodeposition technology, deposited thin film thickness can be affected by a sudden onset of natural convection, thus affecting its uniformity. Therefore, the optimization of natural convection results obtained in this dissertation can further be used to control the electrodeposition processes.

Redox-MHD is compatible with the assay detection; however the presence of redox species in the solution interferes with the signal of detection[1] and needs to be avoided. A work is under way at Fritsch laboratory that is trying to contain the redox species on to the electrode by electrodepositing a redox polymer called poly (3,4-ethylenedixoythiophene), PEDOT. In that case the redox species present at the electrodes will generate ionic current density needed to sustain the MHD force, but without being actually present in the solution form. A theoretical approach to solve the ionic current density part of MHD force ($F_B = j \times B$) was also tried, however due to the complexity of the electrochemical systems under consideration a simulation approach using COMSOL will further help to completely understand the nature of the ionic current density distribution, and will be tried in Fritsch laboratory in future.

6.2 Future Work

This dissertation has established the important microfluidic features that can handle large solution volumes at scales greater than the commonly used microfluidic pumping methods such as the electrokinetic pump. Channel-less, bidirectional, programmable flat flow profile and fluid circulation generated by redox-MHD pumping can further be integrated to make a complete lab-on-a-chip device. A proof-of-concept magnetic microbead assay using redox-MHD flat flow profile was the first step in this direction. However by combining flat flow profile and fluid rotation, and interfacing those features with an external switch[2], a self contained assay can also be performed at the same platform. Under that configuration switching on the disk-ring

electrodes will enhance the rate of interaction between two analytes (e.g. two single strand DNA) using redox-MHD rotational flow. Thereafter the generated by product could be carried undistorted to the detector electrode by switching on the flat flow profile, and generate a signal of detection.

To further enhance the scope of redox-MHD microfluidics a method for DNA hybridization assay detection using flat flow profile was designed. The selection of DNA hybridization materials to be used in this work was based upon an earlier study.[3] As a first step, with the existing electrode chip design a single DNA hybridization assay is proposed, however it can be multiplexed with a new device design having multiple parallel detectors lying close to each other. Assay multiplexing will further allow the detection of multiple analytes as well as multiple detections of an analyte on a single chip platform. A stepwise planning for the single DNA hybridization assay detection approach is described below (See Figure 6.1):

Step a. Superparamagnetic bead immobilization:

In the presence of a magnet underneath electrode chip, streptavidin superparamagnetic beads will be immobilized at a position lying on the horizontal path to detector.

Step b. Capture DNA attachment:

The biotinylated capture DNA (5'TGC TGC TAT ATA TAT–biotin-3') solution will be introduced at streptavidin superparamagnetic beads site, to attach with the magnetic beads via biotin-streptavidin bonding.

Step c. Target DNA Attachment:

The next step will introduce a target DNA (5'ATA TAT ATA GCA GCA GCA GCA GCA GCA GCA GAC GAC GAC GAC TCT C3') solution to hybridize with capture DNA.

Step d. Signal DNA Attachment:

The alkaline phosphatase (AP) labeled complementary DNA strand (5'GAG AGT CGT CGT CGT 3'-AP) solution will be poured on the chip to form a final hybridization assay complex.

Step e. Wash Step:

A redox species solution containing $[Ru(NH_3)_6]^{3+/2+}$ in Tris buffer will be inserted and whole assembly was covered with a microscope glass slide (not shown in the Figure) to form a closed electrochemical cell. Redox-MHD pumping will be switched on to wash un-hybridized DNA species away from the detector electrode. See Figure 6.1e.

Step f. Introduction of p-amino phenyl phosphate (PAPP) substrate:

With the pumping electrode off, a PAPP plug solution will be introduced through a glass slide inlet (not shown in Figure) at the AP labeled DNA hybridized complex site, and will be allowed to incubate. At the hybridization site PAPP will react with AP to give an electroactive species of p-amino phenol (PAP_R).

Step g .Electrochemical signal generation and detection:

This step will utilize redox MHD pumping to transport PAP_R species toward the disk electrode. At disk, PAP_R will be oxidized to form PAP_O and will generate an electrochemical current signal.

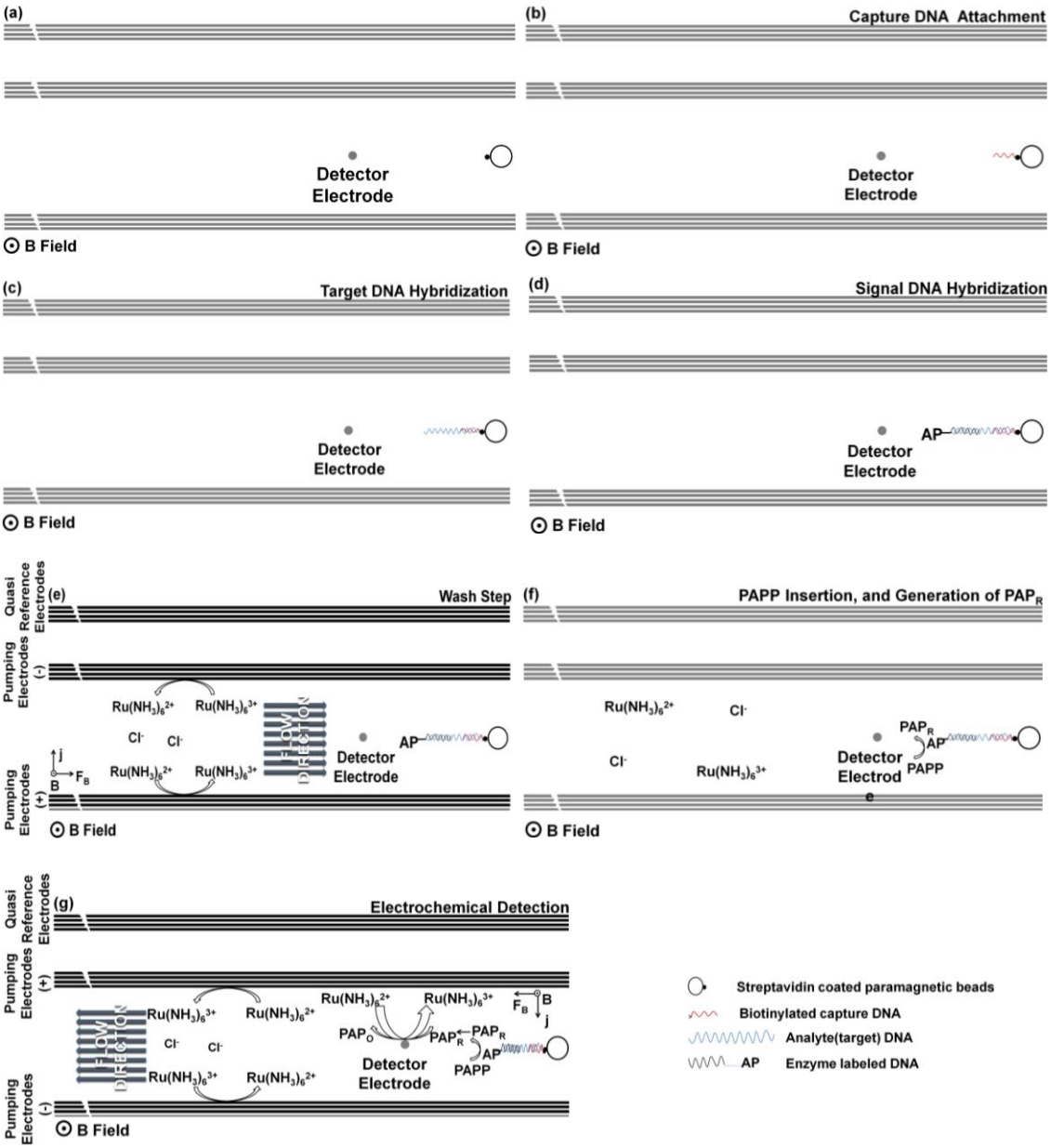

Figure 6.1 Proposed lab-on-a-chip DNA assay to take advantage of the unique features of redox-MHD. **(a)** Superparamagnetic beads will be immobilized in the presence of a magnet underneath the electrode chip, and at a position along on the horizontal path to detector. **(b)** A biotinylated capture DNA will be attached to the streptavidin superparamagnetic beads by exploiting biotin-streptavidin bonding. **(c)** A target DNA will hybridize with the capture DNA. **(d)** Alkaline phosphatase (AP) labeled complementary DNA solution will do the second hybridization to form the enzyme labeled final hybridization assay complex. **(e)** Un-hybridized species will be washed away from the detector site. **(f)** With pumping electrode off, a PAPP plug solution will then be incubated with AP to form the electroactive species of p-amino phenol (PAP_R). **(g)** PAP_R species transported toward the detector using redox-MHD pumping will oxidize to form PAP_O, and generate an electrochemical current signal.

6.3 References

1. M. C. Weston, C. K. Nash and I. Fritsch, Analytical Chemistry, 2010, 82, 7068-7072.

2. M. C. Weston, C. K. Nash, J. J. Homesley and I. Fritsch, Analytical Chemistry, 2012, 84, 9402-9409.

3. M. T. Castañeda, A. Merkoçi, M. Pumera and S. Alegret, Biosens Bioelectron, 2007, 22, 1961-1967.

Appendix A: Electrode Chip fabrication

The electrode chip was made using conventional microfabrication techniques with a procedure that was modified from earlier work performed in our laboratory[1], and an individual chip had multiple features. See Figure A.3, A.4, and A.5, and Table A.1. Briefly, two different photo plot masks were designed using AutoCAD for pattern transfer of the gold microelectrode and BCB (insulator). See Figure A.1, A.2, A.3 and A.4.

A.1 Chemicals and Materials

All chemicals were reagent grade and used as received. Silicon (100) wafers (125 mm diameter, 650 μm thickness, 2 μm thermally grown silicon dioxide) purchased from Silicon Quest International, Santa Clara, CA were used as the substrate material for the chips with patterned electrodes. Chromium and gold layers were deposited on the silicon wafers using chromium coated tungsten rods (Kurt J. Leskar Company, Clairton, PA) and small pieces of gold (Canadian Maple Leaf, 99.99 %) placed in a molybdenum boat (Kurt J. Leskar Company, Pittsburg, PA). Positive photoresist (AZ 4330) was used for the pattern transfer from photo plot masks (Advance Reproductions Corporation, North Andover, MA) to the wafer. Tetramethyl ammonium hydroxide (TMAH) solution was used as a developer in the photolithography process. Gold etchant (Transene, GE8148) and chromium etchant (HTA enterprise, CEP200) were used a received. Negative photoresist, benzocyclobutene, BCB (Cyclotene, 4024-40) was purchased from Dow Chemical Company.

In particular, the following steps were performed to fabricate the chips for redox-MHD studies (See Figure A.6).

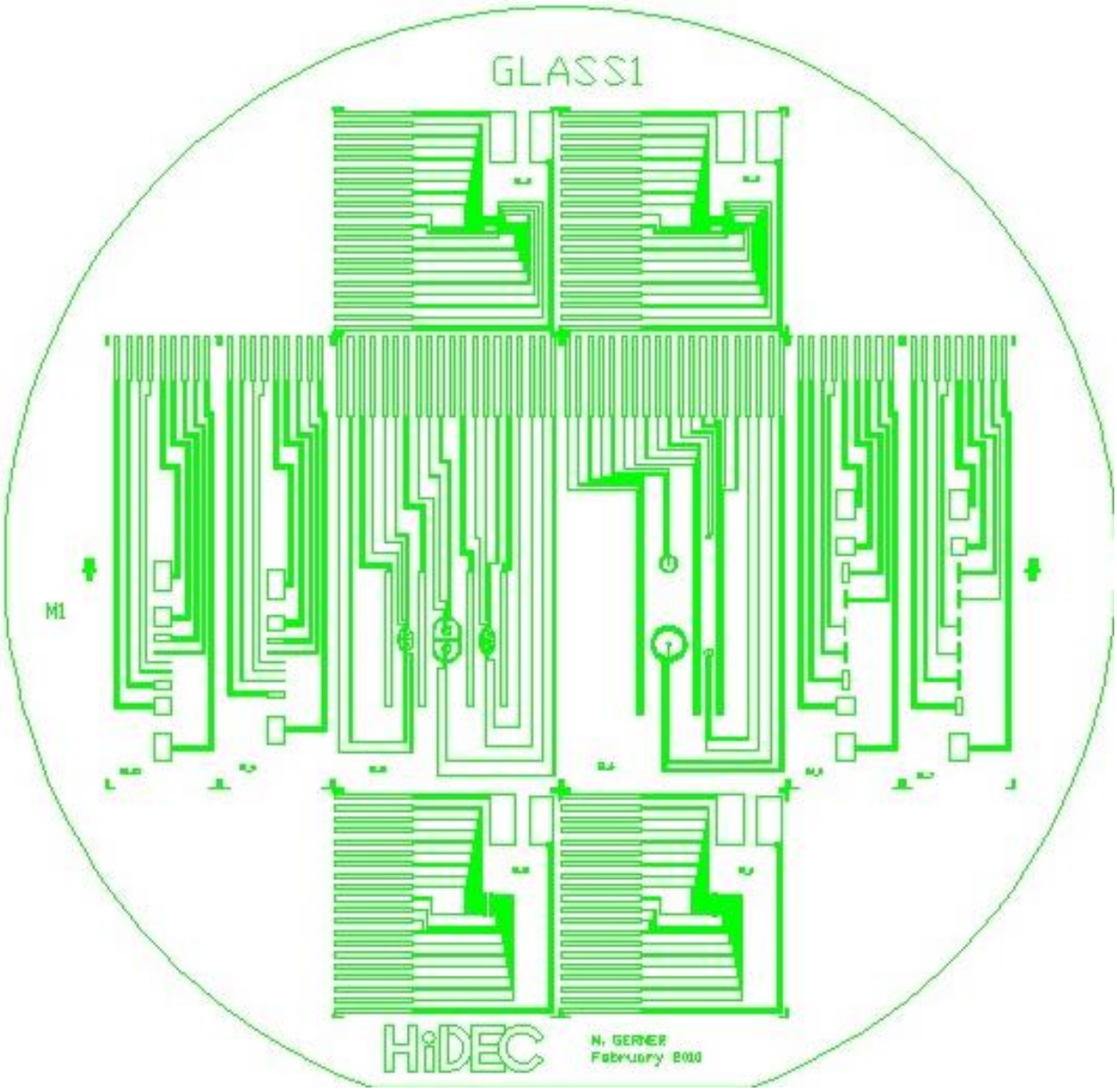

Figure A.1 AutoCAD mask design with gold microelectrode features on a silicon wafer. A single wafer contained 10 different chips; however the chip having disk-ring and rectangular microband electrodes were used for this work.

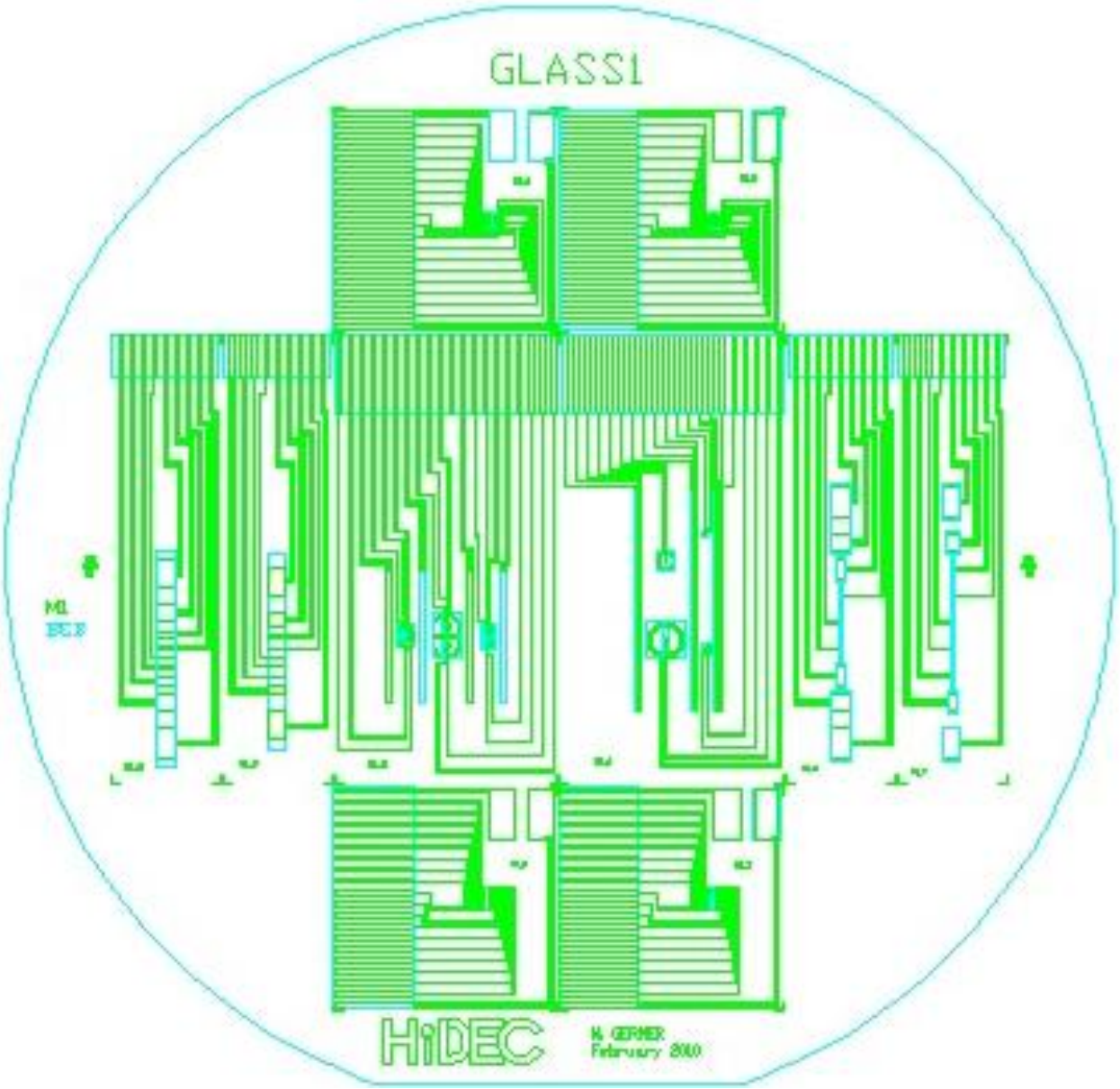

Figure A.2 AutoCAD mask design with benzocyclobutene (BCB) features on a silicon wafer. The mint green colored outline define the edge of the BCB, and outside this outline all the regions were insulated.

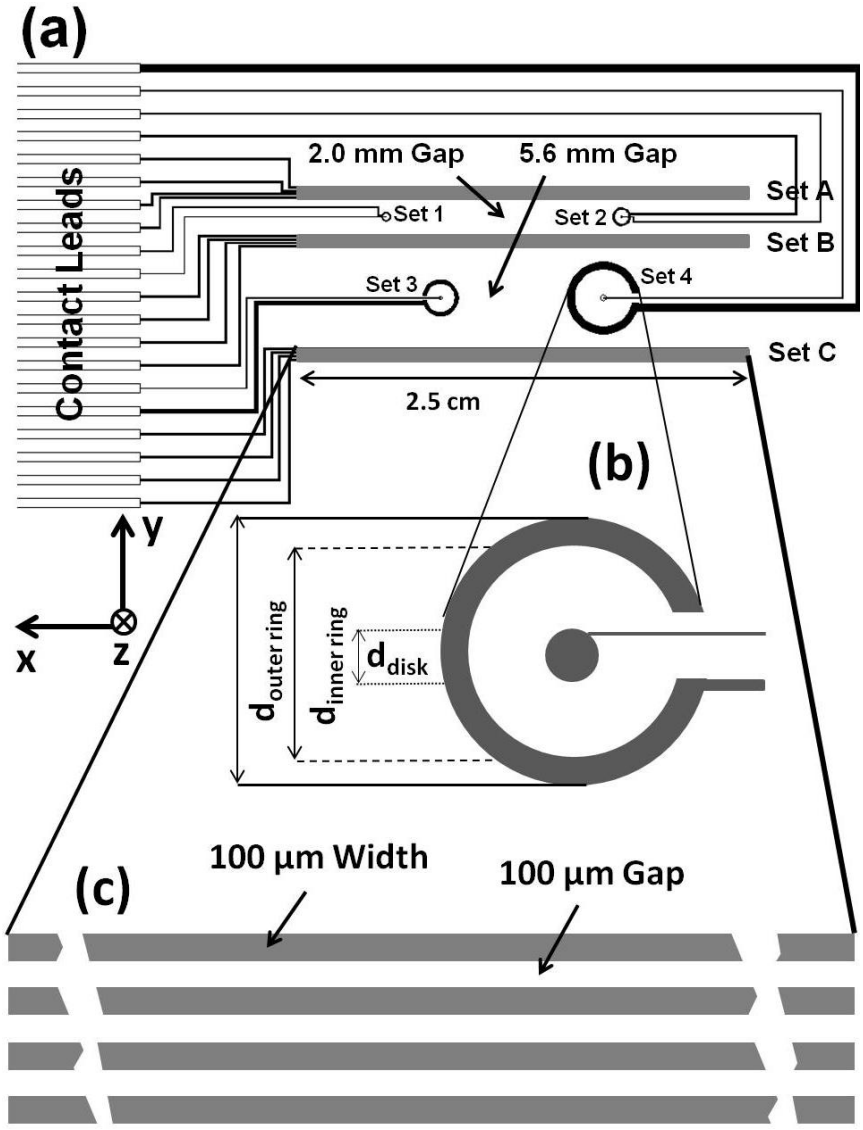

Figure A.3 (a) Top down view of gold mask design for chips used in the studies reported in this dissertation. An individual chip has three microband electrode sets ("set A", "set B", and "set C") with each having four individually-addressable rectangular microelectrodes (1, 2, 3, 4) of equal size (25.0 mm long × 98 ± 0.1 µm wide × ~100 nm thick), and four different sets ("set 1", "set 2", "set 3", and "set 4") of concentric disk-ring microelectrodes. Intraset electrode gap within each microband electrode set is 100 µm, whereas the interset gaps are 2.0 (between sets A and B) and 5.6 mm (between sets B and C). Expanded views of the two kinds of electrode geometries are shown in (b) for the concentric disk-ring electrode set 4, and in (c) for the microband electrode set C, with the corresponding electrode dimensions.

Table A.1 Dimensions of the individual electrodes in the two kinds of geometries available on the electrode chip.

Single Microband Electrode		**Concentric Disk-Ring**				
Length (mm)	25		**Set 1**	**Set 2**	**Set 3**	**Set 4**
		Disk Radius (µm)	20	40	80	160
Width (mm)	0.1	**Inner Ring Radius (µm)**	200	400	800	1600
		Outer Ring Radius (µm)	250	500	1000	2000

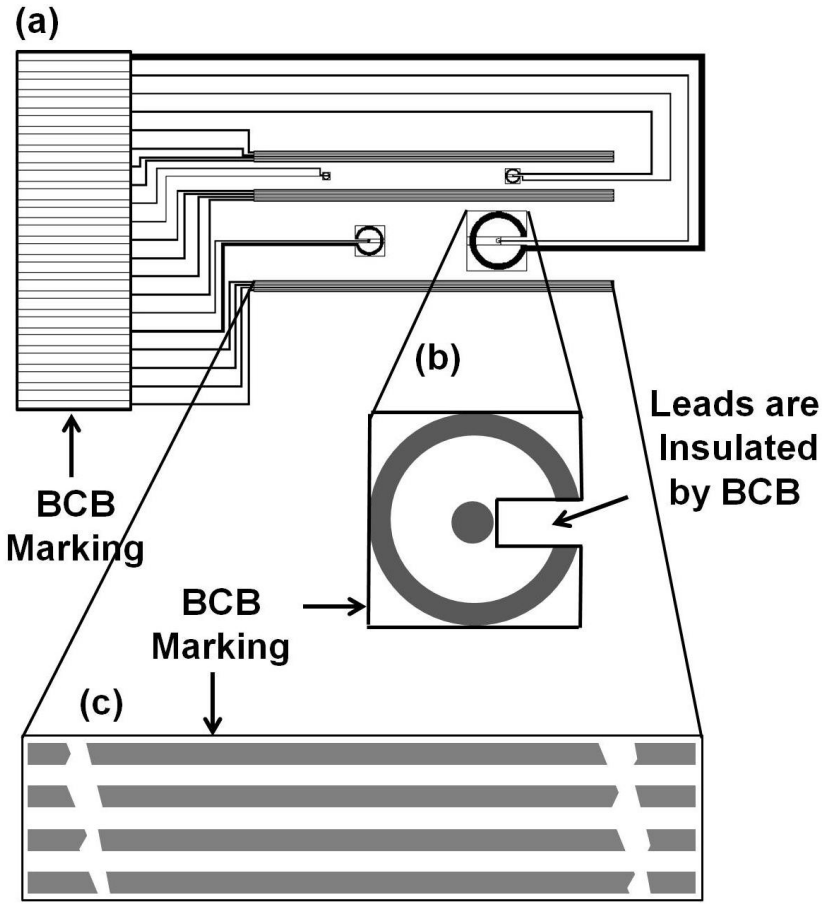

Figure A.4 (a) Top down view of benzocyclobutene (BCB) mask design. BCB layer was patterned to insulate gold leads and other electro inactive regions (except microelectrodes and contact leads) on the chip. Expanded views of the two kinds of electrode geometries are shown in **(b)** for the concentric disk-ring electrode set 4, and in **(c)** for the microband electrode set C. Black outline around the contact pads, microband electrode set C, and disk-ring microelectrode set 3 in the expanded views, define the edge of the BCB, and outside this outline all the regions were insulated.

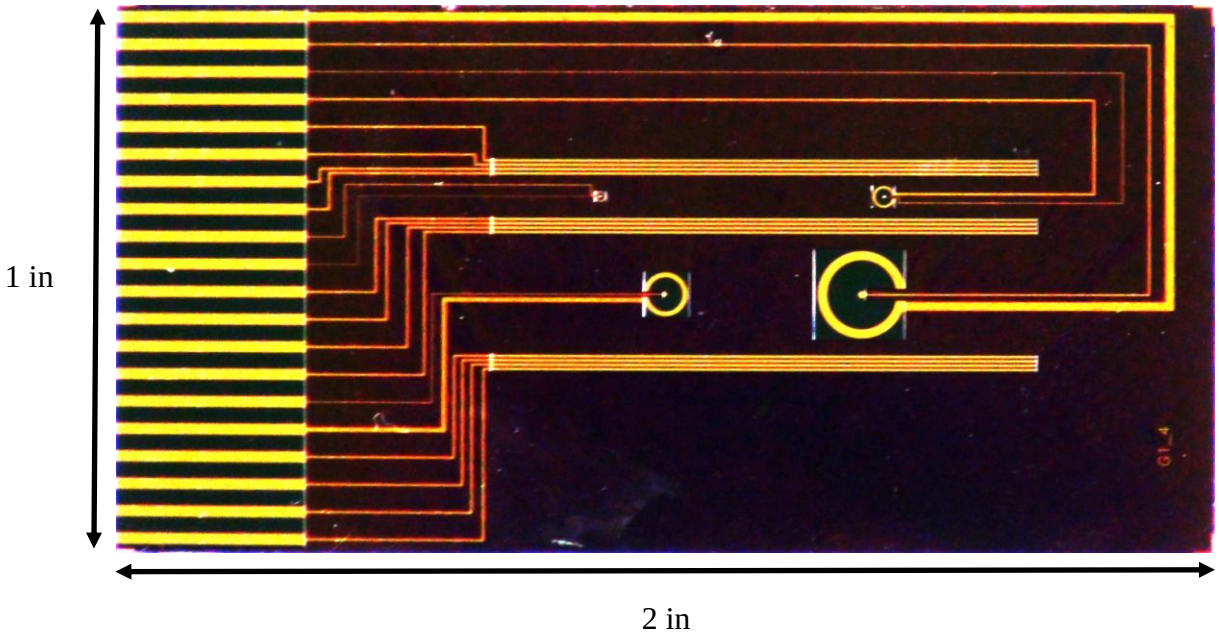

Figure A.5 The picture of an electrode chip containing concentric disk-ring, and rectangular gold microelectrodes.

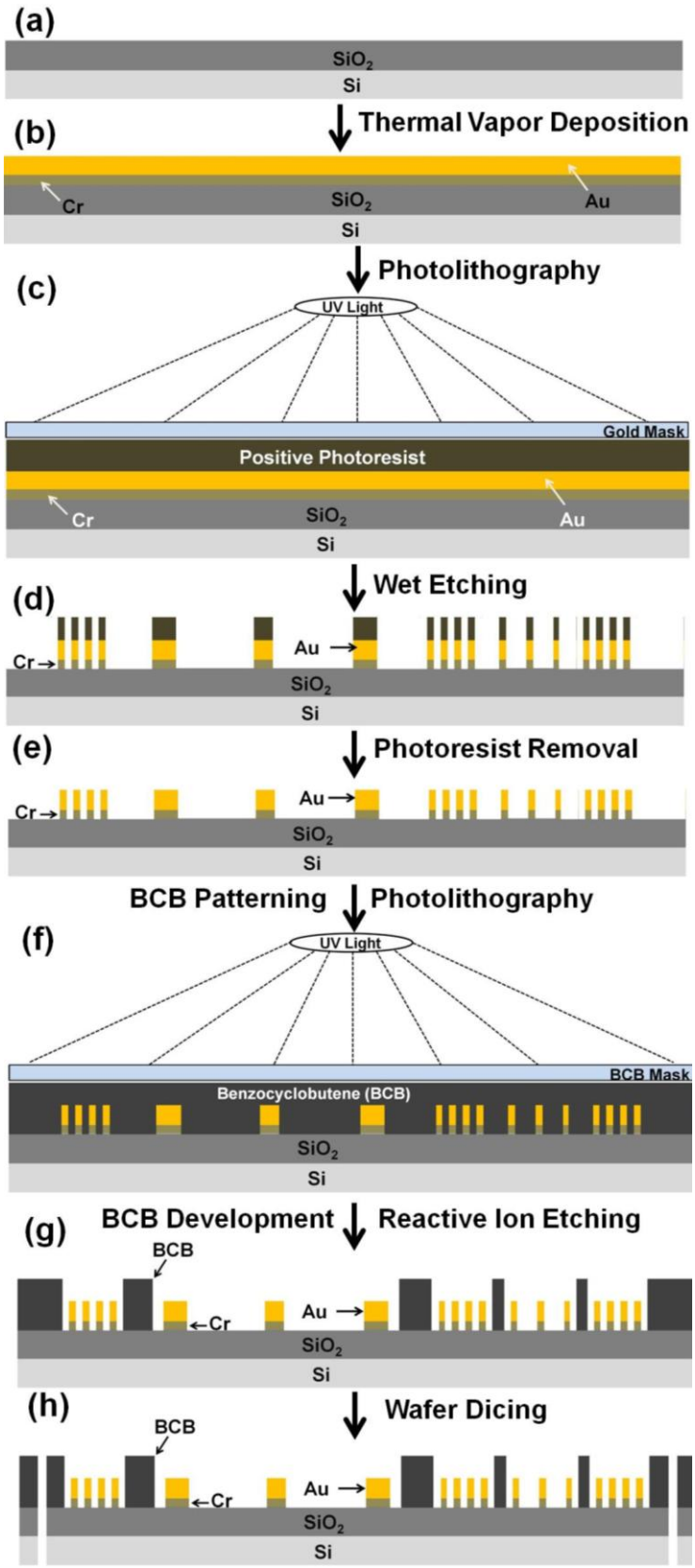

Figure A.6 Caption on the following page.

Figure A.6 Cross sectional view of the device fabrication process (Not drawn to-scale). (a) A silicon wafer with thermally grown silicon dioxide layer (2 µm thickness) was used as the substrate. (b) RCA cleaned wafers were deposited with a 10 nm chromium (brown) as an adhesion layer using thermal vapor deposition, followed by another thermally deposited 100 nm gold layer (yellow), without breaking the vacuum seal between two depositions. (c) Photolithography: Next step involved the design transfer from gold layer mask on to the wafer. Positive photoresist (AZ4313) (dark grey) was spin-coated on the wafer and was exposed to UV light (325 nm) for 19 s followed by the development process in 2.5% tetramethyl ammonium hydroxide (TMAH) solution. (d) Wet Etching: The exposed gold and chromium layers were then selectively removed using chemical wet etching specific to the metals. (e) Wafer was then exposed to UV radiation followed by another tetramethyl ammonium hydroxide (TMAH) bath to remove the remaining photoresist.(f) A polymer layer of benzocyclobutene (BCB) was deposited and patterned using photolithography to insulate any unwanted electroactive features on the wafer. (g) BCB Development and Reactive Ion Etching: Unexposed/undesired BCB was developed and removed in the DS2100 solution, and any leftover at the electroactive regions was descummed using reactive ion etching process. (f) Dicing: Individual electrode chips were cut from the silicon wafer using a dicing saw (Micro Automation 1100).

A.2 Microfabrication Procedure

A. RCA clean: Wafers were cleaned using Radio Corporation of America (RCA) procedure. This involves an organic clean (using 5:1:1 mixture of deionized (DI) H_2O:NH_4OH:H_2O_2 maintained at 75 °C) followed by an oxide stripping process (50:1 mixture of DI H_2O: HF at 27 °C) to remove ~50 nm of the silicon oxide. The wafer was cleaned with a spin rinse dry (SRD) cycle for 2 min.

B. Evaporation: The wafers were deposited with a 10.0 nm chromium adhesive layer using thermal vapor deposition (Edwards Auto 6 Evaporator) followed by another deposition of 100 nm gold layer, without breaking the vacuum seal between the depositions. Deposition was performed at $< 2 \times 10^{-6}$ mTorr pressure and at a rate of < 4 Å/s. Thickness of the deposited layer was based upon the uncalibrated piezoelectric monitor of the thermal evaporator.

C. Photolithography step 1: The design from the mask for the gold layer was transferred to a 1.1 µm positive photoresist (AZ 4330) layer, spin-coated (G3P-8 Spin-Coater) at 6000 rpm on the silicon wafer. After soft baking the photoresist (90 °C for 2 min), the wafer was exposed to ultraviolet (UV) light (325 nm) for 19 s through the gold mask under a Karl SUSS Mictotec MA 150 aligner followed by developing the photoresist in a 2.5% tetramethylammonium hydroxide (TMAH) solution for 2 min at room temperature on Dexton (caustic) wet bench. Wafer was then cleaned for 2 min using SRD.

D. Wet etching: Exposed metal regions on the wafer were selectively removed using gold and chromium etchants on the Dexton (acid) wet bench, and rinsed with DI water inbetween. At the end the wafers were cleaned using SRD cleaning. An experimentally determined, etch time of 45 s and 15 s was used to remove the unwanted gold and chromium layers, respectively. The

entire wafer was further exposed to UV radiation followed by another TMAH bath step to remove the remaining photoresist.

E. Photolithography step 2: BCB, a negative photoresist, was used in this step to insulate leads and define the electrochemically active regions on the wafer. A 5.5 μm BCB layer was spin coated at 3000 rpm followed by a soft baking step at 80 °C for 90 s. The wafer was then exposed to UV light for 19 s under a Karl SUSS Mictotec MA 150 aligner through the BCB layer mask. Unexposed/undesired BCB was removed by washing the wafer with DS2100, a BCB remover, followed by a 4 h hard baking process under an N_2 environment.

F. Reactive ion etching: Residual organic material on electrodes was removed using a "descum" procedure. The BCB-patterned wafer was placed in a reactive ion etching (RIE) chamber (Plasma Therm SLR 720) having a mixture of O_2 at 36 sccm, SF_6 at 4 sccm, at a pressure of 300 mtorr using radio frequency power of 300 W for 1 min.

G. Dicing: The processed wafer was cut into individual chips using a dicing saw (Micro Automation 1100). A single 125-cm diameter wafer contained 10 chips of different designs, but only one type of device was used in this work. The resistance between adjacent band electrodes was beyond the measurement range of FLUKE 77 III multimeter (Fluke Corporation, WA, USA), confirming that the RCA clean did not remove sufficient oxide layer to short the electrodes via the underlying semiconductor substrate.

A.3 References

(1) Anderson, E. C.; Weston, M. C.; Fritsch, I. *Anal Chem* **2010**, *82*. 2643-51.

Appendix B: Description of Research for Popular Publication

Shrinking Laboratory on a Silicon Chip

World needs inexpensive field laboratories to be used in remote set ups, and the way to do this is by shrinking them on to a chip. Dr. Fritsch's research group at the University of Arkansas, Fayetteville has integrated the techniques of microfabrication, electrochemistry, magnetism, and optics to develop a novel microfluidic device platform to create such lab-on-a-chip applications.

Disease diagnostics has been the focus of developing and developed countries for a long time. In the developed world state-of-the-art facilities help in this direction, however, in developing countries the lack of advanced laboratories, skilled work force, and inefficient communication among different regions is a cause of concern. One option is to use small scale portable analytical devices that can be battery powered and are possible to use in remote set-ups without requiring advanced laboratory equipment. This is made a possibility by lab-on-a-chip technology. It can then combine sample preparation, transportation, mixing, separation, and necessary chemical reactions and detection of a single or multiple analytes all at a single chip. One important requirement in lab-on-a-chip technology is the manipulation of fluid at microliter volumes. Redox-magnetohydrodynamics (MHD) microfluidic pumping that can be sustained in the presence of both an electric and magnetic field ($\mathbf{F_B} = \mathbf{j} \times \mathbf{B}$) is a phenomenon that can offer localized control over fluid movement on the chip.

Dr. Fritsch's research group at the University of Arkansas, Fayetteville has been working in this field for a decade now. The lead researcher working on this technology, Vishal Sahore has fabricated a silicon chip with individually addressable microband and concentric disk-ring gold microelectrodes. The device created by Mr. Sahore can transport the microliter fluid volume with

uniform velocity without shape distortion. This technology can also induce a localized fluid circulation at a region between concentric disk-ring microelectrodes without requiring fluid channels.

In a proof-of-concept study Sahore said that “redox-MHD pumping is able to perform multiple and parallel analysis on a single chip”. Researchers at Dr. Fritsch’s laboratory are now trying to detect specific DNA strands by using this device in a lab-on-a-chip setup.

Appendix C: Executive Summary of Newly Created Intellectual Property

The following list of new intellectual property items were created in the course of this research project and should be considered from both a patent and commercialization perspective.

1. A silicon chip having unique size and shape concentric disk-ring and rectangular gold microelectrodes was designed and fabricated for the redox-magnetohydrodynamics (MHD) studies.

2. Channel-less, programmable, and bidirectional flow profiles having uniform velocities at fixed heights across 0.5, 2.0, and 5.6 mm widths, with magnitudes of ≤124.0 μm/s, were sustained along a ~25.0 mm path using redox-magnetohydrodynamics (MHD) microfluidic pumping in a small volume (14.3 mm wide × 27.0 mm long × 620. μm high) on a chip. This microfluidic feature is essential for moving volume elements without shape distortion for lab-on-a-chip assays and separations.

3. Microfluidic rotational flow with velocity ≤ 14 μm/s was achieved over an annular region between concentric disk (radius: 80 μm) - ring (inner radius: 800 μm) microelectrodes. This microfluidic feature is essential for enhancing interactions between multiple reagents (e.g. antigen–antibody interactions).

4. A significant fluid movement (≤ 10 μm/s) over a 0.8 to 3.2 mm region between concentric disk-ring microelectrodes was generated by the natural convection induced by electrochemical reactions under steady state conditions (but without using redox-MHD). This feature is useful to enhance the fluid mixing for on-chip microfluidic systems.

5. A method that uses the inherent presence of an NdFeB permanent magnet beneath the chip and redox-MHD flat flow profile was developed to perform the lab-on-a-chip assays. A

proof-of-concept magnetic microbead assay was integrated with redox-MHD microfluidics, as a first step toward developing multiple and parallel chemical analysis on a chip.

Appendix D: Potential Patent and Commercialization Aspect of Listed Intellectual Property Items

D.1 Patentability of Intellectual Property (Could Each Item be Patented)

The following list of items was considered first from the perspective of whether or not the item could be patented.

1. Silicon chip used in this work is unique in terms of the size and shape of microelectrodes and was specifically designed based upon the fundamentals of redox-magnetohydrodynamics (MHD). This design could be patented.

2. Accomplishment of the channel-less, programmable, and bidirectional flat flow profile microfluidic using redox-MHD pumping with rectangular microelectrode design is unique, and could be patented.

3. Channel-less, bidirectional fluid circulation generated by redox-MHD pumping over a region between concentric disk-ring microelectrodes is also a unique microfluidic feature that could be patented.

4. Natural convection in a microfluidic system was measured over a region between concentric disk-ring microelectrodes using methods of electrochemistry, and optics that involved the particle image velocimetry (PIV) analysis. This study was unique in terms of microfluidic setup, electrode design and PIV based data analysis, and could be patented.

5. The proof-of-concept magnetic microbead assay study could be patented, as it was unique in terms of assay-complex immobilization using inherent magnet used in redox-MHD, a separate assay and detection site, and utilized the flat flow profile toward developing multiple and parallel chemical analysis on a chip.

D.2 Commercialization Prospects (Should each Item be Patented)

The following list of items was then considered from the perspective of whether or not the item should be patented.

1. Electrode chip design should be patented, except for prior public disclosure.

2. Redox-MHD flat flow profile is a fundamental microfluidic feature, and stand alone it should not be patented. However it should be fully developed in a real time multiplex assay detection format and then if it proves advantageous it should be patented, except for prior public disclosure.

3. Redox-MHD fluid circulation is a fundamental microfluidic feature, and stand alone it should not be patented. However it should be integrated in a full lab-on-a-chip setup, and then if it proves advantageous it should be patented, except for prior public disclosure.

4. Natural convection in a microfluidic system was a fundamental microfluidic study, however if it can be integrated in a complete lab-on-a-chip device, then together it should be patented, except for prior public disclosure.

5. Magnetic microbead assay was a proof-of-concept study, that needs to be applied to the diagnostic applications, and then it should be patented, except for prior public disclosure.

D.3 Possible Prior Disclosure of IP

The following items were discussed in a public forum or have published information that could impact the patentability of the listed IP.

1. The silicon chip design was demonstrated at Biosensors 15-18 May, 2012; SciX, September 29 – October 4, 2012; INBRE October 5-6 2012; Pittcon, March 17-21, 2013 conferences; and in an article submitted to the Analytical Chemistry journal.

2. Redox-MHD flat flow profile was discussed at Biosensors 15-18 May, 2012; SciX, September 29 – October 4, 2012; INBRE October 5-6 2012; Pittcon, March 17-21, 2013 conferences; and manuscript was also submitted to the Analytical Chemistry journal.

3. Redox-MHD fluid circulation was discussed at Biosensors 15-18 May, 2012; SciX September 29 – October 4, 2012; INBRE October 5-6 2012; and Pittcon, March 17-21, 2013 conferences

4. The natural convection work was demonstrated at Pittcon, March 17-21, 2013 conference.

5. The proof-of-concept magnetic microbead assay work was discussed at the SciX, September 29 – October 4, 2012 and INBRE October 5-6 2012.

Appendix E: Broader Impact of Research

E.1 Applicability of the research methods to other fields

Electrochemical insights gained from the natural convection studies can also be used in electroplating technology. Redox-MHD microfluidics can also be integrated with biofuel cell technology.

E.2 Impact of Research Results on US and Global Society

This research could eventually be applied to develop analytical devices for point-of-care diagnostic technology. Once established it will help in enhancing the quality of life by providing quick and accurate results for wide spread diseases such as malaria, dengue, diarrhea, etc. In underdeveloped countries this will further help the authorities to contain the spread of diseases and allow for a better and more effective chance to allocate their resources.

E.3 Impact of the Research Results on the Environment

There are no foreseeable harmful effects of this research on the environment. However this research can be used for the environmental monitoring to detect the harmful chemicals. Moreover this research uses microliter fluid volumes that generates less waste and are easy to handle, which further helps in keeping the environment clean.

Appendix F: Microsoft Project for Ph.D. Degree Plan

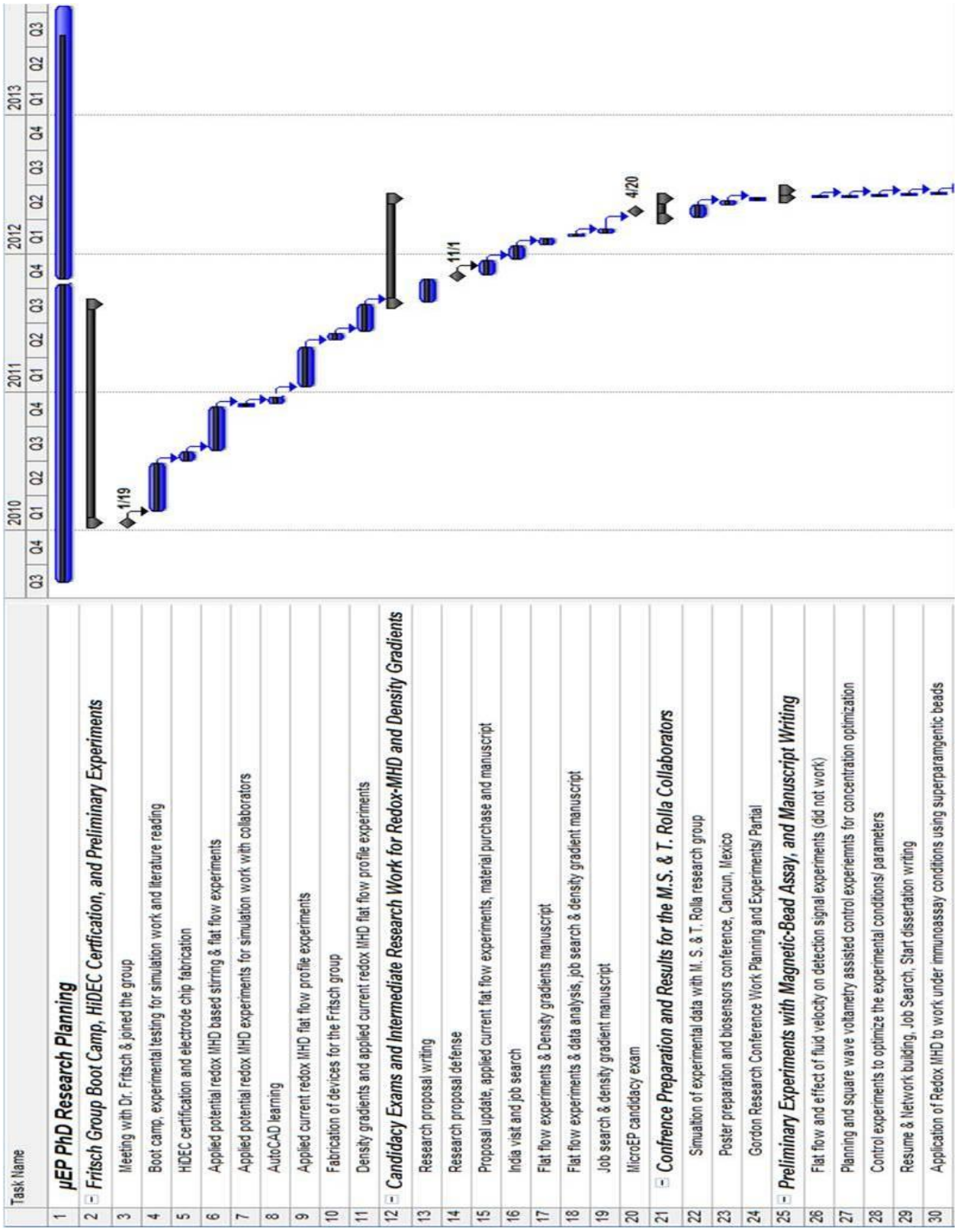

	Task Name
31	Density gradient manuscript work, Echem reading and dissertation
32	Gordon research conference/ under immunoassay condition work
33	***Flat flow and Density Gradients Manuscript Writing, and Bead-Assay Experiments***
34	Density Gradients Manuscript, job search & Dissertation Writing
35	Under immunoassay Condition Experiments
36	Flat flow profile experiments, manuscript & dissertation writing
37	Density gradient manuscript and dissertation writing
38	Under immunoassay condition experiments
39	Density gradient manuscript, under immunoassay experiemnts and dissertation writing
40	Flat flow manuscript/ experiemnt, job search
41	Flat flow profile manuscript
42	Flat flow profile manuscript, dissertation writing, job search and immunoassay experiments
43	Flat flow profile manuscript & dissertation
44	Flat flow profile and fluid stirring manuscript & dissertation
45	Under immonoassay conditions and dissertation writing
46	Flat flow profile manuscript and dissertation writing
47	Flat flow prfofile manuscript
48	***Manuscript Writing, Ionic Current Density Calculation, and Bead-Assay Experiments***
49	Flat flow profile & fluid stirring manuscript writing
50	PDMS and PAPP Synthesis
51	Solution of Laplace equation for Rectangular band and ring/disk geometry
52	Literature survey for comparative advantages of Redox MHD flat flow and stirring
53	Bead Assay Experiments, and Ionic Current Density Calculations
54	Flat flow profile and fluid circulation manuscript writing
55	***Flat Flow and Density Gradients Manuscript Writing, and Bead-Assay Experiments***
56	Flat flow manuscript writing
57	Density gradient manuscript writing, and bead-assay experiemnts
58	PITTCON Conference
59	**Bead-Assay Experiments, DNA Hybridization Assay Preliminary Experiments**
60	Bead-assay final experiments using redox-MHD flat flow profile

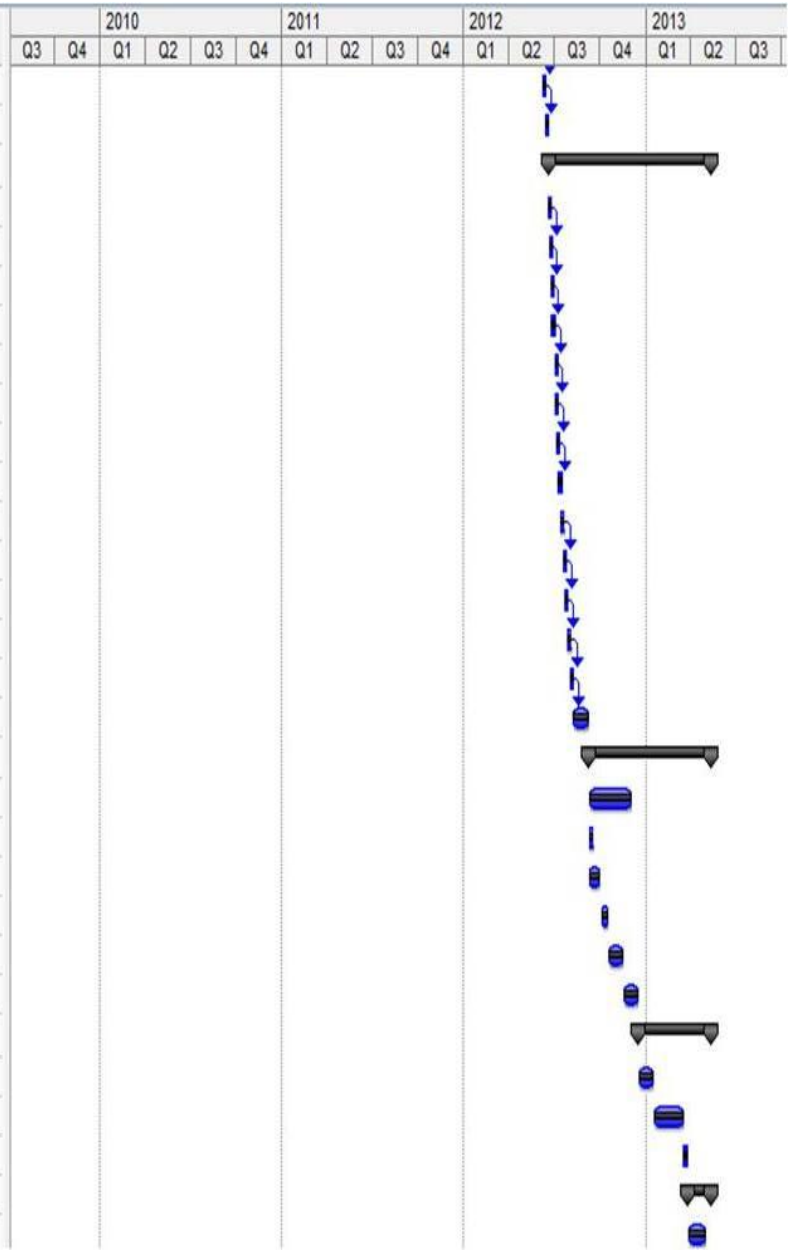

	Task Name
61	Preliminary DNA hybridization experiments
62	***Manuscripts and Dissertation Writing and Submission***
63	Flat flow manuscript writing and submission
64	Redox-MHD fluid circulation manuscript writing
65	Density gradient manuscript writing
66	Bead-assay manuscript writing
67	Dissertation introduction chapter writing
68	Dissertation conclusion chapter writing
69	Dissertation editions
70	MicroEP public presentation and dissertation submission to the committee
71	Dissertation defense
72	Update and complete the dissertation

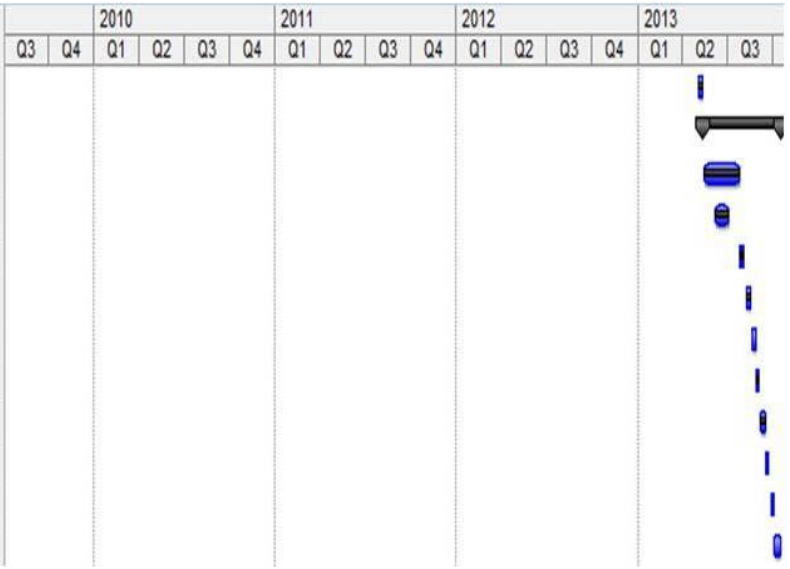

Appendix G: Identification of All Software Used in Research and Dissertation Generation

Computer # 1:
Model Number: Dell Vostro 430A
Serial Number: CQSFLM1
Location: CHBC 103
Owner: Dr. Ingrid Fritsch

- Software # 1
  Name: Microsoft Office 2007 (License Unavailable)
  Purchased by Dr. Ingrid Fritsch
- Software # 2
  Name: AMPERES 3D V.6.4 for magnetic field simulations (Serial No. SK40375-a)
- Software # 3
  Name: Media Converter SA Edition
  Freeware
- Software # 4
  Name: World- in-Motion Physics Toolkit Software
  Freeware
- Software # 5
  Name: CHI 760 B (Serial No. A1409)
  Purchased by Dr. Ingrid Fritsch
- Software # 6
  Name: Sigma Plot (License No. 12BC63C3-35A6C363)
  Purchased by Dr. Ingrid Fritsch
- Software # 7
  Name: Particle Image Velocimetry (Serial No. 6133)
  Purchased by Dr. Ingrid Fritsch
- Software # 8
  Name: End Note Web
  Purchased by University of Arkansas, Fayetteville
- Software# 9
  Name: AutoCAD (Serial No. 33966378914)
  Purchased by Dr. Ingrid Fritsch
- Software# 10
  Name: DigiSim (License Unavailable)
  Purchased by Dr. Ingrid Fritsch

Computer # 2
Model # Optiplex 360
Serial # DQTJ5J1

- Software # 1
  Name: Microsoft Office 2007 (License Unavailable)
  Purchased by Dr. Ingrid Fritsch
- Software # 2
  Name: Particle Image Velocimetry (Serial No. 6133)

Purchased by Dr. Ingrid Fritsch

- Software # 3
  Name: End Note Web
  Purchased by University of Arkansas, Fayetteville
- Software # 4
  Name: Sigma Plot (License No. 12BC63C3-35A6C363)
  Purchased by Dr. Ingrid Fritsch

Appendix H: All Publications Published, Submitted, and Planned

Submitted:

(1) Flat Flow Profiles Achieved with Microfluidics Generated by Redox-Magnetohydrodynamics (MHD). V. Sahore, I. Fritsch, *Analytical Chemistry*, *Submitted in* July 2013

In Preparation:

(2) Microfluidic Rotational Flow Generated by Redox-Magnetohydrodynamics (MHD). V. Sahore, I. Fritsch, Microfluidics and Nanofluidics

(3) Electrochemically Generated Density Gradient-Induced Natural Convection in Microfluidic Systems. V. Sahore, A. Kreidermacher, I. Fritsch, Electrochimica Acta

(4) Redox-Magnetohydrodynamics (MHD) Flat Flow Profile Guided Enzyme Assay Detection: Toward Multiple, Parallel Analysis. V. Sahore, I. Fritsch, Analytical Chemistry

(5) Observing Electrochemically Generated Density Gradient Based Fluid Flow with band electrodes in a Microfluidic Setting. A. J. Kreidermacher, V. Sahore, and I. Fritsch, Electrochimica Acta.